ЕІЕлектротехніка і лектромеханіка

Electrical Engineering & Electromechanics

Електротехніка. Визначні події. Славетні імена
Електротехнічні комплекси та системи.
   Силова електроніка
Теоретична електротехніка та електрофізика
Техніка сильних електричних та магнітних полів.
   Кабельна техніка
Електричні станції, мережі і системи

ISSUE 4/2018
TABLE OF CONTENTS

M.I. Baranov

AN ANTHOLOGY OF THE DISTINGUISHED ACHIEVEMENTS IN SCIENCE AND TECHNIQUE. PART 45: TRADITIONAL POWER ENGINEERING. HYDRAULIC POWER PLANTS: STATE AND PROSPECTS OF THEIR DEVELOPMENT

***Purpose.** Preparation of brief scientific and technical review about the state, achievements, problems and prospects of development of world hydraulic power engineering. **Methodology.** Known scientific methods of collection, analysis and analytical treatment of the opened scientific and technical information, present in scientific monographs, journals and internet sources, high meaningfulness in area of hydraulic power engineering. **Results.** A brief analytical scientific and technical review is resulted about the present state, achievements, problem tasks and prospects of development of hydraulic power engineering in the industrially developed countries of the world. Considerable progress is marked in development and creation of technical base of modern hydraulic power engineering including powerful hydraulic turbines and hydraulic electric generators. Existent classification of the hydraulic power plants (HPPs) is resulted. Basic types and constructions of powerful hydraulic turbines, in-use on modern HPPs are presented. Basic kinds and technical descriptions of powerful hydraulic electric generators used at modern HPPs are indicated. Information is resulted about the largest in the world ordinary HPPs and hydraulic heat-sink HPPs. Hydraulic power engineering of Ukraine is considered and descriptions of basic domestic HPPs are described. Advantages and failings of HPPs are marked in comparison with the thermal and nuclear power plants. Information is presented about absolute volumes of electric power produced by HPPs in a number of the industrial developed countries of the world. Quantitative indexes are resulted for today in the world of reserve of hydraulic power resources on the continents of our planet. A conclusion is done that this reserve of hydraulic power resources is mainly concentrated in the countries of Asia. It is indicated that hydraulic power engineering of the world produces presently up to 21 % of electric energy in annual world in the electrical energy balance. Some problem tasks of world hydraulic power engineering are indicated. Certain prospects are outlined in development of hydraulic power in the world and in Ukraine. **Originality.** Systematization is executed as short structured of scientific and technical review of the scientific and technical materials touching functioning of such important sector of world economy as hydraulic power engineering known from the open sources in informative space. Material is expounded from positions of scientist-electrophysics in an accessible for a wide reader new informatively-rich content form. **Practical value.** Popularization and deepening for students, engineers and technical specialists and researchers of front-rank scientific and technical knowledge in area of modern hydraulic power engineering extending their scientific range of interests and promoting further development of scientific and technical progress in society.* References 21, figures 13.
Key words: **hydropower engineering, hydraulic power plants, hydraulic turbines, hydraulic electric generators, characteristics of hydraulic power plants, problems and prospects of development of world hydropower engineering.**

Приведен краткий научно-технический обзор о современном состоянии и перспективах развития мировой гидроэнергетики. Рассмотрены основные схемы построения и виды гидравлических электрических станций (ГЭС). Указаны преимущества и недостатки ГЭС перед другими видами электрических станций, генерирующих электричество. Приведены основные технические характеристики крупнейших ГЭС мира и Украины. Отмечена важная роль гидроэнергетики в объемах годовой выработки электроэнергии в ряде стран мира. Обозначены проблемные задачи в области гидроэнергетики мира и Украины. Библ. 21, рис. 13.
Ключевые слова: **гидроэнергетика, гидроэлектростанции, гидротурбины, электрогидрогенераторы, характеристики гидроэлектростанций, проблемы и перспективы развития мировой гидроэнергетики.**

Introduction. By and large, nature on the planet Earth has created a wonderful substance − water, a molecule of which, as we all know, consists of two atoms of hydrogen and one oxygen atom. This substance in the usual molecular form (light water, consisting of the atoms of the isotope of hydrogen $_1^1H$ − protium and the isotope of oxygen $_8^{16}O$ [1]) is the basis of the life activity of everything on our planet (possibly not only on the planet Earth!). It is on it that all the basic physicochemical processes of metabolism in the plant and animal world are based. As civilizations evolved, people learned how to use not only the intramolecular energy of water in their life activity, but also its potential energy to bring the wooden aggregates with circular millstones to circular rotation in order to obtain from the grain of agricultural crops flour and then bread baking, and later round metal rotor of an electric generator which generates electricity in the windings of its stator. To increase the potential energy reserves in the water on the way of its movement and its pressure, it was necessary to build reinforced concrete dams (Fig. 1) and correspondingly huge reservoirs with a large difference (in tens and hundreds of meters) of water levels before and after the dams. In this connection, expensive and reliable hydraulic engineering facilities were required ensuring the operation of each powerful hydraulic power station (HPP). The possibility of serious accidents with the breakthrough of the dam at such facilities by specialists in hydropower engineering should be minimized. Otherwise, the material damage and the inevitable death of people can take huge scales. One of the evidence of this is the data on one of the biggest accidents in the history of the world hydraulic power engineering during the breakthrough of the dam of the Bainjiao reservoir on the Zhuhe River (Henan Province, China, 1975) which resulted in the death of approximately 171,000 people and the number of casualties in the number of 11 million Chinese citizens [2]. This catastrophe at the Chinese HPP for the damage caused to society is comparable to the shock of the entire civilized

world by the atomic bombardment by the USA on August 6, 1945 of the Japanese city of Hiroshima which in one instant was actually completely wiped out with people and their houses from the «face» of our planet [3]. What is the role of HPPs now in the balance of the generation of electricity in the world and in Ukraine? What are the prospects for the development of hydraulic power engineering? We try to answer these questions below.

The goal of the paper is compilation of a brief scientific and technical review on the current state and prospects of development in the world of hydraulic power engineering.

Fig. 1. Impressive and mesmerizing our imagination the power of river water discharged through open water lines in a reinforced concrete dam from an artificially created reservoir of modern HPP [2]

1. Physical basis of hydraulic power engineering. To begin with, we point out that hydraulic power engineering is based on HPPs – power plants which use the potential and kinetic energy of water masses as a stable source of energy [2]. Typically, HPPs are built on high-water rivers building the necessary dams and reservoirs on them. Fig. 2 shows a schematic diagram of the construction of HPPs containing the following main devices [2, 4]: massive reinforced concrete dam with pressure water conduits; a machine hall with hydroelectric units installed in it containing hydraulic turbines and electric generators. A powerful flow of water from the reservoir along the water conduits with the help of blades is directed to the impeller blades of the hydraulic turbine of design shown in Fig. 3. The rotational rotation of the blades of the impeller of this turbine causes corresponding rotation of its vertically mounted massive metal shaft on which the rotor of a hydraulic electric generator rotating normally in the horizontal plane is installed providing a rotating and sinusoidal time-varying high magnetic field with magnetic flux density of about 1 T in the air gap between the rotor and stator of the hydraulic electric generator (see Fig. 3).

Due to the fundamental phenomenon of electromagnetic induction [1] in the stator windings of the hydraulic electric generator spatially and phasically spaced apart from each other by 120°, a three-phase electromotive force and a correspondingly high electrical potential are generated. The presence of this potential ensures the flow of a three-phase AC with frequency of 50 Hz in the primary winding of the transformer

connected on one side to the output terminals of the hydraulic electric generator and, on the other hand, to a high-voltage transmission line supplying electricity to the corresponding consumers. The electrical power of the HPP is determined mainly by the head and the flow of water entering the blades of its hydraulic turbines. To a lesser extent, it depends on the efficiency of hydraulic turbines (up to 80 %) and hydraulic electric generators (up to 98 %) [2, 4]. Due to the fact that the level of water in reservoirs varies during a year according to natural laws, hydraulic power specialists traditionally use the concept of cyclic power of HPP (for example, during the year, month, week and day) [2, 4].
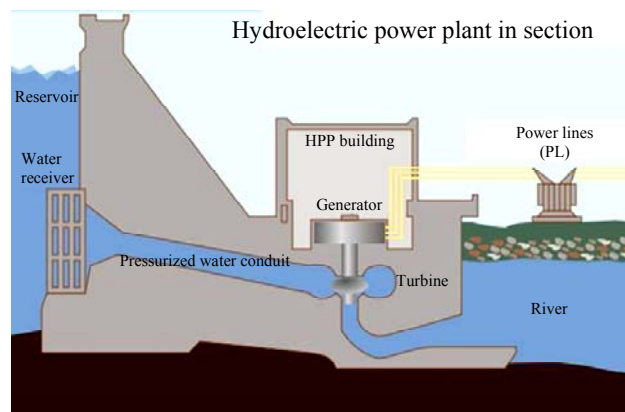
Fig. 2. Schematic diagram of the HPP construction [2]
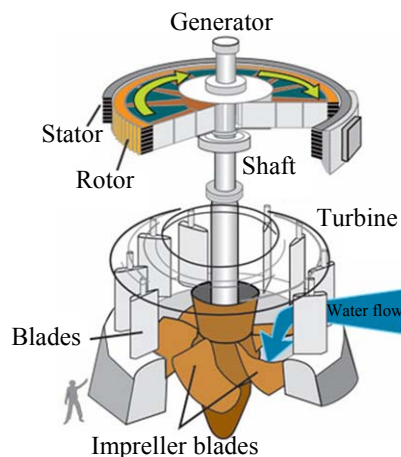
Fig. 3. Block-constructive diagram explaining the principle of operation of a hydraulic turbine and the physical mechanism of generating electrical energy at a modern HPP [2]

1.1. The main classification of HPPs. Depending on the principle of use of renewable natural resources and the way of concentration of water masses, it is possible to single out HPPs of the following type [2, 4]:

• near dams HPPs (reinforced concrete dams, completely blocking the river, raise the level of its water to the required mark, water to the hydraulic turbines comes directly from the river bed);

• dam HPPs (built at higher headings of river water when reinforced concrete dams completely block the river, the building of the HPP is located behind the reinforced concrete dam in its lower part, and water flows to the hydraulic turbines through special pressure tunnels or conduits);

• derivational HPPs (built where the slope of a mountain river is large, the necessary concentration of river water for the efficient operation of its hydraulic turbines is created by non-pressure or pressure derivation (the term «derivation» comes from the Latin word «derivatio» – «diversion» [5]); the type of derivation applied to the HPP (the type of diversion of water from the main river bed) depends on the nature of the slope of the water conduit that supplies river water to the turbine blades);

• pumped storage HPPs (they are built to smooth out peak electrical loads of electricity consumers, water is pumped from the river to a special reinforced concrete upper pool beforehand, and at the appropriate time it is transferred to hydraulic turbines via pressure pipelines from this pool);

• tidal HPPs (usually built in the rocky places of the canyon type with a high level of sea tide reaching up to 19 m in the world [6], a reinforced concrete dam with reversible hydraulic turbines installed at its base in special round canals creates a huge coastal basin of the sea or oceanic water during tide, the energy of this moving water is used by hydraulic turbines both during high tide and low tide);

• wave HPPs (built in the coastal sea area with high waves, this type of HPP transforms the potential energy of sea water pumped by the waves themselves into special containers on the sea surface into electricity).

Depending on the level of water pressure applied to the hydraulic turbines, HPPs are divided into [2, 4]:

• high-pressure HPPs (the level of water pressure in the water conduits to its hydraulic turbines is more than 60 m);

• medium-pressure HPPs (the level of water pressure in the water conduits to its hydraulic turbines from 25 to 60 m);

• low-pressure HPPs (the level of water pressure in the water conduits to its hydraulic turbines from 3 to 25 m).

Depending on the level of electric power generated by hydraulic electric generators, HPPs are divided into the following main types [2, 4]:

• high-power HPPs (their electric power is more than 25 MW);

• medium-power HPPs (their electric power is from 5 to 25 MW);

• low-power HPPs (the electric power produced by them is no more than 5 MW).

1.2. Classification and basic designs of hydraulic turbines. At the HPPs, depending on the level of the water pressure, different designs of hydraulic turbines are used. There are the following types of hydraulic turbines [2, 4]:

• rotary-blade hydraulic turbines (Fig. 4);

• radial-axial hydraulic turbines (Fig. 5);

• bucket hydraulic turbines (Fig. 6).

Fig. 4 shows a general view of a powerful rotary-blade hydraulic turbine for a modern HPP [7]. This type of turbine (Kaplan reactive turbine [7]) is installed at medium-pressure and low-pressure HPPs. Blades of complex shape in this hydraulic turbine can be rotated simultaneously around their horizontal axis, Due to this

and the change in the position of its blades (see Fig. 3), the power produced by the turbine is regulated [7].

Fig. 4. General view of the new modern powerful rotary-blade hydraulic turbine at the time of its installation at the HPP [7]

The flow of water in the rotary-blade hydraulic turbine moves along its axis. The longitudinal axis of this turbine can be located both vertically and horizontally. With the vertical arrangement of the axis, the flow of water before entering the working chamber of the turbine is twisted in a spiral chamber, and then rectified with the help of a fairing. This is necessary for a uniform supply of water to the blades of such a turbine and, accordingly, to reduce its wear.

Fig. 5 represents a general view of the impeller of a powerful radial-axial hydraulic turbine designed for installation at the machine room of the largest in Russia Sayano-Shushenskaya HPP of dam type with installed power up to 6400 MW [2, 4].

Fig. 5. General view of the carried to the HPP impeller to the HPP of a modern powerful radial-axial hydraulic turbine [7]

Radial-axial hydraulic turbines (the Francis reactive turbine [7]) are used in high-pressure HPPs. The water flow in this turbine first moves radially (from the periphery to its center), and then in the axial vertical direction to the outlet from the turbine. This type of hydraulic turbine is used at HPPs with water pressure generated by their dams up to 600 m and their powers up to 640 MW [7]. Of all the known types of hydraulic turbines, radial-axial hydraulic turbines have the highest efficiency. Their disadvantage is a less regular working characteristic than that of rotary-blade hydraulic turbines [4, 7].

Fig. 6 shows a general view of the bucket hydraulic turbine installed on high-pressure HPPs.
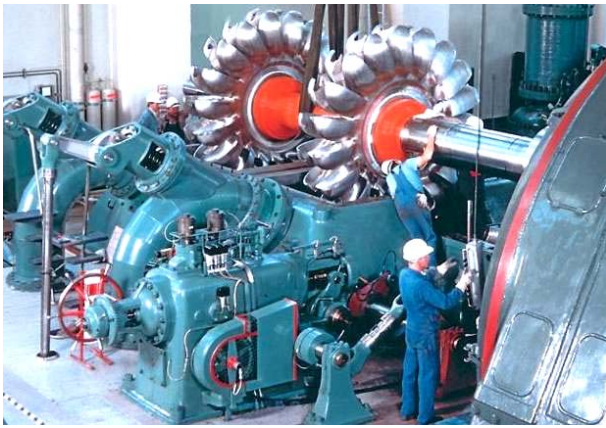
Fig. 6. General view of a bucket hydraulic turbine operating at a high-pressure HPP at the time of its maintenance (to the right of the two bucket hydraulic turbines along the longitudinal axis of the massive steel shaft the body of the hydraulic generator is visible) [7]

Fig. 7. Enlarged view of a new impeller of a modern powerful bucket hydraulic turbine before its installation in the machine room of a high-pressure HPP [10]

Constructively bucket hydraulic turbines (Pelton turbine [7]) are very different from rotary-blade and radial-axial hydro turbines. They, like steam turbines [8], are installed on a horizontal massive steel shaft common with the hydraulic generator. In this type of hydraulic turbine, water is supplied by a large pressure through nozzles (almost like water vapor) along a tangent to the circle passing through the middle of each of its high-strength buckets of special shape placed on both sides of its wheel (see Fig. 6). The jets of water leaving the nozzles at high speed lead to a circular rotation of this hydraulic turbine and the steel shaft of the hydraulic electric generator paired with it. In the bucket hydraulic turbine, the use of the kinetic energy of high-speed jets of river water caused by the dam created by the reservoir with the pressure of water is carried out at atmospheric pressure. Bucket hydraulic turbines (Fig. 7) are used for water pressures of 300 m and more [7, 9]. The power of the bucket hydraulic turbines can reach 200-250 MW with water flow in them up to 100 m^3/s. With a pressure of water up to 700 m (with its excess pressure up to 70 atm), bucket hydraulic turbines compete on HPPs with radial-axial hydraulic turbines. With higher water pressures, their use at HPPs remains uncontested today [7]. The disadvantage of bucket hydraulic turbines is their inefficiency with small pressures and high demands on the river water supplied to them (it should not contain sand and other inclusions that lead to severe wear of the working surfaces of the steel elements of the turbine).

1.3. The main types and characteristics of hydraulic electric generators of HPPs. The hydraulic electric generators used at HPPs with rotary-blade and radial-axial hydraulic turbines are usually a synchronous salient-pole electric machine of vertical design (Fig. 8) driven into rotation from a turbine of a particular design. Note that there are separate designs of low-power hydraulic electric generators of horizontal design including capsular reversible hydraulic electric generators used at tidal HPPs [4, 6]. The hydraulic electric generators with these turbines have a small frequency of circular rotation (up to 500 rpm) and a relatively large outer diameter (up to 20 m) [11]. It is these characteristics that determine the vertical performance of hydraulic

electric generators at all HPPs with rotary-blade and radial-axial hydraulic turbines. With their horizontal design, the rigidity and mechanical strength of elements of similar electrical devices becomes technically not feasible [11]. Hydraulic electric generators of horizontal design are used at HPPs with bucket hydraulic turbines, the rotor speed of which, depending on their pole number (in the presence of 4 or 2 magnetic poles), can reach 1500 or 3000 rpm [8]. Pumped storage HPPs use reversible hydraulic electric generators that operate both in the mode of electricity generation and its consumption during the pumping of river water into the upper basin of such a HPP. They are different from ordinary hydraulic electric generators by a special design of the thrust bearing, allowing their rotor to rotate in both directions [11]. Hydraulic electric generators are designed specifically for the rotational speed and power of hydraulic turbines used at HPPs (for example, for single radial-axial hydro turbines of 640 MW [4, 7]).

Fig. 8. General view of the machine hall of a powerful HPP at the moment of lifting the rotor of one of its large-sized hudraulic electric generators of vertical design [4]

Hydraulic electric generators of HPPs for large unit power (see Fig. 8) are usually installed vertically on the bearings with corresponding guide bearings [11]. They are performed as three-phase ones for frequency of 50 Hz. They use high-efficiency air cooling systems with air-to-water heat exchangers.

2. The largest HPPs in the world. Among the world's largest hydroelectric power stations are the following [2]:

• HPP «Three Gorges» with installed power of 22,400 MW (PRC, Yangtze River, Sandoupin, average annual power generation is 98 billion kWh);

• HPP «Itaipu» with installed power of 14,000 MW (Brazil/Paraguay, Parana, Foz do Iguaçu, average annual power generation at this inter-border station is 92 billion kWh);

• HPP «Silodu» with installed power of 13,900 MW (PRC, Yangtze river, average annual power generation is 64.8 billion kWh);

• HPP «Guri» with installed power of 10,300 MW (Venezuela, Caroni river, average annual power generation is 40 billion kWh);

• HPP «Tukurui» with installed power of 8,300 MW (Brazil, Tokantins River, average annual power generation is 21 billion kWh);

• HPP «Sayano-Shushenskaya» with installed power of 6,400 MW (Russia, the Yenisei River, Sayanogorsk, average annual power generation is 23.5 billion kWh);

• HPP «Krasnoyarskaya» with installed power of 6,000 MW (Russia, the Yenisei River, Divnogorsk, average annual power generation is 20.4 billion kWh);

• HPP «Churchill Falls» with installed power of 5,400 MW (Canada, Churchill River, average annual power generation is 35 billion kWh);

• HPP «Bratskaya» with installed power of 4520 MW (Russia, Angara River, Bratsk, average annual power generation is 22.6 billion kWh).

Fig. 9 shows a general view of the largest in the RF Sayano-Shushenskaya HPP with capacity of 6.4 GW, built on a large Siberian river Yenisei and is a typical dam type (on its photo, descending from a dam of 242 m high down to the machine hall with 10 radial-axial hydraulic turbines of 640 MW each 10 water lines are visible) [4, 7].

The sad statistics in the field of world hydraulic power engineering on our «eyes» also touched upon this modern powerful HPP. On August 17, 2009 at the Sayano-Shushenskaya HPP there was a major accident with large disruptions in the machine hall, which resulted in the death of 75 workers in the power plant [2, 4]. It took about two years to restore it.

Fig. 9. General view of the largest in Russia Sayano-Shushenskaya HPP of dam type with power of 6400 MW (the Yenisei River) [4]

3. The largest pumped storage power plants in the world. In brief, we will focus on hydroelectric power plants whose main purpose is to «remove» peak electrical loads of consumers in their countries' electric power systems (for example, in the evening, when people return home after work and switch on devices that use electricity from the grid). Eliminate the resulting shortage of electricity by increasing the volume of its production at thermal power plants [8], nuclear power plants [12] and conventional hydraulic electric power plants is technically impossible. These power plants for the stability of their power units and, accordingly, the country's energy system as a whole should operate in their «cruising» mode excluding any actions to transfer them to a maneuverable work schedule in a short time. For these purposes, additional energy capacities and resources are needed. One of such resources is pumped storage power plants using their pre-filled upper basins (reservoirs) during the period of peak loads of consumers to generate additional power flows in the power system with the help of hydraulic turbines and hydraulic electric generators at these HPPs, increasing the reliability of its operation [13]. Fig. 10 shows the general view of the reservoir of a pumped storage power plant (near the Missouri River, 80 km from Mississippi, USA), with power of 5.55 billion liters [15]. During the period of peak loads this power plant develops power up to 440 MW.

Fig. 10. Stunning general view from the height of the «bird's eye view» of the huge reinforced concrete reservoir at the top of the remote from the cities of the mountain range of the modern pumped storage power plant «Taum Sauk» (USA) [13]

One of the world's largest pumped storage hydroelectric power plants should be the created since 1983 in Ukraine near the river Dniester (Chernivtsi region) Dniester hydraulic electric power plant with generating power of about 2268 MW (power in the pumping mode is approximately 2847 MW) [14].

4. Hydropower engineering of Ukraine. Domestic hydropower actually began with the construction in the period 1927-1932 on the river Dnieper (Zaporozhye) of the largest at that time in Europe the Dneprovskaya HPP with installed power of 1548 MW [14]. Fig. 11 shows the general view of the hydraulic turbine hall of this HPP.

Fig. 11. Modern view of the hydraulic turbine hall of the Dneprovskaya HPP with installed power of 1548 MW [15]

Fig. 12 shows the general view of the reinforced concrete dam and the machine of the legendary Dneprovskaya HPP which has repeatedly «experienced» in the 20th century joyful and tragic events in its history [4].

Fig. 12. Modern general view of the Dneprovskaya HPP [15]

At present, in the annual balance sheet of power generation in Ukraine, HPPs occupy the third place after nuclear and thermal power plants. The installed power (about 4.7 GW) of all HPPs in the country is approximately 8 % of the total power of the United Energy System of Ukraine [16, 17]. The average annual output of electricity by domestic HPPs is approximately 10.8 billion kWh [18]. The main hydropower potential in the country is concentrated on the base of the Dneprovsky hydro-cascade, including [17]: Dneprovskaya HPP (power is 1548 MW); Kremenchug HPP (power is 682 MW); Kanevskaya HPP (power is 444 MW); Kiev HPP (power is 408 MW); Kakhovskaya HPP (power is 351 MW); Srednedniprovskaya HPP (power is 352 MW). To this should be added Dnestrovskaya-1 HPP (power is 702 MW) as well as a number of pumped storage power plants in Ukraine [16, 17]: Dnestrovskaya (power is 2268 MW); Tashlytsky (power is 302 MW); Kiev (power is 235 MW) should be added. In addition, in Ukraine, 49 so-called small hydraulic power stations operate in rural areas generating up to 200 million kWh of electricity per year [6, 17]. Note that the cost of electricity from HPPs is much lower than from the thermal power plants of Ukraine [2, 4].

5. Advantages and disadvantages of HPPs. The main advantages of HPPs in comparison with other types of power plants are the following [2, 4]:

• the lack of a fuel component in the generation of electricity at HPPs helps to reduce the dependence of the cost of electricity on changes in the world cost of organic fuels;

• use of renewable energy sources at HPPs to produce electricity which contributes to the global efforts of mankind in the fight to reduce emissions of terrestrial greenhouse gases and harmful chemical compounds;

• HPPs are a key element in ensuring the system reliability of the operation of a united electric power system of any country;

• the value of the electricity generated by world's hydroelectric power plants is lower (approximately up to two times) than in other types by traditional power plants;

• the service life of the HPP facilities and power units is higher than at thermal and nuclear power plants (the main reason for this is the absence of high-intensity thermal processes during the generation of electricity in HPPs, the minimum service life of powerful HPPs is 50 years);

• flexibility of HPP operation, associated with a very rapid decrease in the generation of electricity on it, if there is an excess of the latter in the power system (the power units of the HPP can change their operating mode from «cold» start to full electric load acceptance for up to 1.5 minutes);

• low operating costs associated with the presence of a relatively small number of personnel serving the power units at the HPP.

The main shortcomings of the powerful HPPs of the above-mentioned type include the following [2, 19, 20]:

• due to the creation of huge reservoirs in HPPs, it is necessary to flood large areas with fertile lands which causes a number of negative changes in the surrounding nature (the withdrawal of large areas of land from agricultural rotation, the presence of stagnant phenomena in water reservoirs deteriorating the quality of river drinking water, dams of plants overlap the fish path to spawning grounds);

• the cost of building a HPP (at an average world cost of electricity produced up to 5 US cents per kWh) is higher than for thermal and nuclear power plants of the same electrical power;

• major accidents on the dams of powerful hydroelectric power plants inevitably lead to catastrophic floods downstream with severe consequences;

• siltation of the bottom of the HPP reservoirs which inevitably leads to an increase in the external horizontal pressure on the reinforced concrete dam and to the additional formation of methane and greenhouse gases entering the Earth's atmosphere in reservoirs;

• the need to relocate a large number of people living in the future reservoirs of the hydroelectric power station (according to the World Commission on Dams in 2000, the beginning of the construction of the HPP led to the resettlement of up to 60 million people worldwide).

6. Volumes of hydropower generation in the industrialized countries of the world. As of 2012, hydropower engineering provided electricity up to 21% of the total annual electricity production in the world [4, 11]. At that time, the installed power of the world's hydroelectric power plants was about 715 GW. The world leaders in generating electricity at HPPs in its absolute values are currently the PRC, Canada and Brazil. Leaders for the production of electricity at HPPs per citizen are Norway, Iceland and Canada [4]. At the beginning of the 2000s, China was the world's most active hydro-construction, for which hydropower is still the main potential source of energy in the country. It should be noted that now the PRC implements the world's largest program of building new powerful nuclear power plants on its territory [12]. Note that in 1990, the former USSR came second in the world (immediately after the USA) at HPP installed power of 65 GW [4]. Then the USSR for the production of electric power at the hydroelectric power plants with its annual volume of 233 billion kWh occupied the third place in the world after the USA and Canada [11]. At present, Russia, with the installed

capacity of its hydroelectric generating units of 45 GW (the fifth in the world), produces only about 165 billion kWh/year (also the fifth largest in the world) at the hydroelectric power station [4]. Fig. 13 is a structural diagram of the distribution of currently installed power among thermal, nuclear and hydropower plants in Russia [4, 11].
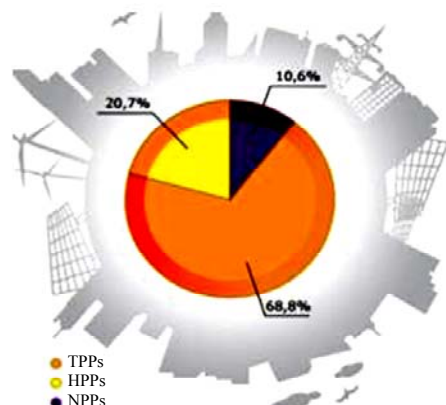

Fig. 13. Structure of distribution of installed power of power plants in the Unified Energy System of Russia for traditional types of electricity generation [4]

From the data in Fig. 13 it can be seen that the share of electricity generated by Russia's hydropower plants in the total volume of its annual production does not exceed 21 %. The bulk of electricity in Russia (about 69 %) is currently being produced at its thermal power plants [4, 8]. Russia's powerful nuclear power plants account for slightly more than 10% of the total annual electricity production. We point out that Russia's hydropower engineering, according to its energy-economic potential, amounting to about 852 billion kWh/year, ranks the second in the world after the PRC [4]. However, in terms of development of its huge hydropower resources, Russia is inferior to virtually all industrialized countries of our world.

7. The problematic tasks of hydropower engineering. The global problem of our civilization is the preservation of a state of the environment that is safe for humanity. In this regard, one of the problematic tasks of the world hydropower engineering, using renewable and environmentally friendly hydropower resources, is to increase the reliability and safety level of hydraulic structures of powerful hydroelectric power plants. These measures should exclude major accidents on the dams of powerful HPPs. Another of its problematic tasks is to minimize the negative environmental consequences from the construction and operation of powerful HPPs. To solve this, large financial investments are required in protective measures to minimize the negative impact of powerful HPPs on the environment. Here, emphasis should be placed on maintaining high quality of water in reservoirs and ensuring the passage in the spring period of fish to their spawning grounds. Hydropower engineering is a relatively highly manoeuvrable energy sub-sector. Therefore, the third problematic task in the field of hydropower engineering is to increase the power of its pumped storage stations in the total power of the power system, including in the United Energy System of Ukraine. In the opinion of hydropower specialists, pumped storage stations should have aggregate power of up to 10-12 % of the total power of all power plants in the country [21]. In this case, when such HPPs are connected to the united power system, optimal passage and regulation of peak electrical loads in the evening time is provided, and a necessary load reserve of the power system is created in emergency situations.

8. Prospects for the development of HPPs in the world and Ukraine. Experts' forecasts point to a steady increase in the world's consumption of electricity and water resources. Thus, according to the available forecasts, the world consumption of electricity in the period from 2000 to 2300 will double in size [21]. In this regard, the role of hydropower engineering in the countries where there are undeveloped hydropower resources is also increasing. It should be noted that as of 2007, in which the world's HPPs generated in the amount of about 3,050 billion kWh, the untapped hydropower potential in the world was about 5,680 billion kWh [21]. Between the continents of our planet, this energy potential was distributed as follows [21]: Asia – 3380 billion kWh (60 %); South America – 930 billion kWh (16 %); Africa – 750 billion kWh (13 %); North and Central Americas – 350 billion kWh (6 %); Europe – 220 billion kWh (4 %); Australia and Oceania – 50 billion kWh (1 %). In Ukraine, the hydropower potential of flat rivers has been used almost completely [18]. Therefore, for Ukraine, the development of the hydraulic storage of energy, whose energy potential can fully ensure the country's energy system in the deficit of «peak» electricity, is now topical. According to [21], the undeveloped hydropower potential is located mainly in the underdeveloped and developing countries of the world. When planning the development of energy in these countries, first of all, it is planned to develop its hydro resources. The forecasts for the development of the world power engineering up to 2030 indicate that the share of hydropower (up to 21 %) in the world energy balance will remain so far [21].

Conclusions.

1. The completed scientific and technical review of the development of the world hydropower engineering indicates that HPPs in the industrialized countries occupy the third place in terms of the annual volume of electricity they produce (up to 21 % of the world's generation) in the industrialized countries after powerful thermal and nuclear power plants. The main reserve of hydropower resources, which has not been currently available in the world (up to 3380 billion kWh), is concentrated in the countries of Asia.

2. Hydropower engineering with its relatively manoeuvrable power units using only renewable and environmentally friendly water energy resources is capable, through the construction of powerful pumped storage power plants, to unload the peak loads of consumers in power systems in the evening and create load reserves to increase the stability of the functioning of power systems in emergency operation modes.

3. In order to protect and preserve the environment on the Earth, it is necessary to improve the environmental safety of the existing and newly created powerful conventional HPPs and pumped storage plants in the world.

4. In the near future, hydropower engineering will continue, together with heat and nuclear power engineering, to remain the main sources of electricity for the developing civilization on our planet.

REFERENCES
1. Kuz'michev V.E. *Zakony i formuly fiziki* [Laws and formulas of physics]. Kiev, Naukova Dumka Publ., 1989. 864 p. (Rus).
2. Available at: https://ru.wikipedia.org/wiki/Гидроэлектростанция (accessed 13 May 2017). (Rus).
3. Baranov M.I. An anthology of the distinguished achievements in science and technique. Part 40: The scientific opening of the method of explosive implosion for the obtaining above critical mass of nuclear charge and Ukrainian «track» in the «Manhattan» American atomic project. *Electrical engineering & electromechanics*, 2017, no.5, pp. 3-13. **doi: 10.20998/2074-272X.2017.5.01.**
4. Available at: http://greenevolution.ru/enc/wiki/gidroelektrostanciya-ges (accessed 22 June 2016).
5. *Bol'shoj illjustrirovannyj slovar' inostrannyh slov* [Large illustrated dictionary of foreign words]. Moscow, Russkie slovari Publ., 2004. 957 p. (Rus).
6. Baranov M.I. An anthology of the distinguished achievements in science and technique. Part 32: Alternative energy: state and prospects of development. *Electrical engineering & electromechanics*, 2016, no.3, pp. 3-16. **doi: 10.20998/2074-272X.2016.3.01.**
7. Available at: http://www.cshp.ru/gidroenergetika/eto-interesno/tipyi-gidroturbin (accessed 05 May 2017).
8. Baranov M.I. An anthology of the distinguished achievements in science and technique. Part 43: Traditional power engineering. Thermal power plants: state and prospects of their development. *Electrical engineering & electromechanics*, 2018, no.2, pp. 3-10. **doi: 10.20998/2074-272X.2018.2.01.**
9. Available at: http://blog.rushydro.ru/?p=4158 (accessed 15 April 2016). (Rus).
10. Available at: http://elektrogenerator.net/smallhydropower/pelton_turbines.html (accessed 05 September 2016). (Rus).
11. Available at: http://bibliofond.ru/view.aspx?id=657541 (accessed 26 October 2016). (Rus).
12. Baranov M.I. An anthology of the distinguished achievements in science and technique. Part 44: Traditional power engineering. Nuclear power stations: retrospective view, state and prospects of their development. *Electrical engineering & electromechanics*, 2018, no.3, pp. 3-16. **doi: 10.20998/2074-272X.2018.3.01.**
13. Available at: http://electricalschool.info/energy/1911-princip-raboty-gidrojelektrostancii.html (accessed 05 May 2014). (Rus).
14. Available at: http://frend.org.ua/post138322582 (accessed 22 July 2016). (Rus).
15. Available at: https://en.wikipedia.org/wiki/Dnieper_Hydroelectric_Station (accessed 12 May 2017).
16. Available at: https://ru.wikipedia.org/wiki/Список_гидроэлектростанций_Украины (accessed 02 February 2017). (Rus).
17. Available at: https://uk.wikipedia.org/wiki/Гідроенергетика_України (accessed 12 June 2017). (Ukr).
18. Available at: http://mpe.kmu.gov.ua/minugol/control/uk/publish/article?art_id=93710&cat_id=35082 (accessed 10 May 2015). (Ukr).
19. Available at: http://myelectro.com.ua/98-gidroenergetika/111-glavnye-dostoinstva-i-nedostatki-gidroelektrostantsij (accessed 10 October 2015). (Rus).
20. Neporozhniy P.S., Obrezkov V.I. *Vvedenie v spedsial'nost': gidroelekroenergetika* [Introduction to the specialty: Hydropower]. Moscow, Energoizdat Publ., 1982. 304 p. (Rus).
21. Available at: http://energetika.in.ua/ua/books/book-3/part-2/section-6/Розділ 6 (accessed 15 September 2016). (Rus).

M.I. Baranov, Doctor of Technical Science, Chief Researcher,
Scientific-&-Research Planning-&-Design Institute «Molniya»
National Technical University «Kharkiv Polytechnic Institute»,
47, Shevchenko Str., Kharkiv, 61013, Ukraine,
phone +380 57 7076841,
e-mail: baranovmi@kpi.kharkov.ua

M. Benkahla, R. Taleb, Z. Boudjema

A NEW ROBUST CONTROL USING ADAPTIVE FUZZY SLIDING MODE CONTROL FOR A DFIG SUPPLIED BY A 19-LEVEL INVERTER WITH LESS NUMBER OF SWITCHES

This article presents the powers control of a variable speed wind turbine based on a doubly fed induction generator (DFIG) because of their advantages in terms of economy and control. The considered system consists of a DFIG whose stator is connected directly to the electrical network and its rotor is supplied by a 19-level inverter with less number of switches for minimize the harmonics absorbed by the DFIG, reducing switching frequency, high power electronic applications because of their ability to generate a very good quality of waveforms, and their low voltage stress across the power devices. In order to control independently active and reactive powers provided by the stator side of the DFIG to the grid and ensure high performance and a better execution, three types of robust controllers have been studied and compared in terms of power reference tracking, response to sudden speed variations, sensitivity to perturbations and robustness against machine parameters variations. References 34, tables 4, figures 13.
Key words: **wind turbine, doubly fed induction generator, sliding mode controller, adaptive sliding mode controller, adaptive fuzzy sliding mode controller, multilevel inverter.**

В статье описывается управление мощностью ветряной турбины переменной скорости на основе асинхронного генератора двойного питания ввиду их преимуществ с точки зрения экономичности и управления. Рассматриваемая система состоит из асинхронного генератора двойного питания, статор которого подключен непосредственно к электрической сети, а его ротор питается от 19-уровневого инвертора с меньшим количеством коммутаторов для минимизации гармоник, поглощаемых генератором, уменьшая частоту переключения, и устройств силовой электроники вследствие их способности генерировать высокое качество сигналов и низкого уровня напряжения на них. Чтобы независимо управлять активной и реактивной мощностью, подаваемой стороной статора указанного генератора в сеть, и обеспечивать высокую производительность и лучшее конструктивное исполнение, изучены и сопоставлены три типа робастных контроллеров с точки зрения отслеживания мощности, реакции на внезапное изменение скорости, чувствительности к возмущениям и устойчивости к изменениям параметров машины. Библ. 34, табл. 4, рис. 13.
Ключевые слова: **ветряная турбина, асинхронный генератор двойного питания, контроллер режима скольжения, адаптивный контроллер режима скольжения, адаптивный нечеткий контроллер режима скольжения, многоуровневый инвертор.**

Introduction. Wind energy has the most contribution for power generation among different renewable energy resources; this is so because of its potential advantageous such as free availability of wind, ability to exploit in high power, other land around uses of wind farms and as the important one it is relatively inexpensive to build wind farm [1]. The wind energy community has dedicated a huge effort to develop improved condition monitoring strategies. Fault detection and isolation schemes and fault tolerant control strategies applicable to wind turbines (WT) [2].

Wind power has established itself as a main source for the generation of electricity in the past decade by delivering at least 3.4% of the world's electricity in 2014, a figure expected to increase to 6-8 % by 2020 and to 8-17 % by 2030 [3, 4].

In the development of WT technologies doubly fed induction generators (DFIG) are the most popular due to their numerous advantages including independent control of both active and reactive powers, variable speed operation, four-quadrant active and reactive power capabilities, high energy efficiency, and low size converters [5-8]. These advantages are achieved through controlling the rotor voltage or current by a converter while the stator is directly connected to the grid [9].

Research on the control and operation for DFIG under distorted grid voltage conditions has been studied in [10]. Studied in this paper is shown in Fig. 1. In this diagram, mechanical energy is produced by a WT and provided to a DFIG through a gear box. The back-to-back control system and voltage source converters comprise rotor-side and grid-side converters. The grid side converter (GSC) is used to control the DC-link voltage and reactive power exchanged with the grid and is connected to the grid via three chokes to improve the current harmonic distortion. The rotor side converter (RSC) is used to control the generator speed and reactive power [11]. The RSC controls the generator to achieve maximum power point tracking. In one classification, the control approaches of the DFIG are categorized in two groups: classic control approaches using PI regulators and advanced control approaches.
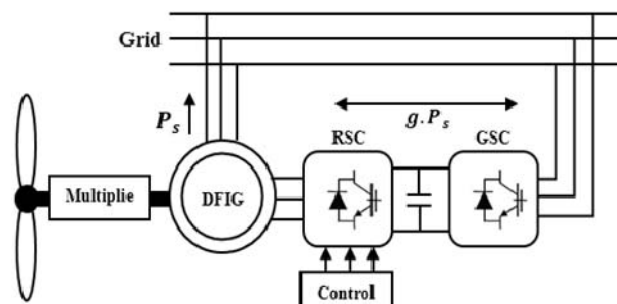
Fig. 1. Diagram of a wind energy conversion system

High power applications in electrical traction require high voltage supply for motors. The only way to use multilevel converters is actually to generate voltages with high magnitudes [12].

Several topologies of multilevel inverters have been studied and presented. Among them, neutral point clamped inverters [13], flying capacitors inverters also called imbricated cells [14], and series connected cells inverters also called cascaded inverters [15]. The industry often has used the neutral-point-clamped inverter [16].

However, the topology that uses series connected cells inverters presents some advantages, as smaller voltage rate (*dU/dt*) due to existence of higher number levels, producing less common-mode voltage across motor windings [17]. Furthermore, this topology is simple and its modular configuration makes it easily extensible for any number of desired output voltage levels. Fig. 2,*a*. shows the basic diagram of this topology with *k* partial cells represented by Fig. 2,*b*. The *J*th single-phase inverter is supplied by a DC-voltage source $U_{dj}(j = 1…k)$. The relationship between the number of series-connected single-phase inverters in each phase and the number of output voltage levels generated by this topology, respectively *k* and *N*, is given by: $N = 2k + 1$, in the case where there are equal voltages in all partial inverters.
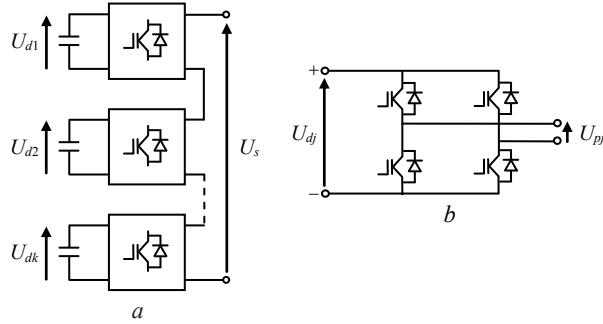
Fig. 2. *a* – a series-connected multilevel inverter topology with *k* partial cells, *b* – partial cell configuration

In all the well-known multilevel converter topologies, the number of power devices required depends on the output voltage level needed [18]. However, increasing the number of power semiconductor switches also increases the converter circuit and control complexity and the costs. To provide a large number of output levels without increasing the number of converters, a uniform step asymmetrical multilevel inverters (USAMI) can be used [19].

The sliding mode control achieves robust control by adding a discontinuous control signal across the sliding surface, satisfying the sliding condition. Nevertheless, this type of control has an essential disadvantage, which is the chattering phenomenon caused by the discontinuous control action. To treat these difficulties, several modifications to the original sliding control law have been proposed, the most popular being the boundary layer approach [20, 21].

The disadvantages of the structure are complex network structure and inference mechanism. Therefore, to overcome the disadvantages of the aforementioned sliding mode controller (SMC), a new adaptive sliding mode controller (ASMC) is developed to estimate the unknown bound of uncertainty which is obtained in the sense of Lyapunov stability theorem to minimize the control effort and attenuate chattering [22], robustness and rapidity [23]. In addition, estimating the disturbance in terms of the sliding function dynamics is that, it results in a simple linear dynamics and hence the estimator can be made simple [24]. And scheme guarantees asymptotic convergence of states and external disturbances [25]. An adaptive sliding mode controller is developed to track the speed for maximum power extraction.

In order to reduce the chattering problem in SMC, a small boundary layer around the sliding surface. However this method can lead to solve the chattering problem but usually there exist a finite steady state error and so asymptotical convergence is lost. As another solution, adaptive fuzzy sliding mode control (AFSMC) [26]. An

AFSMC was proposed by combining the tuning online characteristic of an AFC and the robust characteristic of a conventional SMC. In an AFSMC, the controller includes two parts: a fuzzy equivalent controller designed based on an AFC scheme and a reaching controller based on a SMC scheme [27]. An AFSMC that control the uncertain nonlinear chaotic systems and unknown robotic systems [28], the controller proposed is composed of two terms: an auxiliary control law which is designed to compensate and uncertainties of parameters and a primary control law which ensure a good tracking. Another advantages of this controller is the using of Lyapunov approach to guarantee the stability and convergence analysis [29]. As another solution to eliminate chattering phenomenon and achieve zero steady state error [26].

System modeling. The WT model. For a horizontal axis wind turbine, the output mechanical power extracted from the wind is given by [30]:

$$P_t = \frac{1}{2} P_{Coef}(\lambda, \beta)\pi R^2 \rho v^3, \quad (1)$$

where P_{Coef} is the power coefficient which is a function of both tip speed ratio λ, and blade pitch angle β (deg), and v is the wind speed (m/s), ρ is the air density (kg/m³), and *R* is the radius of the turbine (m). In this work the P_{Coef} equation is approximated using a non-linear function according to [31]:

$$P_{Coef} = (0.5 - 0.167)(\beta - 2)\sin\left[\frac{\pi(\lambda + 0.1)}{18.5 - 0.3(\beta - 2)}\right] - \quad (2)$$
$$- 0.0018(\lambda - 3)(\beta - 2).$$

The tip speed ratio is given by:

$$\lambda = \Omega_t R / v, \quad (3)$$

where Ω_t is the angular velocity of WT.

Proposed 19-level USAMI. Multilevel inverters generate at the AC-terminal several voltage levels as close as possible to the input signal. The output voltage step is defined by the difference between two consecutive voltages. A multilevel converter has a uniform or regular voltage step, if the steps Δu between all voltage levels are equal. In this case the step is equal to the smallest DC-voltage, u_{d1} [32]. This can be expressed by

$$u_{d1} = \Delta u = u_{s2} - u_{s1} = u_{s3} - u_{s2} = ... = u_{sN} - u_{s(N-1)} \quad (4)$$

If this is not the case, the converter is called a non uniform step CHBAMI or irregular CHBAMI. An USCHBAMI is based on DC-voltage sources to supply the partial cells (inverters) composing its topology which respects to the following conditions:

$$\begin{cases} u_{d1} \leq u_{d2} \leq ... \leq u_{dk}; \\ u_{dj} \leq 1 + 2\sum_{l=1}^{j-1} u_{dl}, \end{cases} \quad (5)$$

where *k* represents the number of partial cells per phase and $j = 1…k$.

The number of output voltage levels depends on the number of cells per phase and on the corresponding supplying DC-voltages. Equation 6 shows that in certain cases, there are many possibilities for setting the partial DC-voltages to obtain the same number of levels. These possible redundant solutions are another degree of freedom for the designer

$$N = 1 + 2\sigma_k \text{ where } \sigma_k = \sum_{j=1}^{k} u_{dj}. \quad (6)$$

Table 1 gives some examples of the DC-voltages which can be set and the corresponding number of output voltage levels which can be obtained. In this example there are $k = 3$ series-connected single-phase inverters per phase.

Table 1
Examples of unequal DC-voltages in a 3 cells USAMI

u_{d1} (p.u.)	u_{d2} (p.u.)	u_{d3} (p.u.)	N
1	1	2	9
1	1	3	11
1	2	2	
1	1	4	13
1	2	3	
1	1	7	
1	2	6	19
1	3	5	

Among several modulation strategies, the multi-carrier sub-harmonic PWM technique has been receiving an increasing attention for symmetrical multilevel converters [33]. This modulation method can also be used to control asymmetrical multilevel power converters.

The SPWM is also known as the multi-carrier PWM because it relies on a comparison between a sinusoidal reference waveform and vertically shifted carrier waveforms $N-1$ carriers are therefore required to generate N levels. The carriers are in continuous bands around the zero reference. They have the same amplitude A_c and the same frequency f_c. The sine reference waveform has a frequency f_r and an amplitude A_r. At each instant, the result of the comparison is 1 if the triangular carrier is greater than the reference signal and 0 otherwise. The output of the modulator is the sum of the different comparisons which represents the voltage level. The strategy is therefore characterized by the two following parameters, respectively called the modulation index and the modulation rate:

$$m = f_c / f_r ; \qquad (7)$$

$$r = \frac{2}{N-1} \cdot \frac{A_r}{A_c} . \qquad (8)$$

The reference voltages are given as follows:

$$\begin{cases} u_{ri} = u_{rmax} \sin(2\pi f_r t - (j-1)2\pi/3); \\ (i, j) \in \{(a,1), (b,2), (c,3)\}. \end{cases} \qquad (9)$$

We propose to develop a 19-level USAMI composed of $k = 3$ partial inverters per phase with the following DC-voltage sources: $u_{d1} = 1p.u$, $u_{d2} = 3p.u$ and $u_{d3} = 5p.u.$. For this configuration (1, 3, 5), the total harmonic distortion (THD) of output voltage is smaller than configurations (1, 1, 7) and (1, 2, 6). Fig. 3 shows the output voltage in each partial inverter and the 19-level USAMI output voltage V_a in the first leg.
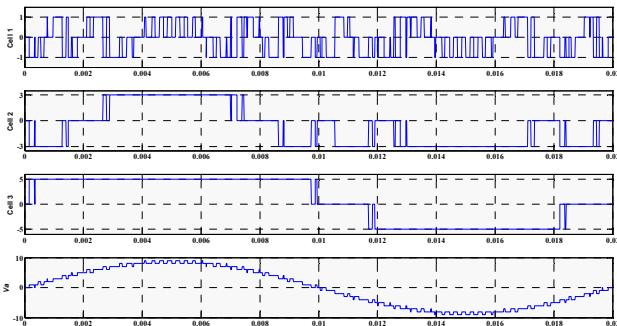
Fig. 3. Output voltages of the partial H-bridges, and total output voltage of the 19-level USAMI

Doubly fed induction generator modeling. The dynamic voltages and fluxes equations of the DFIG in a synchronous reference frame (d-q) rotating at an angular speed of ω_s. The stator and rotor voltages are given, respectively, as follows:

$$\begin{cases} V_{ds} = R_s I_{ds} + \dfrac{d}{dt}\psi_{ds} - \omega_s\psi_{qs}; \\ V_{qs} = R_s I_{qs} + \dfrac{d}{dt}\psi_{qs} + \omega_s\psi_{ds}; \\ V_{dr} = R_r I_{dr} + \dfrac{d}{dt}\psi_{dr} - \omega_r\psi_{qr}; \\ V_{qr} = R_r I_{qr} + \dfrac{d}{dt}\psi_{qr} + \omega_r\psi_{dr}; \end{cases} \quad \begin{cases} \psi_{ds} = L_s I_{ds} + M I_{dr}; \\ \psi_{qs} = L_s I_{qs} + M I_{qr}; \\ \psi_{dr} = L_r I_{dr} + M I_{ds}; \\ \psi_{qr} = L_r I_{qr} + M I_{qs}. \end{cases} \quad (10)$$

The stator and rotor angular velocities are linked by the following relation: $\omega_s = \omega + \omega_r$. The generator mechanical and electromagnetic torques (C_{em} and C_r) are related, if the viscous friction coefficient is taken into account, as follows:

$$C_{em} = C_r + J\frac{d\Omega}{dt} + f\Omega , \qquad (11)$$

where the electromagnetic torque C_{em} is defined by:

$$C_{em} = p\frac{M}{L_s}(\psi_{qs}I_{dr} - \psi_{ds}I_{qr}) . \qquad (12)$$

Field oriented control of the DFIG. In order to easily control the production of electricity by the wind turbine, we will carry out an independent control of active and reactive powers by orientation of the stator flux. By choosing a diphase reference frame d-q related to the stator spinning field pattern and aligning the stator vector flux with the axis d, we can write

$$\psi_{ds} = \varphi_s \quad \text{and} \quad \psi_{qs} = 0. \qquad (13)$$

The electromagnetic torque becomes:

$$C_{em} = -p\frac{M}{L_s}I_{qr}\psi_{ds} . \qquad (14)$$

The following rotor flux and the stator voltage can be rewritten as:

$$\begin{cases} \psi_s = L_s I_{ds} + M I_{dr}; \\ 0 = L_s I_{qs} + M I_{qr}. \end{cases} \qquad (15)$$

$$\begin{cases} V_{ds} = 0; \\ V_{qs} = \omega_s\psi_s. \end{cases} \qquad (16)$$

By supposing that the electrical supply network is stable, having for simple voltage V_S, which led to a stator flux ψ_S constant. This consideration associated with Equation (15) shows that the electromagnetic torque only depends on the q-axis rotor current component. Using Equation (16), a relation between the stator and rotor currents can be established

$$\begin{cases} I_{ds} = -\dfrac{M}{L_s}I_{dr} + \dfrac{\psi_s}{L_s}; \\ I_{qs} = -\dfrac{M}{L_s}I_{qr}. \end{cases} \qquad (17)$$

The stator active and reactive powers are written

$$\begin{cases} P_s = V_{ds}I_{ds} + V_{qs}I_{qs}; \\ Q_s = V_{qs}I_{ds} - V_{ds}I_{qs}. \end{cases} \qquad (18)$$

By using Equation (10), (16-18), the statoric active and reactive power, the rotoric fluxes and voltages can be written versus rotoric currents as

$$\begin{cases} P_s = -\dfrac{\omega_s \psi_s M}{L_s} I_{qr}; \\ Q_s = -\dfrac{\omega_s \psi_s M}{L_s} I_{dr} + \dfrac{\omega_s \psi_s^2}{L_s}. \end{cases} \quad (19)$$

$$\begin{cases} \psi_{dr} = (L_r - \dfrac{M^2}{L_s}) I_{dr} + \dfrac{M \psi_s}{L_s}; \\ \psi_{qr} = (L_r - \dfrac{M^2}{L_s}) I_{qr}. \end{cases} \quad (20)$$

$$\begin{cases} V_{dr} = R_r I_{dr} + (L_r - \dfrac{M^2}{L_s}) \dfrac{dI_{dr}}{dt} - g\omega_s (L_r - \dfrac{M^2}{L_s}) I_{qr}; \\ V_{qr} = R_r I_{qr} + (L_r - \dfrac{M^2}{L_s}) \dfrac{dI_{qr}}{dt} + g\omega_s (L_r - \dfrac{M^2}{L_s}) I_{dr} + g\omega_s \dfrac{M\psi_s}{L_s}. \end{cases} \quad (21)$$

In steady state, the second derivative terms of the two equations in 21 are nil.

We can thus write:

$$\begin{cases} V_{dr} = R_r I_{dr} - g\omega_s (L_r - \dfrac{M^2}{L_s}) I_{qr}; \\ V_{qr} = R_r I_{qr} + g\omega_s (L_r - \dfrac{M^2}{L_s}) I_{dr} + g\omega_s \dfrac{M\psi_s}{L_s}. \end{cases} \quad (22)$$

The third term, which constitutes cross-coupling terms, can be neglected because of their small influence. These terms can be compensated by an adequate synthesis of the regulators in the control loops.

With the hypothesis that led to a stator flux ψ_S constant, the electrical supply network is stable, having for simple voltage V_S.

Control strategies of the DFIG. In this section, we have chosen to compare the performances of the DFIG with three different nonlinear controllers: SMC, ASMC and AFSMC. The control system can be designed as shown in Fig. 4. Based on Equations (18) and (21), the blocks R_P, R_Q, R_{Iqr} and R_{Idr} represent respectively the stator powers and the rotor currents regulators.
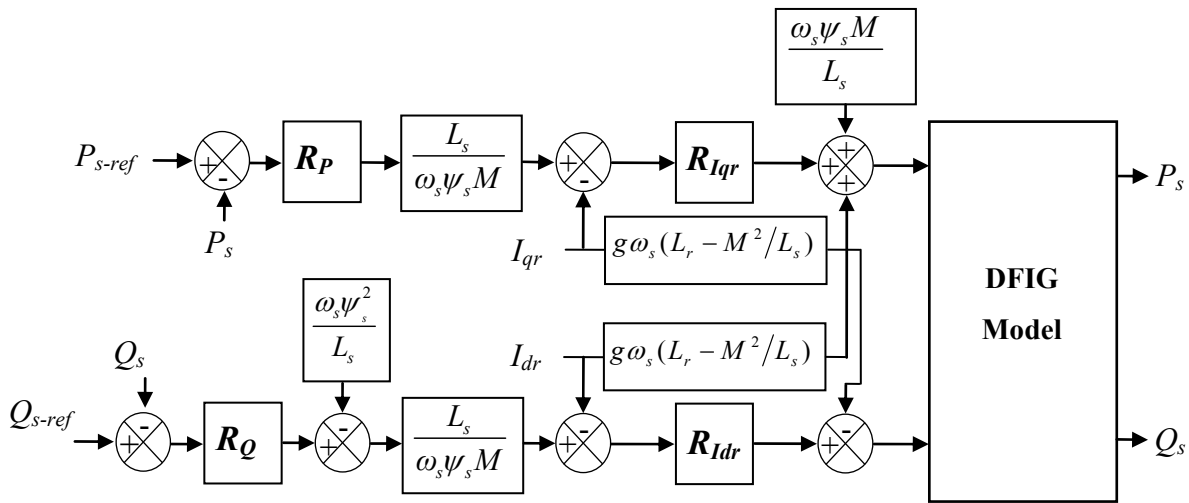
Fig. 4. Power control of the DFIG

Sliding mode controller synthesis. The sliding mode technique is developed from variable structure control to solve the disadvantages of other designs of nonlinear control systems. The sliding mode is a technique to adjust feedback by previously defining a surface. The system which is controlled will be forced to that surface, then the behavior of the system slides to the desired equilibrium point. The control function will satisfy reaching conditions in the following form:

$$V_{com} = V_{eq} + K \cdot \mathrm{sat}\big(S(x)/\delta\big). \quad (23)$$

K is a constant and is chosen to compensate for uncertainties and disturbances, sat($S(x)/\delta$) is the proposed saturation function, is the boundary layer thickness. In this paper we propose the Slotine method

$$S(X) = \left(\dfrac{d}{dt} + \lambda\right)^{n-1} e, \quad (24)$$

here e is the tracking error vector, λ is a positive coefficient and n is the relative degree.

In our study, the control of the active stator power P_S and reactive stator power Q_S to their references P_{S_ref} and Q_{S_ref} respectively. The SMC control scheme is shown in Fig. 5, we choose the error between the measured and references stator powers as sliding mode surfaces, so we can write the following expression

$$\begin{cases} S_d = P_{S\_ref} - P_S; \\ S_q = Q_{S\_ref} - Q_S. \end{cases} \quad (25)$$
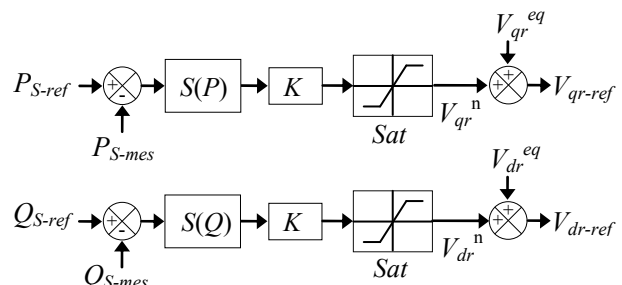
Fig. 5. Block diagram of the sliding mode controller (SMC)

The first order derivate of (25) gives

$$\begin{cases} \dot{S}_d = \dot{P}_{S\_ref} - \dot{P}_S; \\ \dot{S}_q = \dot{Q}_{S\_ref} - \dot{Q}_S. \end{cases} \quad (26)$$

Replacing the powers in (26) by their expressions given in (19), one obtains

$$\begin{cases} \dot{S}_d = \dot{P}_{S\_ref} - \dfrac{\omega_s \psi_s M}{L_s} \dot{I}_{qr}; \\[3mm] \dot{S}_q = \dot{Q}_{S\_ref} - \dfrac{\omega_s \psi_s M}{L_s} \dot{I}_{dr} - \dfrac{\omega_s \psi_s^2}{L_s}. \end{cases} \quad (27)$$

V_{dr} and V_{qr} will be the two components of the control vector used to constraint the system to converge to $S_{dq} = 0$. The control vector V_{dqeq} is obtained by imposing $\dot{S}_{dq} = 0$. So the equivalent control components are given by the following relation

$$V_{eqdq} = \begin{bmatrix} -\dfrac{L_s\left(L_r - \dfrac{M^2}{L_s}\right)}{\omega_s \psi_s M}\dot{Q}_s^* + R_r I_{dr} - \left(L_r - \dfrac{M^2}{L_s}\right)g\omega_s I_{qr} + \dfrac{\left(L_r - \dfrac{M^2}{L_s}\right)\psi_s}{M} \\[4mm] \dfrac{L_s}{\omega_s \psi_s M}\dot{P}_s^* + R_r I_{qr} - \left(L_r - \dfrac{M^2}{L_s}\right)g\omega_s I_{dr} + \dfrac{g\omega_s \psi_s M}{L_s} \end{bmatrix} \quad (28)$$

To obtain good performances, dynamic and commutations around the surfaces, the control vector is imposed as follows

$$V_{dq} = V_{eqdq} + K \cdot \text{sat}\left(S_{dq}\right). \quad (29)$$

The sliding mode will exist only if the following condition is met

$$S\dot{S} < 0. \quad (30)$$

Adaptive sliding mode controller. The main obstacles for application of sliding mode control are two phenomena: high activity of control action and chattering. In this section we propose an adaptive sliding mode controller whose switching gain is adapted based on the disturbance estimation, this control proposed in [34]. The ASMC could be considered as an advance version of basic sliding mode control that is also in the topics of many advance control studies. The ASMC control scheme is shown in Fig. 6. This method is often used low overshoot, low setting time, and robustness against disturbance, chattering reduction, no need for the prior knowledge of uncertainty bound, minimum control effort. The control input in the ASMC is given in

$$V_{com} = V_{eq} + V_{ASMC}. \quad (31)$$
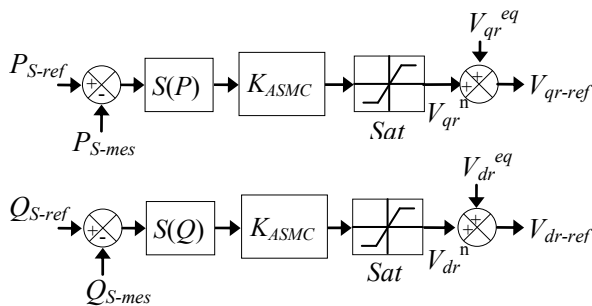
Fig. 6. Block diagram of the adaptive sliding mode control (ASMC)

V_{ASMC} is obtained by

$$V_{ASMC} = K_{asmc}(t)\text{sat}\left(S(x)/\delta\right), \quad (32)$$

where $K_{asmc}(t)$ is the reaching gain which is achieved by adaptation law

$$\dot{K}_{asmc}(t) = -\gamma\|s\|, \quad (33)$$

where γ is a positive constant and $K_{asmc}(t)$ is the adaptive controller gain. This control law makes $K_{asmc}(t)$ to increase until the system reaches the switching manifold. Whenever $S = 0$ is not reachable in practical SMC which causes an increasing $K_{asmc}(t)$ and high gain introduces

chattering. Further, $\dot{K}_{asmc}(t) = 0$ which results in saturation of the control gain $K_{asmc}(t)$.

Adaptive fuzzy sliding mode controller. The disadvantage of sliding mode controllers is that the discontinuous control signal produces chattering. In order to eliminate the chattering phenomenon, we propose to use the adaptive fuzzy sliding mode control. This paper proposes an AFSMC which is designed to control the active and reactive power of the DFIG shown in Fig. 7. Besides advantage of stability and robustness and convergence of the control system are guaranteed by using the Lyapunov method. This control following from

$$V_{com} = V_{eq} + V_{AFSMC}. \quad (34)$$

V_{AFSMC} is obtained by

$$V_{AFSMC} = K_{asmc}(t)V_{Fuzzy}; \quad (35)$$

$$V_{Fuzzy} = \text{sat}\left(S(x)/\delta\right). \quad (36)$$
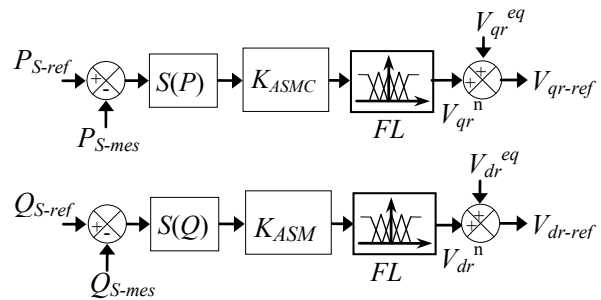
Fig. 7. Block diagram of the Adaptive Fuzzy Sliding Mode Control (AFSMC)

The fuzzy sliding mode controller (FSMC) is a modification of the sliding mode controller, where the switching controller term $\text{sat}(S(x)/\delta)$, and $K_{asmc}(t)$ is obtained by Equation (33), the universes of discourses are first partitioned into the seven linguistic variables NB, NM, NS, EZ, PP, PM, PG, triangular membership functions are chosen to represent the linguistic variables and fuzzy singletons for the outputs are used. The fuzzy rules that produce these control actions are reported in Table 2.

Table 2

Matrix of inference

E	NB	NM	NS	EZ	PS	PM	PB
NB	NB	NB	NB	NB	NM	NS	EZ
NM	NB	NB	NB	NM	NS	EZ	PS
NS	NB	NB	NM	NS	EZ	PS	PM
EZ	NB	NM	NS	EZ	PS	PM	PB
PS	NM	NS	EZ	PS	PM	PB	PB
PM	NS	EZ	PS	PM	PB	PB	PB
PB	EZ	PS	PM	PB	PB	PB	PB

We use the following designations for membership functions: **NB**: Negative Big, **NS**: Negative Small, **PS**: Positive Small, **PB:** Positive Big, **NM**: Negative Middle, **EZ**: Equal Zero, **PM**: Positive Middle. These choices are described in Fig. 8.

Simulation results and discussions. In this section, simulation are realized with a 7.5 KW generator coupled to a 380V/50Hz grid. Parameters of the machine are given in Appendix A. With an aim to evaluate the performances of the three controllers: SMC, ASMC and AFSMC, three

types of tests have been realized: reference tracking, sensitivity to the speed variation and robustness against machine parameter variations.
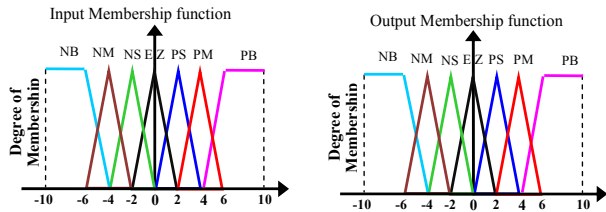
Fig. 8. Fuzzy sets and its memberships functions

Reference tracking. This goal of this test is the study of the behavior of the three controllers in reference tracking, while the machine's speed is considered constant and equal to its nominal value. Simulation results are presented in Fig. 9. As it's shown by this Figure, for the

three controllers, the stator active and reactive generated powers tracks almost perfectly their reference and ensures a perfect decoupling between the two axes. Therefore it can be considered that the three types or controllers have a very good performance for this test. On the other hand, Fig. 10 shows the harmonic spectrum of one phase stator current of the DFIG obtained using Fast Fourier Transform (FFT) technique for the three controllers. It can be clear observed that the THD is reduced for AFSMC supplied by 19-level USAMI (THD = 0.67 %) when compared to AFSMC (THD = 1.79 %) and ASMC (THD = 1.91 %) and SMC (THD = 2.06 %) supplied by conventional inverter (i.e. 2-level inverter). Therefore it can be concluded that proposed controller (AFSMC) supplied by 19-level USAMI is the most effective in eliminating chattering phenomenon and to reduce the current harmonics.

Fig. 9. Reference tracking test
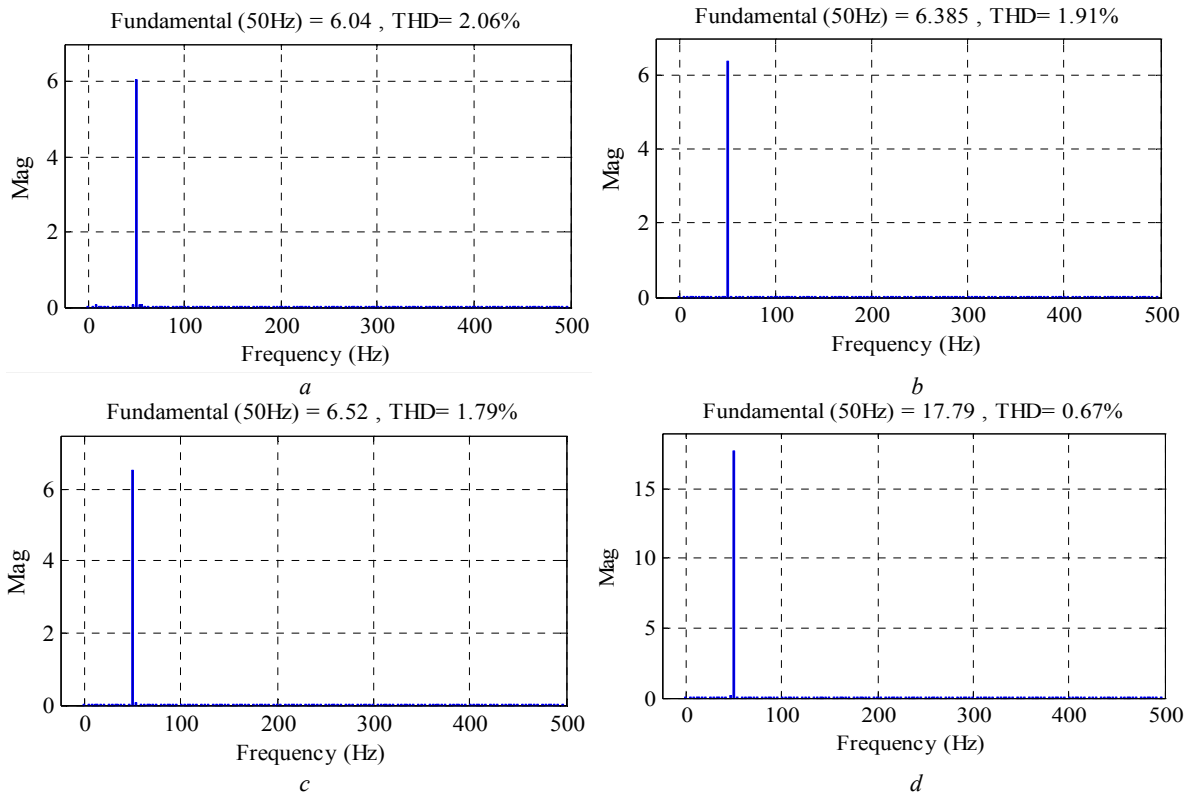
Fig. 10. Spectrum harmonic of one phase stator current for 1) supplied by conventional inverter: SMC (*a*), ASMC (*b*), AFSMC (*c*), 2) supplied by 19-level USAMI: AFSMC (*d*)

Sensitivity to the speed variation. The main object of this test is to analyze the influence of a speed variation of the DFIG on reactive and active powers for three controllers. For this objective and at time $t = 0.04$ s, the speed was varied from 150 rad/s to 170 rad/s as its shown in Fig. 11. Simulation results are shown in Fig. 12.
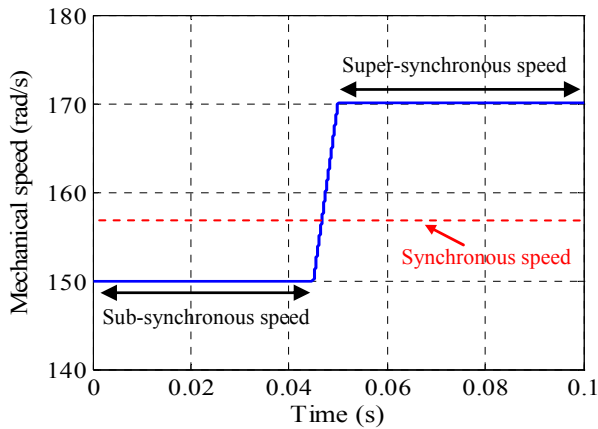
Fig. 11. Mechanical speed profile
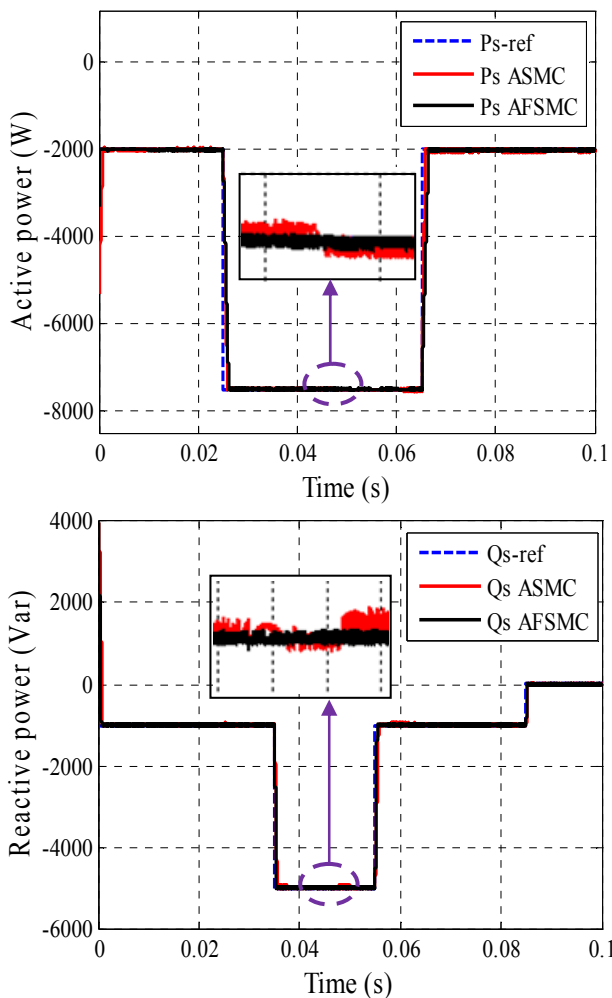
Fig. 12. Sensitivity to the speed variation

This figure express that the speed variation produces a slight effect on the powers curves of the system with ASMC controller, while effect is almost negligible for the system with AFSMC one. It can be noticed that this last has a nearly perfect speed disturbance rejection; indeed only very small power variation can be observed (fewer than 2 %). This result

is attractive for wind energy application quality and to ensure stability of the generated power when the sped is varying.

Robustness tests. The aim of these tests is to analyze the influence of the DFIG's parameters variation on the controllers' performance. The DFIG is running at its nominal speed. To test the robustness of the used controllers, parameters of the machine have been modified as follows: the values of the rotor and stator resistances are doubled while the values of inductances L_s, L_r and M are divided by 2. The obtained results are presented in Fig. 13. These results show that parameters variation of the DFIG presents a clear effect on the powers curves (especially in their errors curves) and that the effect appears more significant for ASMC controller than that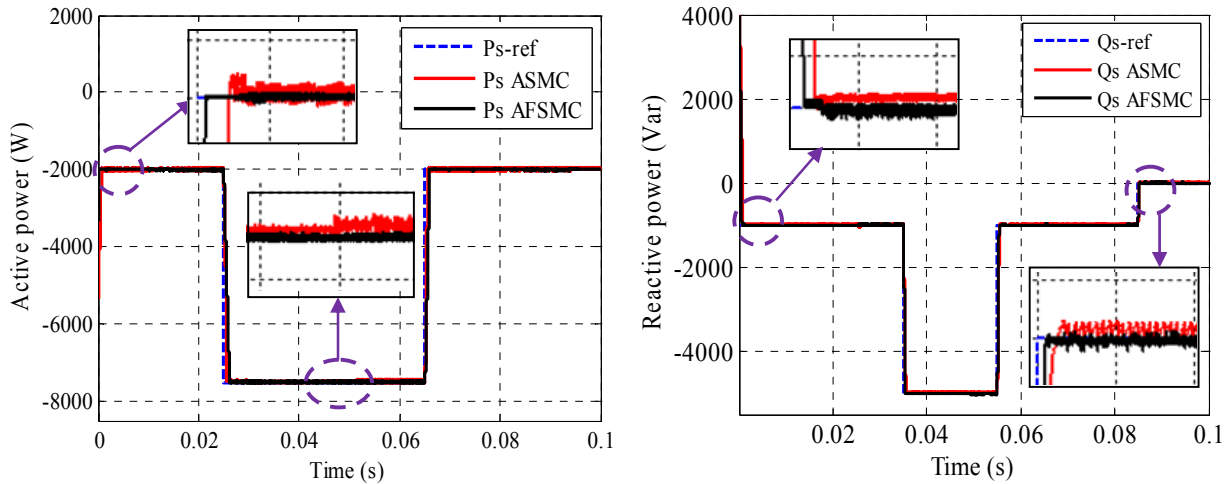 with AFSMC one. Thus it can be concluded that this last is the most robust among the proposed controllers studied in this work.
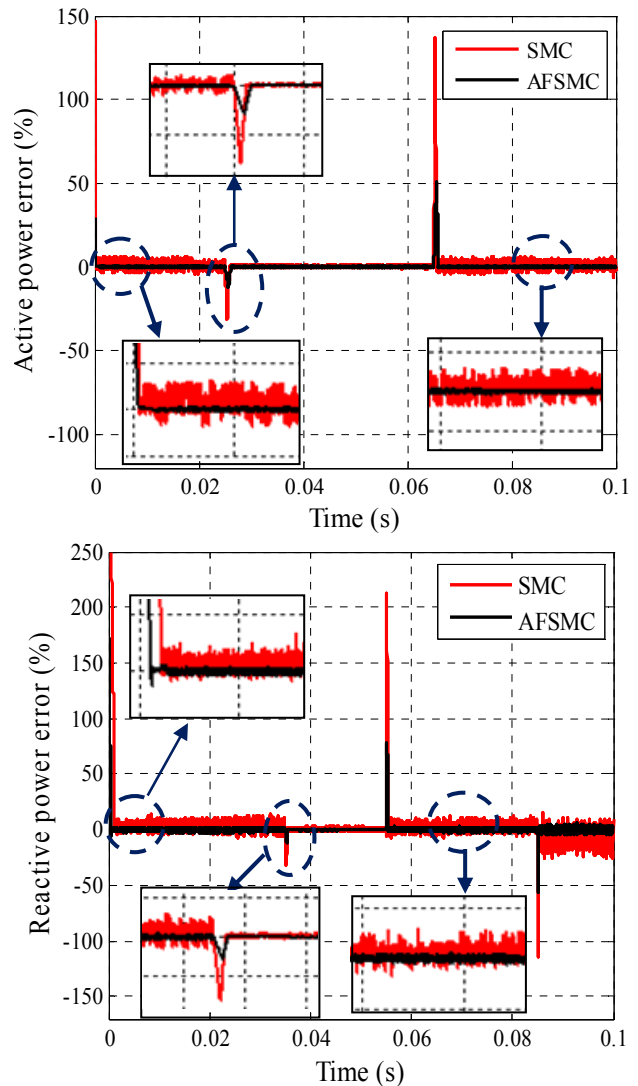
Fig. 13. Effect of machine's parameters variation on the robust control of the DFIG

Conclusion. The modeling and the control of a WT conversion system based on a DFIG connected directly to the grid by the stator side and fed by a 19-level inverter USAMI on the rotor side has been presented in this paper. This kind of variable speed systems has several advantages over the traditional WT operating

methods, such as an increase in the energy captured and the reduction of the mechanical stress. Our objective was the implementation of a robust decoupled control system of active and reactive powers generated by the stator side of the DFIG in order to make the system insensible with the external disturbances, parametric variations and to ensure a better execution of the DFIG. In the first step, we started with a study of modeling on the whole system. In second step, we present a vector control strategy in order to control active and reactive power exchanged between the stator the DFIG and the grid. In third step, three different controllers are synthesized and compared. In term of power reference tracking with the DFIG in ideal conditions, the SMC ensures a perfect decoupling between the two axes comparatively to the other controllers where the coupling effect between them is clear. The phenomenon of «chattering» associated with the control by sliding mode has a major drawback because it can excite the dynamics of high frequency control which makes it undesirable. In order to eliminate the chattering, we propose to use the AFSMC. Basing on all these results we conclude that robust control method as AFSMC can be a very attractive solution for devices using DFIG such as wind energy conversion systems and establish its suitability for the system drive.

Appendix A

Table 3

Machine parameters

| Parameters	Value	IS-Unit
Nominal power	7.5	kW
Turbine radius	35.5	m
Gearbox gain	90	
Stator voltage	398	V
Stator frequency	50	Hz
Number of pairs poles	2	
Nominal speed	150	rad/s
Rotor resistance	0.62	Ω
Stator inductance	0.084	H
Rotor inductance	0.081	H
Mutual inductance	0.078	H
Inertia	0.01	Kg·m^2

Appendix B

Table 4

List of symbols

Symbol	Significance
$V_{ds}, V_{qs}, V_{dr}, V_{qr}$	Two-phase stator and rotor voltages
$\psi_{qs}, \psi_{ds}, \psi_{qr}, \psi_{dr}$	Two-phase stator and rotor fluxes
$I_{ds}, I_{qs}, I_{dr}, I_{qr}$	Two-phase stator and rotor currents
R_s, R_r	Per phase stator and rotor resistances
L_s, L_r	Per phase stator and rotor inductances
M	Mutual inductance
p	Number of pole pairs
s	Laplace operator
ω_s, ω_r	Stator and rotor currents frequencies (rad/s)
ω	Mechanical rotor frequency (rad/s)
P_s, Q_s	Active and reactive stator power
J	Inertia
f	Coefficient of viscous frictions
C_r	Load torque
C_{em}	Electromagnetic torque

REFERENCES
1. Ellabban O., Abu-Rub H., Blaabjerg F. Renewable energy resources: Current status, future prospects and their enabling technology. *Renewable and Sustainable Energy Reviews*, 2014, vol.39, pp. 748-764. **doi: 10.1016/j.rser.2014.07.113**.
2. de Bessa I.V., Palhares R.M., D'Angelo M.F.S.V., Chaves Filho J.E. Data-driven fault detection and isolation scheme for a wind turbine benchmark. *Renewable Energy*, 2016, vol.87, pp. 634-645. **doi: 10.1016/j.renene.2015.10.061**.
3. *GWEC: Global Wind Energy Outlook 2014*. Available at: http://www.gwec.net/wp-content/uploads/2014/10/GWEO2014_WEB.pdf (accessed 02 May 2017).
4. *World Wind Energy Market Update, Navigant Research, 2015.* Available at: http://www.provedor.nuca.ie.ufrj.br/estudos/navigant1.pdf (accessed 15 October 2016).
5. Cardenas R., Pena R., Alepuz S., Asher G. Overview of Control Systems for the Operation of DFIGs in Wind Energy Applications, *IEEE Transactions on Industrial Electronics*, 2013, vol.60, no.7, pp. 2776-2798. **doi: 10.1109/tie.2013.2243372**.
6. Tazil M., Kumar V., Bansal R.C., Kong S., Dong Z.Y., Freitas W. Three-phase doubly fed induction generators: an overview. *IET Electric Power Applications*, 2010, vol.4, no.2, p. 75. **doi: 10.1049/iet-epa.2009.0071**.
7. Marques G.D., Sousa D.M. Air-Gap-Power-Vector-Based Sensorless Method for DFIG Control Without Flux Estimator. *IEEE Transactions on Industrial Electronics*, 2011, vol.58, no.10, pp. 4717-4726. **doi: 10.1109/tie.2011.2107716**.
8. Kamh M.Z., Iravani R. Three-Phase Steady-State Model of Type-3 Wind Generation Unit – Part I: Mathematical Models. *IEEE Transactions on Sustainable Energy*, 2011, vol.2, no.4, pp. 477-486. **doi: 10.1109/tste.2011.2156821**.
9. Jadhav H.T., Roy R. A comprehensive review on the grid integration of doubly fed induction generator. *International Journal of Electrical Power & Energy Systems*, 2013, vol.49, pp. 8-18. **doi: 10.1016/j.ijepes.2012.11.020**.
10. Boudjema Z., Taleb R., Yahdou A., Bouyekni A. Fuzzy second order sliding mode control of a doubly-fed induction machine supplied by two matrix converters. *Journal of Electrical Engineering,* 2015, vol.15, no.3, pp. 308-317.
11. Rahimi M. Drive train dynamics assessment and speed controller design in variable speed wind turbines. *Renewable Energy*, 2016, vol.89, pp. 716-729. **doi: 10.1016/j.renene.2015.12.040.**
12. Talha A., Berkouk El Madjid, Francois B., Boucherit M.S. Modeling and Control of a Power Electronic Cascade for the Multi DC Bus Supply of a Seven-Level NPC Voltage Source Inverter. *2006 12th International Power Electronics and Motion Control Conference*, Aug. 2006. **doi: 10.1109/epepemc.2006.4778399.**
13. Rodriguez J., Bernet S., Steimer P.K., Lizama I.E. A Survey on Neutral-Point-Clamped Inverters. *IEEE Transactions on Industrial Electronics*, 2010, vol.57, no.7, pp. 2219-2230. **doi: 10.1109/tie.2009.2032430.**
14. Huang Jing, Corzine K.A. Extended operation of flying capacitor multilevel inverters. *IEEE Transactions on Power Electronics*, 2006, vol.21, no.1, pp. 140-147. **doi: 10.1109/tpel.2005.861108.**
15. Babaei E. A Cascade Multilevel Converter Topology With Reduced Number of Switches. *IEEE Transactions on Power Electronics*, 2008, vol.23, no.6, pp. 2657-2664. **doi: 10.1109/tpel.2008.2005192.**
16. Kouro S., Malinowski M., Gopakumar K., Pou J., Franquelo L.G., Bin Wu, Rodriguez J., Pérez M.A., Leon J.I. Recent Advances and Industrial Applications of Multilevel Converters. *IEEE Transactions on Industrial Electronics*, 2010, vol.57, no.8, pp. 2553-2580. **doi: 10.1109/tie.2010.2049719**.

17. Tolbert L.M., Fang Zheng Peng, Habetler T.G. Multilevel converters for large electric drives. *IEEE Transactions on Industry Applications*, 1999, vol.35, no.1, pp. 36-44. **doi: 10.1109/28.740843**.

18. Rodriguez J., Franquelo L.G., Kouro S., Leon J.I., Portillo R.C., Prats M.A.M., Perez M.A. Multilevel Converters: An Enabling Technology for High-Power Applications. *Proceedings of the IEEE*, 2009 vol.97, no.11, pp. 1786-1817. **doi: 10.1109/jproc.2009.2030235**.

19. Song-Manguelle J., Mariethoz S., Veenstra M., Rufer A.A Generalized Design Principle of a Uniform Step Asymmetrical Multilevel Converter for High Power Conversion. *European Conference on Power Electronics and Applications, EPE'01*, Graz, Austria, August 2001.

20. López J., Sanchis P., Roboam X., Marroyo L. Dynamic Behavior of the Doubly Fed Induction Generator During Three-Phase Voltage Dips. *IEEE Transactions on Energy Conversion*, 2007, vol.22, no.3, pp. 709-717. **doi: 10.1109/tec.2006.878241**.

21. Boudjema Z., Taleb R., Yahdou A. A New DTC Scheme using Second Order Sliding Mode and Fuzzy Logic of a DFIG for Wind Turbine System. *International Journal of Advanced Computer Science and Applications*, 2016, vol.7, no.8. **doi: 10.14569/ijacsa.2016.070808**.

22. Li L.-B., Sun L.-L., Zhang S.-Z., Yang Q.-Q. Speed tracking and synchronization of multiple motors using ring coupling control and adaptive sliding mode control. *ISA Transactions*, 2015, vol.58, pp. 635-649. **doi: 10.1016/j.isatra.2015.07.010**.

23. Chen H., Ding K., Zhou X., Fu K., Qu Y. A novel adaptive sliding mode control of PWM rectifier under unbalanced grid voltage conditions based on direct power control. *Proceedings of the 33rd Chinese Control Conference*, Jul. 2014. **doi: 10.1109/chicc.2014.6896603**.

24. Sahoo S.R., Brisilla R.M., Sankaranarayanan V. Disturbance observer based adaptive sliding mode control: An application to single machine infinite bus power system. *2015 IEEE International Conference on Signal Processing, Informatics, Communication and Energy Systems (SPICES)*, Feb. 2015. **doi: 10.1109/spices.2015.7091544.**

25. Lee D., Vukovich G. Adaptive sliding mode control for spacecraft body-fixed hovering in the proximity of an asteroid. *Aerospace Science and Technology*, 2015, vol.46, pp. 471-483. **doi: 10.1016/j.ast.2015.09.001**.

26. Shahriari kahkeshi M., Sheikholeslam F., Zekri M. Design of adaptive fuzzy wavelet neural sliding mode controller for uncertain nonlinear systems. *ISA Transactions*, 2013, vol.52, no.3, pp. 342-350. **doi: 10.1016/j.isatra.2013.01.004.**

27. Do H.T., Park H.G., Ahn K.K. Application of an adaptive fuzzy sliding mode controller in velocity control of a secondary controlled hydrostatic transmission system. *Mechatronics*, 2014, vol.24, no.8, pp. 1157-1165. **doi: 10.1016/j.mechatronics.2014.09.003.**

28. Khazaee M., Markazi A.H.D., Omidi E. Adaptive fuzzy predictive sliding control of uncertain nonlinear systems with bound-known input delay. *ISA Transactions*, 2015, vol.59, pp. 314-324. **doi: 10.1016/j.isatra.2015.10.010**.

29. Mirzaei M., Nia F.S., Mohammadi H. Applying adaptive fuzzy sliding mode control to an underactuated system. *The 2nd International Conference on Control, Instrumentation and Automation*, Dec. 2011. **doi: 10.1109/icciautom.2011.6356736**.

30. Zou Y., Elbuluk M.E., Sozer Y. Stability Analysis of Maximum Power Point Tracking (MPPT) Method in Wind Power Systems. *IEEE Transactions on Industry Applications*, 2013, vol.49, no.3, pp. 1129-1136. **doi: 10.1109/tia.2013.2251854.**

31. Taleb R., Derrouazin A. USAMI Control with a Higher Order Harmonics Elimination Strategy based on the Resultant Theory. *International Conference on Technologies and Materials for Renewable Energy, Environment and Sustainability*, TMREES'14, Beirut, Lebanon, 10-13 April 2014.

32. Bouchafaa F. *Etude et commande de différentes cascades à onduler à neuf niveaux à structure NPC*. Application à la conduite d'une MSAP, Ph.D. thesis, ENP, Algiers, Algeria, 2008. (Fra).

33. Abdin E.S., Xu W. Control design and dynamic performance analysis of a wind turbine-induction generator unit. *IEEE Transactions on Energy Conversion*, 2000, vol.15, no.1, pp. 91-96. **doi: 10.1109/60.849122**.

34. Huang Y.-J., Kuo T.-C., Chang S.-H. Adaptive Sliding-Mode Control for Nonlinear Systems With Uncertain Parameters. *IEEE Transactions on Systems, Man, and Cybernetics, Part B (Cybernetics)*, 2008, vol.38, no.2, pp. 534-539. **doi: 10.1109/tsmcb.2007.910740**.

Mohamed Benkahla[1],
Rachid Taleb[1], *Associate Professor,*
Zinelaabidine Boudjema[1], *Associate Professor,*
[1] Electrical Engineering Department,
Hassiba Benbouali University, LGEER Laboratory,
Chlef, Algeria.
e-mail: med89.benkahla@gmail.com

Y.V. Kovalova

COMPUTER SIMULATION OF INTERMITTENT CURRENT MODE OF DC ELECTRIC DRIVE WITH THREE-PHASE CONTROLLED RECTIFIER

Introduction. The mode of intermittent current for DC motor with three-phase thyristor rectifier appears in the idle intervals of some mechanisms. Active and passive filters reduce the variable component of the rectified voltage. The capacitance of the capacitors filter is determined by the effective value of the variable component of the rectified voltage. Problem. Necessity of developing an analytical method for calculating the effective value of the variable component of the rectified voltage in the intermittent current mode, taking into account three parameters: the control angle, the electromagnetic time constant of the armature circuit and the load current. Purpose. To determine the dependence of the effective value of the variable component of the rectified voltage for three parameters in the intermittent current mode. Methodology. The effective value of the variable component of the rectified voltage is suggested to be determined through the voltage pulsations factor as the ratio of the effective value of the variable component of the rectified voltage to its constant component. The dependence of the pulsations factor from the parameters of the mode is determined using computer simulation of the mode for intermittent current. Results. The computer model is developed in the software package Simulink, which allows to change each parameter of the mode separately while stabilizing the other two. Numerical dependences of the pulsation factor on each parameter are obtained. The analytical dependence of the voltage pulsations factor on three influencing values was obtained by the method of experiment planning. Originality. For the first time, method has been developed for calculating pulsation factor of the rectified voltage and calculating the effective value of the variable component in the mode of intermittent currents, taking into account three parameters. Practical value. The proposed method will allow to rationally determine the capacity of the capacitors of active and passive filters and increase the efficiency of electromechanical power conversion by reducing the variable component of the rectified voltage. References 6, tables 7, figures 5.
Key words: **thyristor rectifier, voltage pulsations, angle of control, intermittent current.**

Режим прерывистого тока вентильных электроприводов постоянного тока появляется в интервалах холостого хода механизмов. Расчет емкости конденсаторов фильтра выполняется через действующее значение переменной составляющей выпрямленного напряжения и поэтому возникает задача разработки методики для ее расчета через коэффициент пульсаций напряжения с учетом угла управления, электромагнитной постоянной времени цепи якоря и тока нагрузки. Выражение для расчета коэффициента пульсаций напряжения с учетом влияющих факторов, полученное методом планирования эксперимента на основе компьютерного моделирования в программном пакете Simulink, позволяет определить емкость конденсаторов фильтра и повысить эффективность электромеханического преобразования электроэнергии за счет снижения переменной составляющей. Библ. 6, табл. 7, рис. 5.
Ключевые слова: **тиристорный выпрямитель, пульсации напряжения, угол управления, прерывистый ток.**

Actuality of the topic. In modern, controlled DC electric drives, semiconductor (transistor, thyristor) controlled rectifiers are widely used.

In the driven by the network thyristor rectifiers, which are now continuing to be serially produced in Ukraine, there are modes of intermittent currents during idle motor operation. Intermittent currents reduce the efficiency of the motor since the variable component of the current does not create a mechanical torque on the shaft.

To smooth out the rectified voltage, filters are used: active or resonant, which in their circuits have a capacitor [1-4]. For resonant filters, the capacity of a capacitor is determined by the condition of equality of reactor and capacitor energies

$$C = L \cdot \sum I_k^2 \Big/ \sum U_k^2 , \quad (1)$$

where L is the reactor inductance; I_k, U_k are the effective values of harmonic components of current and voltage, respectively.

From (1) the need to determine the effective value of the variable components of the rectified voltage including this for the mode of intermittent currents follows.

Analysis of publications. To determine the effective value of the variable components of the rectified voltage in the mode of intermittent currents it is necessary to choose a generalizing parameter that does not depend on

the motor power. This parameter is the voltage pulsation coefficient K_{pU} [1-4]

$$K_{pU} = \sqrt{\sum U_k^2} \Big/ U_{d0} = \sqrt{U_{dD}^2 - U_{d0}^2} \Big/ U_{d0} , \quad (2)$$

where U_{d0} is the average value (constant component) of rectified voltage, U_{dD} is the effective value of the rectified voltage.

Then the effective value of the alternating components of the rectified voltage is equal

$$\sqrt{\sum U_k^2} = K_{pU} \cdot U_{d0} . \quad (3)$$

In the well-known literature, for example, in [4], the graphoanalytic method for determining the voltage pulsation coefficient for DC motors is proposed only for the case of its operation with nominal load and nominal speed. But this method, on the one hand, is rather uncomfortable and cumbersome, and on the other hand, creates a certain error in the calculations, since, as a rule, DC motors operate with a load and a speed less than nominal. Proceeding from this, it is necessary to develop a more convenient and more precise method for determining the voltage pulsation coefficient for the mean values of load and speed, if during the process of operation the latter change in a certain range. The modern approach to determining the pulsation coefficient is a

method of computer modeling, but this method is not sufficiently studied in known literary sources.

The goal of the work is by means of computer simulation to determine the dependence of the pulsation coefficient of the output voltage of the three-phase controlled rectifier in the mode of intermittent currents on the angle of control and load parameters and to develop an analytical method for its calculation.

Results of investigations. The complex nature of the dependence of the voltage pulsation coefficient on the parameters of the mode excludes the possibility of obtaining it in an analytical form. Therefore, this dependence must be determined experimentally with further approximation by an analytic polynomial by the method of experiment planning. Since DC motors relate to a class of deterministic systems, it is rational to carry out a computer experiment. The computer model of a three-phase controlled rectifier (for example, a thyristor rectifier) with a DC motor in the software package Simulink [5] is presented in Fig. 1. The model consists of the following elements: three-phase voltage system performed on single-phase alternating voltage sources, three-phase thyristor rectifier with pulse-phase control system, ammeters, voltmeters, blocks for calculating the constant (average) components and effective values of voltage and current, display and oscilloscope. The constant component of the rectified voltage is determined by the block "Magnitude signal", and the effective value by the blocks "signal rms". The model of the DC motor is represented by the electromotive force (EMF) of the armature E_a, the active resistance R_a, and the inductance of the armature L_a. EMF of the armature is represented by a source of constant voltage.
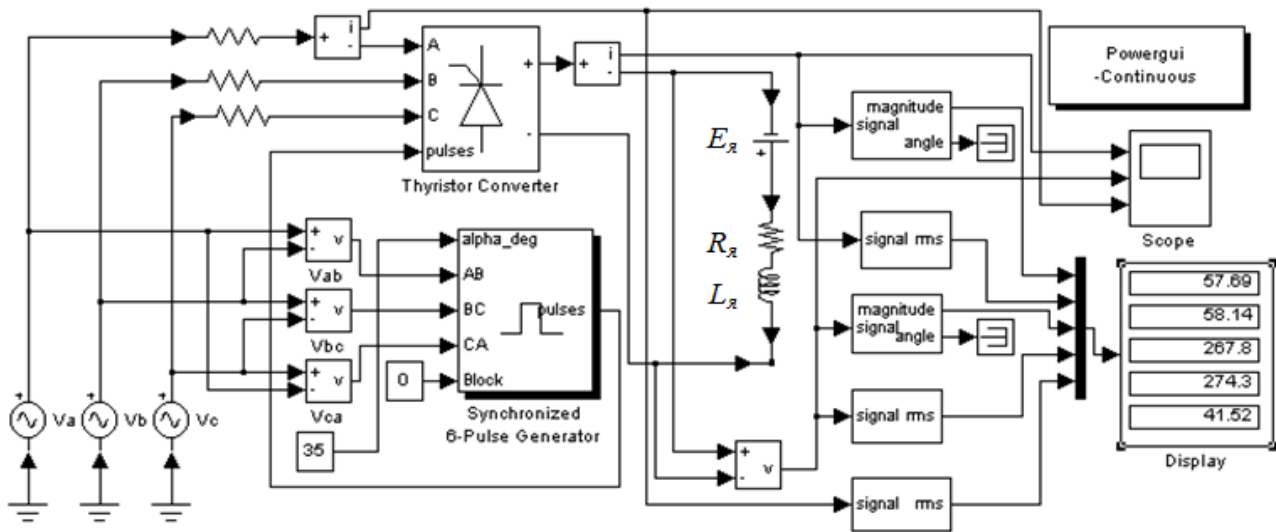
Fig. 1. Simulink-model of a DC electric drive with thyristor rectifier

The value of the armature EMF is given by the E_a block with the minus sign, since on the circuit it is connected non-opposite for rectifier voltage, due to the peculiarities of connection of blocks in the Simulink software package. Fig. 2 shows the obtained oscillograms of the voltage and current of the armature on the model.
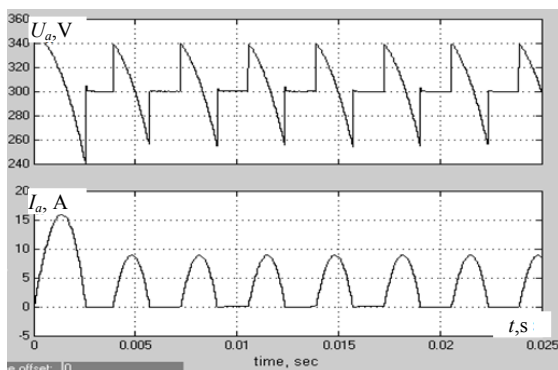
Fig. 2. Calculated oscillograms of voltage and current of the winding and armature

According to the method of planning the experiment, the computer experiment is carried out as follows. We determine the dependences of the voltage pulsation coefficient separately from each of the influencing factors (the angle of control of the thyristors, the electromagnetic time constant of the armature circuit and the load on the motor shaft) with stabilization of the other two. Stabilization of a constant current component is realized by adjusting the speed of the motor through the appropriate regulation of the armature EMF by the iteration method, that is, the successive approximation of the value of the EMF to the required value of current. Let's calculate the voltage pulsation coefficient in the mode of intermittent currents for the motor 4ПФ180M with parameters P = 45 kW, U = 440 V, n = 1060 rpm, I_{nom} = 115 A, R_a = 50 mΩ, L_a = 4 mH, T_a = 0.08 s. Experimental results are presented in Table 1-3.

Table 1

Calculation of the voltage pulsation coefficient dependence on the control angle at I_0 = const = 3.46 A, T_a = const = 0.08 s

α, degrees	80	110	140
U_{d0}, V	318.9	304.2	280.8
U_{dD}, V	319.7	305.4	282.3
$\sqrt{\sum U_k^2}$, V	22.6	27.05	29.06
K_{pU}	0.07	0.09	0.1

Calculation of the voltage pulsation coefficient dependence on the time constant at I_0 = const = 3.46 A, α = const = 110 degrees

T_a, s	0.06	0.08	0.1
U_{d0}, V	308.7	304.2	300.2
U_{dD}, V	309.4	305.3	301.6
$\sqrt{\sum U_k^2}$, V	20.8	25.89	29.03
K_{pU}	0.07	0.09	0.1

Calculation of the voltage pulsation coefficient dependence on the load at α = const = 110 degrees, T_a = const = 0.08 s

E_a, V	319.5	304	293.6
U_{d0}, V	319.6	304.2	293.9
U_{dD}, V	319.8	305.3	296
$\sqrt{\sum U_k^2}$, V	11.31	25.89	35.2
K_{pU}	0.04	0.08	0.12

According to the results of the research, the corresponding graphs of the dependences of the voltage pulsation coefficient from the angle of control, the electromagnetic time constant of the armature circuit and the load current, are built and shown in Fig. 3-5.
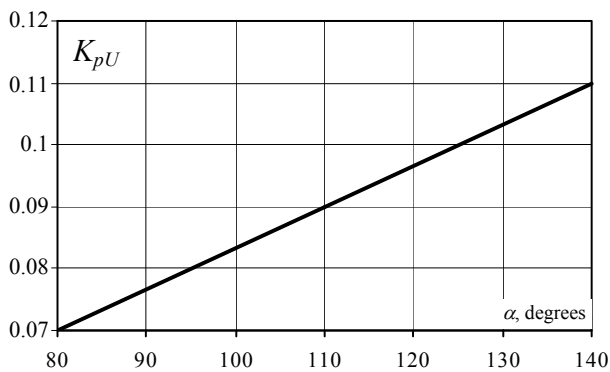
Fig. 3. Voltage pulsation coefficient dependence on the angle of control
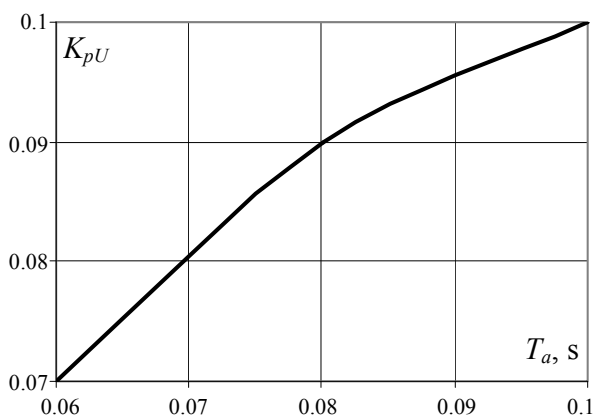
Fig. 4. Voltage pulsation coefficient dependence on the electromagnetic time constant of the armature circuit
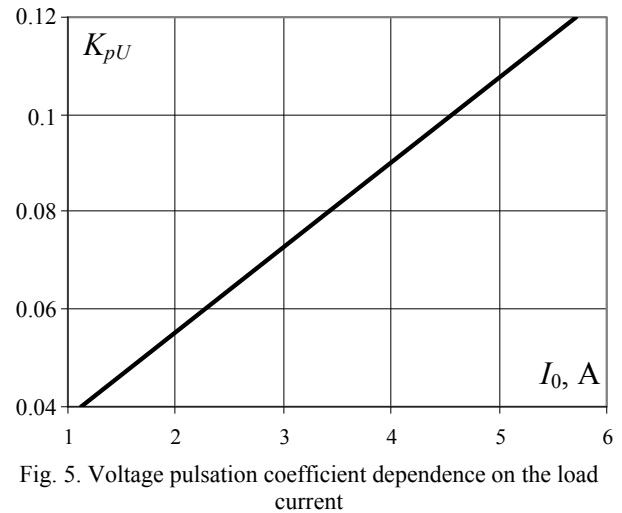
Fig. 5. Voltage pulsation coefficient dependence on the load current

For the approximation of the dependence of the voltage pulsation coefficient on the three influencing factors, we apply the experiment planning method. According to the methodology [6], we look for a polynomial for calculating the voltage pulsation coefficient in the form:

$$K_{pU} = b_0 + b_1\alpha + b_2 T_a + b_3 I_0^* + b_{12}\alpha T_a + \\ + b_{13}\alpha I_0^* + b_{23}T_a I_0^* + b_{123}\alpha T_a I_0^*, \qquad (4)$$

where $I_0^* = I_0/I_{nom}$ is the relative value of the constant current component.

The values of the factors in full experiment, their coding and variations are shown in Table 4.

The values of factors at the full factor experiment, their coding and variations

α, degrees	80	110	140
T, s	0.06	0.08	0.1
L, H	0.003	0.004	0.005
I_0^*	0.01	0.03	0.05
I, A	1.15	3.45	5.75
Code of factors	–	0	+

Experimental results are presented in Table 5.

Results of the full factor experiment

No.	E, V	U_{d0},V	U_{dD},V	$\sqrt{\sum U_k^2}$, V	K_{pU}
1	388	332.9	335	37.451	0.112
2	285	302.8	309.1	62.088	0.205
3	367	328.9	333.1	52.729	0.16
4	260	296.3	300.5	50.066	0.169
5	324.5	315.5	316.6	26.369	0.084
6	213	275.5	277.5	33.257	0.121
7	303.6	306.3	308.4	35.929	0.117
8	186.1	262.6	266.3	44.237	0.168
9	304.4	304.6	308.1	46.308	0.152

As a result of calculations of the coefficients of the polynomial (4), the formula of the pulsation coefficient is obtained

$$K_{pU} = 0.142 + 0.024\alpha + 0.012T_a - 0.02I_0^* -$$
$$- 0.009\alpha T_a - 0.002\alpha I_0^* + 0.009T_a I_0^* + 0.012\alpha T_a I_0^*. \qquad (5)$$

We determine the error of the calculated values of the voltage pulsation coefficient by the formula (5) relative to the obtained on the model. The results of calculations of errors are summarized in Table 6.

Table 6

Results of calculation of relative error

No. of experiment	Exact values	Calculated values	Relative error, %
1	0.112	0.16	−43
2	0.205	0.19	7
3	0.16	0.16	0
4	0.169	0.19	−12
5	0.084	0.16	−9
6	0.121	0.19	−57
7	0.117	0.16	−37
8	0.168	0.19	−13

To calculate the effective value of the voltage pulsations, we must determine the relative values of the average speed and the constant component of the armature voltage $\omega_a^* = U_0^* = \omega_a / \omega_{nom} = U_0 / U_{nom}^*$ which depend on the angle of control of the thyristors. Dependence of the relative value of the constant component of the armature voltage on the angle of control obtained on the model is shown in Table 7.

As a result of the approximation of the regulatory characteristic by the method of the least squares [6] according to Table 7 we obtain the formulas for the relative value of the constant component of the voltage and the control angle $U_{d0}^* = 0.831 - 0.077\alpha$, $\alpha = (0.831 - U_{d0}^*)/0.077$, where α is the angle of control in radians.

Table 7

Dependence of the relative value of the constant component of the armature voltage on the control angle

Thyristors control angle, degrees	Relative value of the armature voltage, U_{d0}^*
80	0.86
110	0.65
140	0.23

Thus, the method for determining the effective value of the components of the voltage components is as follows:

1. We set the speed ω_a^*, calculate U_{d0}^* and α;
2. We set the loading torque and determine the relative value of the constant current component $I_0^* = M_a / M_{nom}$;
3. We determine the voltage pulsation coefficient by the formula (5);
4. We determine the effective value of the variable voltage component by the formula (3).

Conclusions.

On the basis of computer simulation an analytical method for calculating the pulsation coefficient and the effective value of the variable component of the rectified voltage in the mode of intermittent currents is developed.

The proposed methodology will allow us to efficiently determine capacitances of filter capacitors and increase the efficiency of electromechanical transformation of electric energy by reducing the variable component of the rectified voltage.

REFERENCES

1. Afonso J., Couto C., Martins J. Active filters with control based on p-q theory. *IEEE Industrial Electronics Society Newsletter*, 2000, vol.47, no.3, pp. 5-10.
2. Soares V., Verdelho P., Marques G.D. An instantaneous active and reactive current component method for active filters. *IEEE Transactions on Power Electronics*, 2000, vol.15. no.4, pp. 660-669. **doi: 10.1109/63.849036.**
3. Kovalova Y.V. Determination of the ripple factor of the voltage of single-phase three sided rectifier. *Lighting engineering and power engineering*, 2016, no.3, pp. 4-7.
4. Sen'ko V.I. *Sylova elektronika* [Power electronics]. Kiev, IZMN Publ., 1999. 214 p. (Ukr)
5. German-Galkin S.G. *Komp'iuternoe modelirovanie poluprovodnikovykh sistem v MATLAB 6.0* [Computer model of the semiconductor systems in MATLAB 6.0]. Saint Petersburg, CORONA Publ., 2007. 320 p. (Rus).
6. Vlasov K.P. *Metody issledovanii i organizatsiia eksperimentov* [The method of investigation and organization experiments]. Kharkiv, Gumanitarnyi Center Publ., 2002. 256 p. (Rus).

Y.V. Kovalova, Candidate of Technical Sciences,
O.M. Beketov National University of Urban Economy in Kharkiv,
17, Marshal Bazhanov Str., Kharkiv, 61002, Ukraine,
phone +380 66 9797302, e-mail: kovalova.jv@gmail.com

V.V. Panchenko, A.S. Maslii, D.P. Pomazan, S.G. Buriakovskyi

DETERMINATION OF PULSATION FACTORS OF THE SYSTEM OF SUPPRESSION OF INTERFERING HARMONICS OF A SEMICONDUCTOR CONVERTER

Purpose. The purpose of the paper is to define the pulsation factors of a closed-loop automatic control system (ACS) of interfering harmonics containing a semiconductor converter with double-sided pulse-width modulation (PWM), as well as confirmation of theoretical assumptions about possibilities of self-compensation of pulsation factors' influence in the system with double-sided PWM. Methodology. The research was conducted with the usage of classic electric circuit theory, frequency analysis methods, generalized function theory. Results. The obtained expressions mathematically relate pulsation factors, value of the damping coefficient and manipulative variable for different frequencies of interfering harmonics in the system with double-sided PWM. The research concerned harmonics with frequencies 100, 300, 600, 900 and 1200 Hz as the most significant constituents of the output voltage of a 12-pulse semiconductor converter. The obtained expressions allow taking into account settings of the selective link and its approximation on the level of supreme frequencies with aperiodic link. Originality. The research has experimentally proved theoretical assumptions about self-compensation of pulsation factors in the system with double-sided PWM. It has been shown that the damping coefficient has a low-impact influence on the values of pulsation factors. It is caused by the pass band of the selective link, which is included in the closed-loop control system of harmonics regulation. Practical value. Application of the research results can contribute to the development of the closed-loop control system for effective attenuation of interfering harmonics in direct current contact wire without interfering in the power part of the semiconductor converter. Besides the possibility to regulate output voltage, it will also help to solve the problem of electromagnetic compatibility of a traction substation semiconductor converter with contact wire. The application of the developed closed-loop control system will as well provide for decreasing the size of the filter in the direct current traction substation unit. References 9, figures 5.
Key words: **pulsation factor, interfering harmonic, automatic control system, double-sided pulse-width modulation, semiconductor converter.**

Цель. Целью статьи является определение факторов пульсаций замкнутой системы автоматического регулирования (САР) мешающих гармоник, содержащей полупроводниковый преобразователь с двухсторонней широтно-импульсной модуляцией (ШИМ), а также подтверждение теоретических предпосылок о возможности самокомпенсации действия факторов пульсаций в системе с двухсторонней ШИМ. Методика. Для проведения работы использовались: классическая теория электрических цепей, методы гармонического анализа и теория обобщенных функций. Результаты. Получены выражения, математически связывающие факторы пульсаций, значения коэффициентов демпфирования и регулируемого параметра для разных частот мешающих гармоник в системе с двухсторонней ШИМ. Научная новизна. Экспериментально подтверждены теоретические предпосылки о самокомпенсации действия факторов пульсаций в системе с двухсторонней ШИМ; Практическое значение. Использование результатов работы позволит создать замкнутую САР для эффективного подавления мешающих гармоник в контактной сети постоянного тока. Библ. 9, рис. 5.
Ключевые слова: **фактор пульсаций, мешающая гармоника, система автоматического регулирования, двухсторонняя широтно-импульсная модуляция, полупроводниковый преобразователь.**

Problem definition. The main disadvantages of semiconductor converters with increased pulsation are:

• impossibility to create a converter with absolutely symmetrical shoulders, which leads to generation of harmonics, reduction of the quality of electric energy at the output of the traction substation and deterioration of the electromagnetic compatibility of the rectifier with the traction network. The problems of symmetrization of semiconductor converters remain unsolved in [1, 2];

• constant presence of non-canonical harmonics in output voltage, to which signaling, centralization and blocking (SCB) devices are critical and which do not depend on rectifier pulsation, due to the practical impossibility of creating an integer ratio of turns of high power transformer windings supplying rectifier bridges. At the same time, in [3, 4], the possibility of applying active filtering of harmonics of the output voltage of a semiconductor converter is not considered.

In addition, the cause of the disturbing harmonics is the discrete nature of the rectification conversion of the electric energy of the alternating current and the effect of the inherent asymmetry of the rectifier and the asymmetry of the supply network. These reasons cause the generation into the contact network of canonical and non-canonical harmonics. A large contribution to the formation of an interfering voltage is made by harmonics whose frequencies lie in the range $f_m = 100...1200$ Hz. The use to reduce the amount of interfering harmonics in the specified range in the composition of the smoothing filter of rejection LC circuits is not effective enough [5, 6]. This is explained by the difficulty of obtaining precise tuning of the rejection circuits at the frequencies of the interfering harmonics and changing the resonant frequencies caused by the temperature and time effects.

That is, it is actual to search for alternative technical solutions for combating the interfering harmonics of a semiconductor converter.

In [7] the questions of application of special closed structures for regulating the harmonics of the output voltage of the controlled converter were considered. However, the proposed systems with single-sided PWM

have a narrow bandwidth and do not allow high PWM frequencies to be realized.

Thus, in the context of the problem under consideration, the issues of using a semiconductor converter with a two-way PWM, as part of a closed automatic control system, remain unresolved to reduce the values of interfering harmonics and improve electromagnetic compatibility with the traction network.

The goal of the work is investigation of electromagnetic processes in the automatic control system of interfering harmonics of a semiconductor converter with a two-way PWM and obtaining expressions for determining the factors of pulsations acting in this system.

Main part. In the automatic control system containing a converter with two-way pulse width modulation (Fig. 1), two pulsation factors act [9].
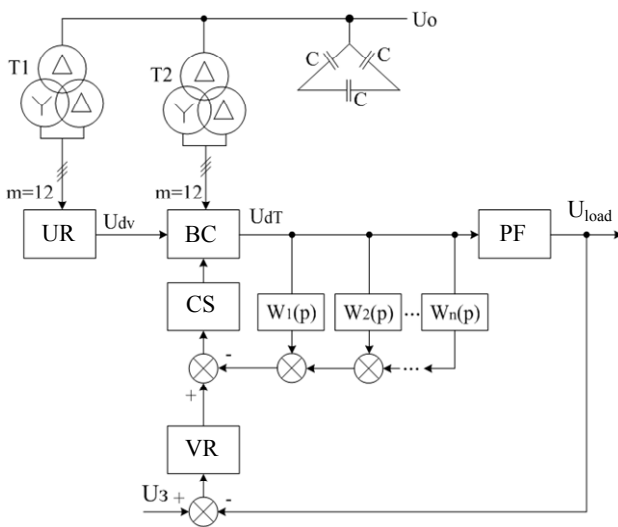

Fig. 1. Closed automatic control system of the semiconductor converter with two-way PWM

In the automatic control system under consideration, the main power flow from the mains to the load is transmitted through the main 12-pulse uncontrolled rectifier (UR). The wide-adjustable booster converter (BC) controlled by the control system (CS) is designed to transmit power, which is about 20 % of the power of the main rectifier.

Stabilization of the voltage of the rectifier unit is ensured by negative feedback on the load voltage U_{load} with the help of the voltage regulator (VR), and the regulation of the interfering harmonics of load voltage over a wide frequency range is performed by internal circuits containing selective links $W_1(p)$, $W_2(p)$ … $W_n(p)$ with transfer functions.

The proposed automatic control system of the rectifier with a pulse-width-adjustable BC meets the requirements of astaticism. This requirement is achieved by the introduction of an integral part in the VR, as well as the use of adaptive feedback on the circuit suppression factor of the load voltage harmonics.

The main task of the L-shaped passive the *LC*-filter (PF) in this system is the suppression of the harmonic of the voltage of the BC carrier frequency.

The use of a two-sided PWM instead of a one-sided PWM is due to the possibility of extending the converter bandwidth, which will suppress the harmonics of the output voltage of a DC traction substation over a wide frequency range, and therefore reduce the volume of the PF.

In the booster converter, the formation of a pulse-width modulated pulse train is performed by a control system, the functional circuit of which is shown in Fig. 2. Functionally, the control system consists of a reference voltage generator RVG and a comparator K.
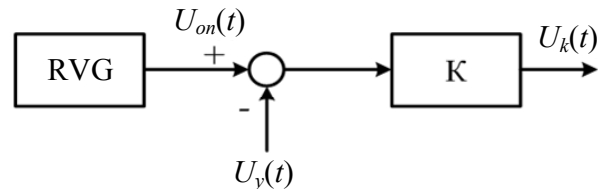
Fig. 2. Functional circuit of the control system

In [8] generalized expressions for the pulsation factors were obtained in the representation of the transfer function of the reduced continuous part as a sum of aperiodic links. For the system for suppressing the interfering harmonic, the expressions for the pulsation factors have the form

$$F_1^{-1} = 1 - \sum_{i=1}^{n} \frac{K_P T_1}{2T_i} \cdot \frac{(1 - e^{-\gamma \frac{T_1}{T_i}}) e^{-\frac{T_1}{T_i}}}{1 - e^{\frac{T_1}{T_i}}}, \quad (1)$$

$$F_2^{-1} = 1 + \sum_{i=1}^{n} \frac{K_P T_1}{2T_i} \cdot \frac{(1 - e^{-\gamma \frac{T_1}{T_i}}) e^{-\frac{T_1}{T_i}}}{1 - e^{-\frac{T_1}{T_i}}}. \quad (2)$$

To apply formulas (1), (2), we represent the transfer function of the selective link $G(p)$ as a sum of aperiodic links

$$G(p) = \frac{p}{T_0} \left(\frac{K_1}{p - p_1} + \frac{K_2}{p - p_2} \right), \quad (3)$$

where $p_1 = (-\xi + ja)/T_0$, $p_2 = (-\xi - ja)/T_0$ are the poles of the transfer function $G(p)$.

The coefficients K_1 and K_2 are defined as the residues of the transfer function $G(p)$ in the corresponding poles

$$K_1 = \left| \frac{p}{p - p_2} \right|_{p = p_1} = \frac{a + j\xi}{2a}, \quad (4)$$

$$K_2 = \left| \frac{p}{p - p_2} \right|_{p = p_2} = \frac{a - j\xi}{2a}. \quad (5)$$

Substituting (4) and (5) into (3) and transforming, we obtain

$$G(p) = \frac{j}{2a} \left[\frac{1}{T_0(\xi + ja) + 1} - \frac{1}{T_0(\xi - ja) + 1} \right]. \quad (6)$$

Taking into account (6), the expressions for the pulsation factors take the form

$$F_1^{-1} = 1 - j\frac{K_p T_1}{4aT_0}\left\{(\xi - ja)\frac{[1 - e^{-\gamma(\xi - ja)\frac{T_1}{T_0}}]e^{-(\xi - ja)\frac{T_1}{T_0}}}{1 - e^{-(\xi - ja)\frac{T_1}{T_0}}} - (\xi + ja)\frac{[1 - e^{-\gamma(\xi + ja)\frac{T_1}{T_0}}]e^{-(\xi + ja)\frac{T_1}{T_0}}}{1 - e^{-(\xi + ja)\frac{T_1}{T_0}}}\right\}, \quad (7)$$

$$F_2^{-1} = 1 + j\frac{K_p T_1}{4aT_0}\left\{(\xi - ja)\frac{[1 - e^{-\gamma(\xi - ja)\frac{T_1}{T_0}}]e^{-(\xi - ja)\frac{T_1}{T_0}}}{1 - e^{-(\xi - ja)\frac{T_1}{T_0}}} - (\xi + ja)\frac{[1 - e^{-\gamma(\xi + ja)\frac{T_1}{T_0}}]e^{-(\xi + ja)\frac{T_1}{T_0}}}{1 - e^{-(\xi + ja)\frac{T_1}{T_0}}}\right\}. \quad (8)$$

Performing simple but rather cumbersome transformations in (7) and (8), we obtain expressions for the pulsation factors of the closed system for suppressing the interfering harmonics

$$F_1^{-1} = 1 + j\frac{K_p T_1}{2aT_0}\left\{\frac{C_{1.1} \cdot e^{-\xi\frac{T_1}{T_0}} - C_{1.2} \cdot e^{-\xi(1-\gamma)\frac{T_1}{T_0}} -}{1 - 2e^{-\xi\frac{T_1}{T_0}}\cos a\frac{T_1}{T_0} + e^{-2\xi\frac{T_1}{T_0}}} \frac{- C_{1.3} \cdot e^{-\xi(2-\gamma)\frac{T_1}{T_0}} + a \cdot e^{-2\xi\frac{T_1}{T_0}}}{}\right\}, \quad (9)$$

where

$$C_{1.1} = \xi \sin a\frac{T_1}{T_0} - a\cos a\frac{T_1}{T_0};$$

$$C_{1.2} = \xi \sin a(1-\gamma)\frac{T_1}{T_0} - a\cos a(1-\gamma)\frac{T_1}{T_0};$$

$$C_{1.3} = \xi \sin a\gamma\frac{T_1}{T_0} - a\cos a\gamma\frac{T_1}{T_0};$$

$$F_2^{-1} = 1 - j\frac{K_p T_1}{2aT_0}\left\{\frac{C_{2.1} \cdot e^{-\xi\gamma\frac{T_1}{T_0}} - C_{2.2} \cdot e^{-\xi\frac{T_1}{T_0}} +}{1 - 2e^{-\xi\frac{T_1}{T_0}}\cos a\frac{T_1}{T_0} + e^{-2\xi\frac{T_1}{T_0}}} \frac{+ C_{2.3} \cdot e^{-\xi(1+\gamma)\frac{T_1}{T_0}} - a \cdot e^{-2\xi\frac{T_1}{T_0}}}{}\right\}, \quad (10)$$

where

$$C_{2.1} = \xi \sin a\gamma\frac{T_1}{T_0} - a\cos a\gamma\frac{T_1}{T_0};$$

$$C_{2.2} = \xi \sin a\gamma\frac{T_1}{T_0} - a\cos a\frac{T_1}{T_0};$$

$$C_{2.3} = \xi \sin a(1-\gamma)\frac{T_1}{T_0} + a\cos a(1-\gamma)\frac{T_1}{T_0}.$$

Fig. 3, 4 show the results of calculating the pulsation factors for different values of the controlled parameter γ,

the damping coefficient ξ, and the frequencies of the interfering harmonics.

From the obtained dependences it follows that in contrast to a system with one-sided pulse-width modulation in a system with two-way pulse-width modulation, the effect of self-compensation of the action of pulsation factors is observed. There is a weak dependence of the pulsation factors on the damping coefficient. This is explained by the fact that the frequencies influencing the values of the pulsation factors lie outside the pass band of the selective link.
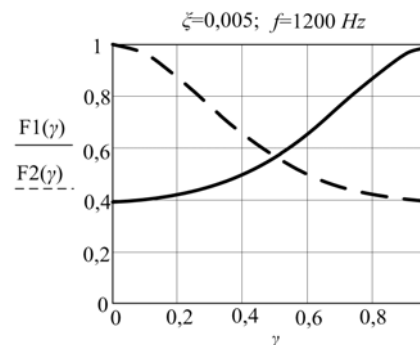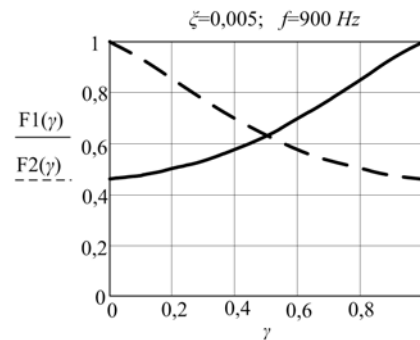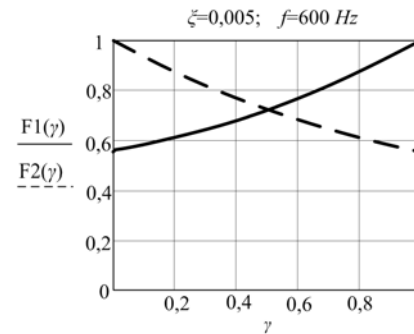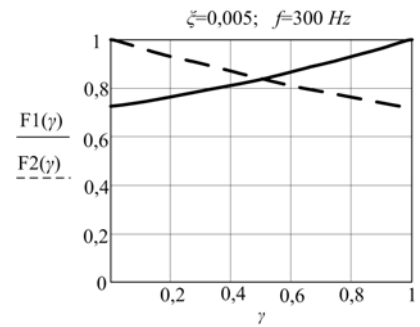

Fig. 3. The results of calculating the pulsation factors for different values of the frequency of the interfering harmonic f
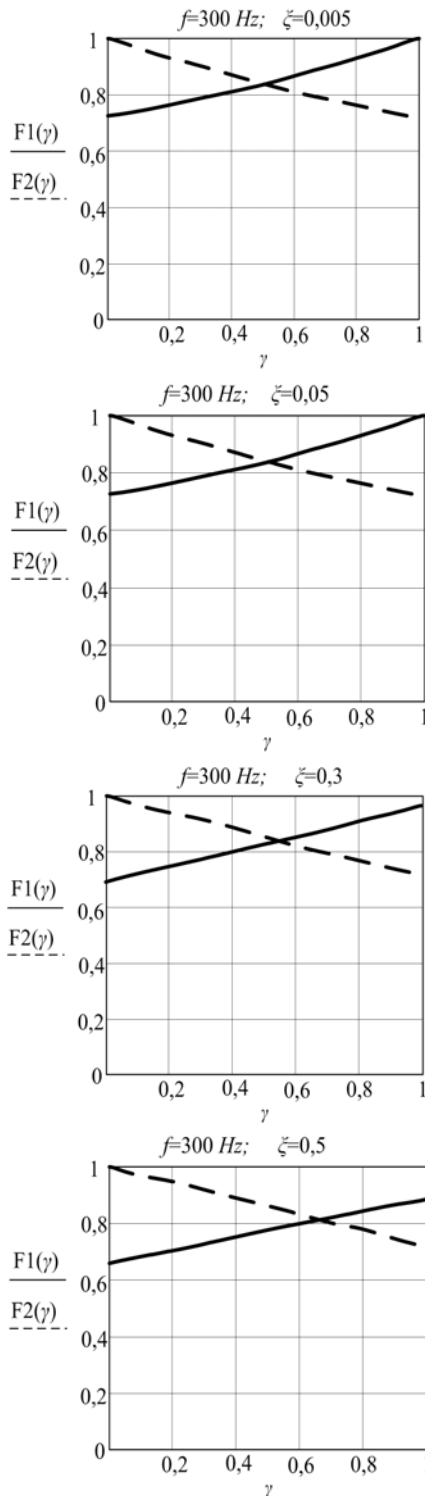
Fig. 4. The results of calculating the pulsation factors for different values of the damping coefficient ξ

The amplitude-frequency response of the selective link $G(p)$ in the region of higher frequencies has a slope of -20 dB/dec. This gives a prerequisite for the approximation of the link $G(p)$ by an aperiodic link

$$H(p) = \frac{1}{T_e p + 1},\qquad(11)$$

having the same transmission factor as $G(p)$ at the pulse-width modulation frequency.

The time constant of an aperiodic link is defined as

$$T_e^2 = \frac{1 + \dfrac{f_{PWM}^2}{f_q^2}\left[\dfrac{f_{PWM}^2}{f_q^2} - 2(1 - 2\xi^2) - 1\right]}{4\pi^2 \dfrac{f_{PWM}^4}{f_q^2}},\qquad(12)$$

where f_{PWM} is the pulse-width modulation frequency; f_q is the frequency of the q-th interfering harmonic.

In this case, the expressions for the pulsation factors take the form [6]:

$$F_1^{-1} = 1 - \frac{K_p T_1}{2 T_e} \cdot \frac{(1 - e^{-\gamma \frac{T_1}{T_e}}) e^{-\frac{T_1}{T_e}}}{1 - e^{-\frac{T_1}{T_e}}};\qquad(13)$$

$$F_2^{-1} = 1 + \frac{K_p T_1}{2 T_e} \cdot \frac{e^{-\gamma \frac{T_1}{T_e}} - e^{-\frac{T_1}{T_e}}}{1 - e^{-\frac{T_1}{T_e}}}.\qquad(14)$$

Fig. 5 shows the graphical dependencies characterizing the changes in the pulsation factor in the function of the regulated parameter γ, calculated from formulas (13) and (14).
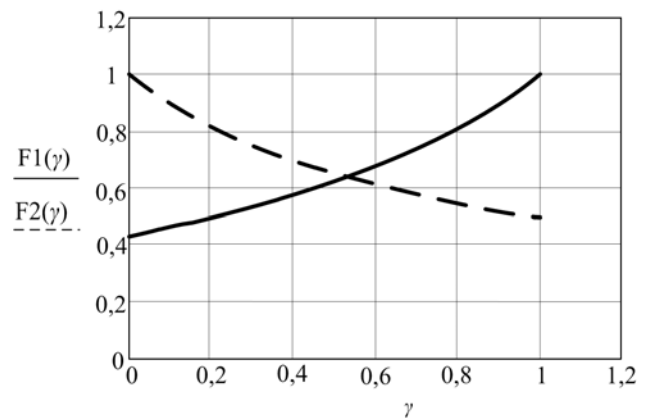
Fig. 5. Dependences of values of pulsation factors on γ

Conclusions.

For the first time, expressions were obtained for determining the pulsation factors of the automatic control system of interfering harmonics of a semiconductor converter with a two-way PWM for different values of the damping coefficient and the controlled parameter.

It is established that in the considered automatic control system of a semiconductor converter with two-way PWM, self-compensation of the action of pulsation factors occurs.

As a result of the investigation of electromagnetic processes in the automatic control system of a semiconductor converter, the possibility of suppressing interfering harmonics without interference in its power part was revealed. This is especially important in the maintenance of the rectifying installation of the traction substation.

REFERENCES
1. Richter J., Doppelbauer M. Control and mitigation of current harmonics in inverter-fed permanent magnet synchronous machines with non-linear magnetics. *IET Power*

Electronics, 2016, vol.9, no.10, pp. 2019-2026. **doi: 10.1049/iet-pel.2015.0977.**

2. Ghanizadeh R., Ebadian M., Gharehpetian G.B. Non-linear load sharing and voltage harmonics compensation in islanded microgrids with converter interfaced units. *International Transactions on Electrical Energy Systems*, 2016, vol.27, no.1, p. e2237. **doi: 10.1002/etep.2237**.

3. Panchenko V.V. The harmonic composition of the output voltage of a rectifier unit with a PWM voltage booster converter. *Information and control systems at railway transport*, 2015, no.4, pp. 71-78. (Rus).

4. Kuznetsov B.I., Nikitina T.B., Tatarchenko M.O., Khomenko V.V. Multicriterion anisotropic regulators synthesis by multimass electromechanical systems. *Technical electrodynamics*, 2014, no.4, pp. 105-107. (Rus).

5. Sozański K. Three phase active power filter with selective harmonics elimination. *Archives of Electrical Engineering*, 2016, vol.65, no.1, pp. 33-44. **doi: 10.1515/aee-2016-0003**.

6. Huang J., Shi H. Suppression of the Peak Harmonics from Loads by Using a Variable Capacitance Filter in Low-Voltage DC/DC Converters. *IEEE Transactions on Electromagnetic Compatibility*, 2016, vol.58, no.4, pp. 1217-1227. **doi: 10.1109/temc.2016.2552230**.

7. Coillot C., Nativel E., Zanca M., Goze-Bac C. The magnetic field homogeneity of coils by means of the space harmonics suppression of the current density distribution. *Journal of Sensors and Sensor Systems*, 2016, vol.5, no.2, pp. 401-408. **doi: 10.5194/jsss-5-401-2016**.

8. Scherbak Y.V., Ivakina K.Y., Panchenko V.V. Factor pulsations automatic regulation with two-way pulse width modulation. *Collected scientific works of Ukrainian State University of Railway Transport*, 2015, no.153, pp. 113-120. (Rus). **doi: 10.18664/1994-7852.153.2015.64336.**

9. Panchenko V.V. Dynamic properties of system «rectifier with buck converter – load». *Eastern-European Journal of Enterprise Technologies*, 2013, vol.4, no.8(64), pp. 14-17. (Ukr).

V.V. Panchenko[1]*, Candidate of Technical Science, Associate Professor,*
A.S. Maslii[1]*, Candidate of Technical Science, Associate Professor,*
D.P. Pomazan[1]*, Postgraduate Student,*
S.G. Buriakovskyi[2]*, Doctor of Technical Science,*
[1] Ukrainian State University of Railway Transport,
7, Feierbakh Square, Kharkiv, 61050, Ukraine,
e-mail: vlad_panchenko@ukr.net, a.masliy@ukr.net,
danil.pomazan@ukr.net
[2] Scientific-&-Research Planning-&-Design Institute «Molniya»,
National Technical University «Kharkiv Polytechnic Institute»,
2, Kyrpychova Str., Kharkiv, 61002, Ukraine,
e-mail: sergbyr@i.ua

O.D. Podoltsev, V.M. Zolotaryov, M.A. Shcherba, R.V. Belyanin

CALCULATION OF THE EQUIVALENT ELECTRICAL PARAMETERS OF THE INDUCTOR OF INDUCTION CHANNEL FURNACE WITH DEFECTS IN ITS LINING

Aim. The aim of the paper is to determine a quantitative relationship between measured impedance of the inductor and the electrical characteristics of the separated melt circuit parts for the determination of the place of a liquid metal leakage and for the improvement in such way the diagnostic system of lining state of induction channel furnaces. Technique. The study was performed on the basis of the concepts of theoretical electrical engineering, mathematical physics, and mathematical modeling. Results. Using two equivalent electrical circuits of the inductor the analytical expressions and graphical dependencies, which determine a quantitative relationship between the parameters of the separated parts of a liquid-metal circuit and the impedance of the whole inductor measured in practice, for the presence of different lining defects, were found. The method for calculating the increments of equivalent electrical parameters of the inductor as a function of increments of the parameters of the secondary liquid-metal circuit was proposed. Scientific novelty. It is proved that for small changes (less than 10 %) of the parameters of the liquid-metal circuit, it is expedient to use a linear relationship between its increments and to create the sensitivity matrix, which clearly shows the presence of a strong or weak interrelation between the disturbed values of the parameters of the secondary circuit and the inductor. Practical significance. The use of this technique allows to develop the database for various types of lining defects for a given furnace and on its basis to predict the places of a melt leakage and the state of furnace lining owing to periodical measurements of the inductor parameters. References 10, figures 3.
Key words: **equivalent electric parameters, mathematical modeling, induction channel furnace, defects of lining, diagnostics of the lining state.**

Цель. Целью статьи является установление количественной связи между измеряемым импедансом индуктора и электрическими характеристиками отдельных участков контура расплава для установления места протекания жидкого металла и усовершенствования таким образом системы диагностики состояния футеровки индукционных канальных печей. Методика. Для проведения исследований использовались положения теоретической электротехники, математической физики, математического моделирования. Результаты. С использованием двух электрических схем замещения индуктора получены аналитические выражения и графические зависимости, устанавливающие количественную связь между параметрами отдельных участков жидкометаллического контура и измеряемым на практике импедансом всего индуктора при наличии различных дефектов в его футеровке. Предложена методика расчета приращений эквивалентных электрических параметров индуктора в зависимости от приращений параметров вторичного жидкометаллического контура. Научная новизна. Доказано, что при малых изменениях (менее 10%) параметров жидкометаллического контура целесообразно использовать линейную связь между их приращениями с построением матрицы чувствительности, которая наглядно показывает наличие сильной или слабой связи между возмущенными значениями параметров вторичного контура и индуктора. Практическое значение. Использование данной методики позволяет разработать базу данных для различных типов дефектов футеровки для индукционной канальной печи и на ее основе, путем периодического измерения параметров индуктора, прогнозировать места протеканий расплава и состояние футеровки. Библ. 10, рис. 3.
Ключевые слова: **эквивалентные электрические параметры, математическое моделирование, индукционная канальная печь, дефекты футеровки, диагностика состояния футеровки.**

Introduction. Today consumers of metallurgical products make high demands on the quality of copper rolled wire (homogeneity, chemical purity, etc.). The copper rolled wire manufactured in induction channel furnaces generally satisfies the highest requirements [1]. On the strength of this circumstance, it is induction installations of this type that are used in the cable industry in the manufacture of copper rolled wire for the production of power cable cores [2].

The peculiarity of the induction furnaces, in particular channel type is the lining destruction under various factors: 1) the high temperature of the molten metal; 2) intensive hydrodynamic molten metal flow destroying the internal walls of the lining, forming caverns and leading to a decrease in thickness of the walls during prolonged operation, and 3) the presence of an electromagnetic field that causes vibrational phenomena in the liquid metal and in the outer metal casing.

Modern researches are aimed at increasing the efficiency and operating life of induction furnaces. In particular, they are aimed at analyzing the distribution of temperature fields inside the refractory lining under different operating conditions [4, 5], determination of mixing features of the metal melt [6], improving the diagnostic systems and continuous monitoring of the furnace lining state in industrial use [8, 9] and improvement of structural elements of furnaces and inductors [3, 7].

In particular, the improvement of the systems for diagnosing the state of furnace lining is an important scientific problem, since it allows to more accurately predict the residual life of the equipment, adjust its operating modes to extend the service life and prepare in advance for the necessary replacement of the lining, as it

is related with complete stoppage of the furnace and draining the metal melt.

In order to diagnose the state of the lining of a channel induction furnace, the following three methods can potentially be used in practice:

1) Periodic measurement of the complex equivalent resistance (pure resistance and image impedance) of the inductor, the value of which depends on the state of the lining (the presence of pits and caverns, thickening of the channel and narrowing of the channel filled with liquid metal, etc.) [10].

2) Regular measurement of the temperature distribution over the surface of the furnace outer casing by means of pyrometer, for example, or an infrared imager. This distribution allows to identify the «hot spots» on this surface, which are due to the appearance of caverns or pits filled with liquid metal in the lining. [5, 9].

3) Evaluation of the dielectric properties of the lining by measuring the capacitance between the outer furnace casing and the liquid metal, which are separated by a dielectric lining, as well as measuring the dielectric loss tangent of this capacity, generally at a different frequency of the external supplementary source. An analysis of the dependences obtained in this way allows to conclude that there are defects in the furnace lining [1].

At present, the systems for diagnosing the state of induction channel furnaces, offered by their manufacturers, generally based on a measuring the complex impedance (impedance) of the inductor melt channel and measuring the temperature rise of water as it passes through the cooling system pipes [10].

The disadvantages of such systems are the impossibility of determining the location and dimensions of the areas of liquid metal flowing into the defects of the lining. However, this is important, because the melt channel has a branched shape (it consists of three branches and forms two contours as shown in Fig. 2,*a*), and the melt leakage can be directed both to the outer walls of the body and to the inner ones in the direction of the magnetic circuit with inductance coils.

Improvement of this diagnostic method can be the ability to determine the problem area of the melt channel according to the inductance impedance measured in practice. If we determine a quantitative relationship between the impedance of the inductor and the electrical characteristics of the separated parts of the melt contour, then they in turn can be related to the geometric characteristics of these parts (an increase or decrease in the local section – the occurrence of leakage or overgrowing of the channel). Obtaining such important information will allow us to more accurately predict the residual life of the induction channel furnace.

Therefore, the **aim of the paper** is to determine a quantitative relationship between the measured impedance of the inductor and the electrical characteristics of the separated parts of the melt contour for finding the leakage location of the liquid metal and thus improving the diagnostics system of the lining state of induction channel furnaces.

As a typical example of an induction channel furnace, we considered the UPCAST US20X-10 furnace in the line for the continuous casting of oxygen-free copper rod [10] with a power of 500 kW installed at PJSC «Yuzhkabel Works» (Kharkiv).

The general view of the investigated furnace is shown in Fig. 1.
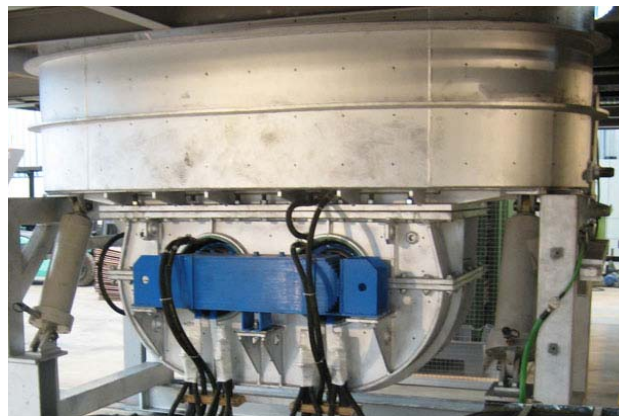
Fig. 1. Induction channel furnace for the production of copper rolled wire

Structurally, the furnace consists of a lined tank, which contains the whole mass of the metal being melted, and the inductor located under the tank [1, 5, 10]. The tank is connected with the melting channel filled with melt too. The copper template is lined with a refractory mixture with a working temperature of 1800 °C. After the template melting and sintering of the lining, a melting channel, which together with the adjacent part of the tank forms a closed conductive ring, is formed.

The principle of induction furnace operation is similar to the principle of the action of a single-phase power transformer in the short-circuit mode [1, 2]. However, the electric parameters of the furnace and the transformer are significantly different due to the difference in its design.

The inductor, whose turns are wound up on two rods of a closed magnetic circuit, is the primary winding of the transformer, and the secondary winding is the molten metal. The current flowing in the secondary circuit causes heating of the melt. At that almost all energy is released in the channel having a small cross section (90-95 % of the electric energy supplying the furnace is released in the channel).

The metal is heated owing to heat exchange and mass transfer between the channel and the tank. The movement of the metal is mainly determined by the action of the electrodynamic forces that arise in the channel and to a lesser degree by convection due to the overheating of the metal in the channel in comparison with tank [7, 8].

Electrical equivalent circuits of the induction channel furnace and calculation of their equivalent parameters. As a starting point, the paper considers two equivalent electric circuits (simplified equivalent electric circuits and refined one) of the inductor as a transformer with a short-circuited secondary winding as

well as we use the assumption based on the physical nature that when defects arise in the lining, the electrical parameters of the secondary liquid metal circuit of the induction furnace are changed.

The investigated induction furnace is schematically shown in Fig. 2,*a*. There are both main elements and the current contours in the molten metal indicated with dashed line in the figure.

In the secondary circuit formed by the melt, we can distinguish three branches (2-1-3, 2-3, 2-4-3), which, due to various geometric characteristics, can be conveniently divided into five sections (2-1, 1-3, 2-3, 2-4, 4-3), indicated by Roman numerals (I, II, III, IV, V) in Fig. 2,*a*.
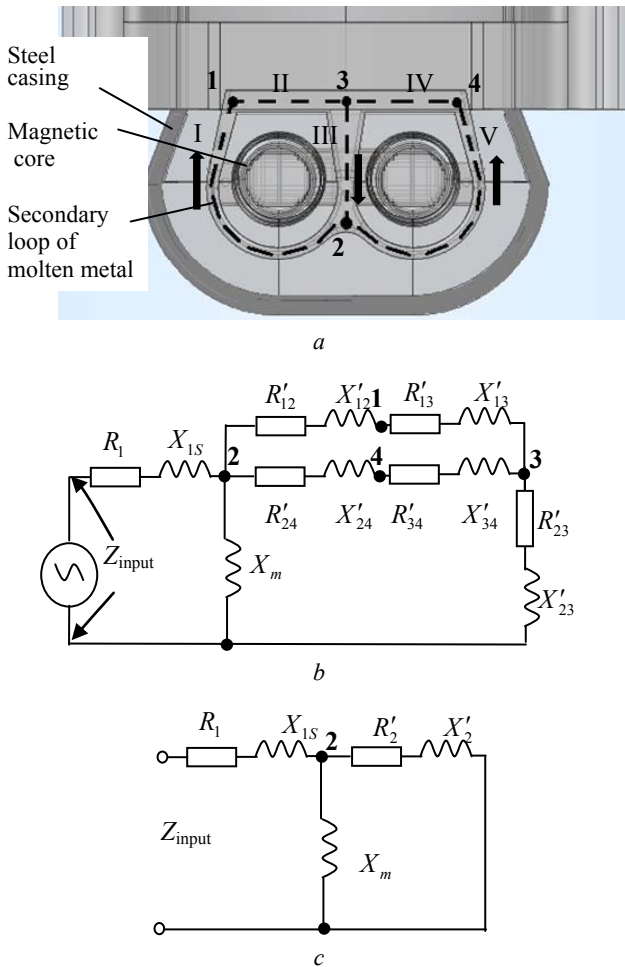

a

b

c

Fig. 2. *a* – configuration of induction channel furnace and *b* – its equivalent circuits with subdivision of the secondary circuit into separate branches; *c* – simplified equivalent circuit of the furnace when branches are replaced by a single turn with equivalent parameters

Fig. 2,*b* shows the electrical equivalent circuit of the furnace as an electrical transformer whose secondary winding has two short-circuited turns with a common branch III located between nodes 2 and 3 (see Fig. 2,*a*) through which the currents of both circuits flow.

The circuit under consideration includes the parameters of the inductor – the pure resistance and leakage inductance R_1, X_{1s}, the parameter of the magnetization circuit – X_m (which is caused by the magnetic flux in the magnetic core of inductor) and the

parameters of the secondary liquid-metal circuit reduced to the winding of the inductor as the primary winding of the transformer. In this case, each parts of branch of the secondary circuit in Fig. 2,*a* corresponds its own branch in the electrical equivalent circuit in Fig. 2,*b*.

A simplified equivalent circuit for the furnace is shown in Fig. 2,*c*. In this equivalent circuit the secondary circuit is presented in the form of a single turn with equivalent parameters R_2', X_2' reduced to the winding of the inductor. The complex impedance of the simplified equivalent circuit in Fig. 2,*c*, which is measured in practice at the inductor terminals, is determined by the following equation:

$$Z_{input} = Z_1 + \frac{jX_m(R_2' + jX_2')}{R_2' + j(X_m + X_2')}.$$

Hence the functional dependencies of the inductor resistances (pure resistance R_{input} and image impedance X_{input}) on the parameters of the secondary liquid-metal circuit R_2' and X_2' have the following form:

$$R_{input} = f_R(R_2', X_2') = \text{Re}(Z_{input}) =$$
$$= R_1 + \frac{X_m R_2'(X_2' + X_m) - X_m X_2' R_2'}{(R_2')^2 + (X_m + X_2')^2}; \quad (1)$$

$$X_{input} = f_X(R_2', X_2') = \text{Im}(Z_{input}) =$$
$$= X_{1S} + \frac{X_m(R_2')^2 + X_m X_2'(X_2' + X_m)}{(R_2')^2 + (X_m + X_2')^2}. \quad (2)$$

The dependences calculated on the basis of expressions (1) and (2) are shown in Fig. 3.

Note that here, for greater generality, all values are given in relative units and the graphs are valid regardless of the specific numerical values of the parameters of the equivalent circuit.

As an example, let us consider the following values of the parameters of the equivalent circuit, calculated on the basis of the geometric and electrical characteristics of the inductor coils, magnetic circuit and melt loop, as well as those indicated in the technical documentation for the furnace under study [10] and measured experimentally at PJSC «Yuzhkabel Works» [9]:

$$R_1 = 0.12 \text{ m}\Omega, \quad X_{1s} = 24 \text{ m}\Omega, \quad X_m = 0.2 \text{ }\Omega, \quad (3)$$
$$R_2'|_0 = 1.2 \text{ m}\Omega, \quad X_2'|_0 = 24 \text{ m}\Omega,$$
$$R_{input}|_0 = 1.08 \text{ m}\Omega, \quad X_{input}|_0 = 0.05 \text{ }\Omega. \quad (4)$$

Here, the basic values correspond to a furnace with a new lining without defects, as shown by the dot in Fig. 3 with values $R_2'/R_2'|_0 = 1$ and $X_2'/X_2'|_0 = 1$.

From the results obtained, we can conclude the following:

1) If in the furnace with initially defect-free lining parameters – $R_2'/R_2'|_0 = 1$ and $X_2'/X_2'|_0 = 1$ only the value R_2' will be increase (due to the occurrence of any defect in the lining), that this leads to an increase in the measured values both R_{input} and X_{input}.

Increasing only the value X_2' will lead, that value X_{input} will increase, but value R_{input} will decrease.

$R_{input}/R_{input}\big|_0$

$X'_2/X'_2\big|_0 = 0.7$

1.0
0.9
0.8
1.3
1.2
1.1

$R'_2/R'_2\big|_0$

a

$X_{input}/X_{input}\big|_0$

1.3
1.2
1.1
1.0
0.9
0.8
$X'_2/X'_2\big|_0 = 0.7$

$R'_2/R'_2\big|_0$
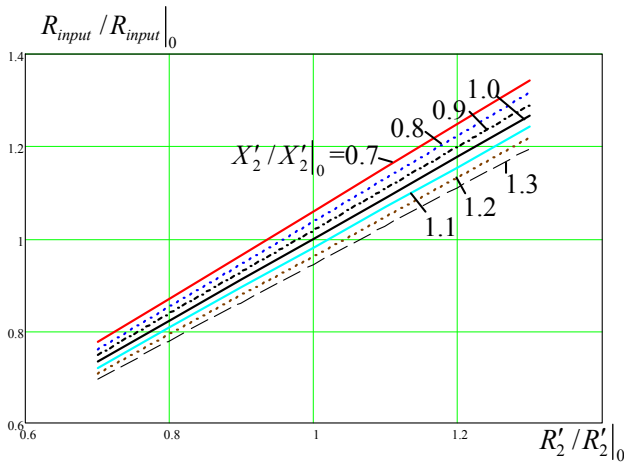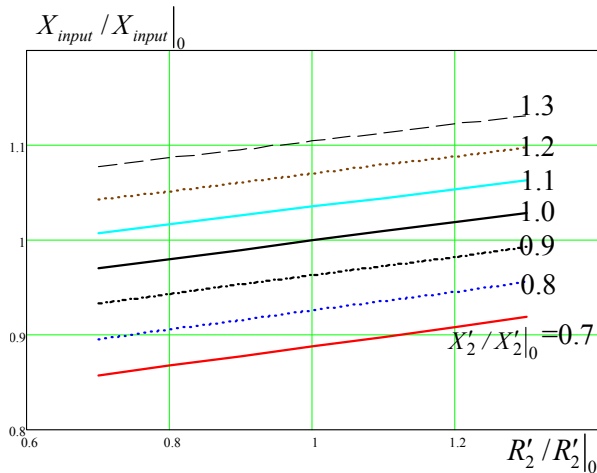
b

Fig. 3. Dependences of the relative value of the complex impedance of the inductor on relative values of pure resistance of secondary circuit and at various values of inductive impedance of the circuit: *a* – pure resistance; *b* –image impedance

2) In the general case, with simultaneous changes in both R'_2 and X'_2, the quantitative changes in the pure resistance and image impedance of the inductor can be determined from the graphs in Fig. 3.

3) Using the data in Fig. 3 or directly functional dependences (1) and (2) for relatively small changes in the values of R'_2 and X'_2 one can determine a linear relationship between their increments in the neighborhood of a point with a defect-free lining in the form of the following vector-matrix equation:

$$\begin{bmatrix} \dfrac{\Delta R_{input}}{R_{input}\big|_0} \\[2mm] \dfrac{\Delta X_{input}}{X_{input}\big|_0} \end{bmatrix} = \begin{bmatrix} 0.9 & -0.075 \\ 0.1 & 0.35 \end{bmatrix} \begin{bmatrix} \dfrac{\Delta R'_2}{R'_2\big|_0} \\[2mm] \dfrac{\Delta X'_2}{X'_2\big|_0} \end{bmatrix}. \qquad (5)$$

Here, the resulting matrix, which can be called the sensitivity matrix $A = \begin{bmatrix} 0.9 & -0.075 \\ 0.1 & 0.35 \end{bmatrix}$, characterizes the sensitivity of the change in the equivalent inductor resistances with respect to the change in the resistances of the secondary circuit in accordance with the simplified equivalent circuit in Fig. 2,*c*.

Note, that elements of matrix *A* are dimensionless and show the degree of influence of separated parameters of the secondary circuit (melt) on the input resistances of the inductor. Although, in this example the matrix *A* was calculated for the particular inductor, but within the framework of the proposed approach, it can be easily recalculated for an another one.

The relatively large values of the diagonal elements of the matrix *A* (0.9 and 0.35) indicate a strong connection between the pure resistances of the inductor and the secondary circuit and the less strong connection between their image impedance, and the small values the other matrix elements indicate relatively weak cross-connections. Moreover, the negative value of the coefficient, that equals to –0.075, attests a decrease in the value R_{input} with growth of R'_2.

4) For practice, it would be interesting to determine a feedback between the values increments. For this purpose, calculating the inverse sensitivity matrix A^{-1} from equation (5) we get:

$$\begin{bmatrix} \dfrac{\Delta R'_2}{R'_2\big|_0} \\[2mm] \dfrac{\Delta X'_2}{X'_2\big|_0} \end{bmatrix} = A^{-1} \begin{bmatrix} \dfrac{\Delta R_{input}}{R_{input}\big|_0} \\[2mm] \dfrac{\Delta X_{input}}{X_{input}\big|_0} \end{bmatrix} = \begin{bmatrix} 1.09 & 0.23 \\ -0.31 & 2.8 \end{bmatrix} \begin{bmatrix} \dfrac{\Delta R_{input}}{R_{input}\big|_0} \\[2mm] \dfrac{\Delta X_{input}}{X_{input}\big|_0} \end{bmatrix}. \quad (6)$$

This expression makes it possible to calculate and analyze the deviations of the parameters of the secondary liquid-metal circuit based on the measured deviations of the inductor parameters and then to estimate the probability of the appearance of any defect in the lining.

The obtained results are applied to the simplified equivalent circuit in Fig. 2,*c*. However, in practice, when analyzing the effect of lining defects on the parameters of the secondary circuit, it is expedient to use the refined equivalent circuit in Fig. 2,*b*. It allows to evaluate the effect of the defect directly on the parameters of each part of branch separately.

For the subsequent conversion to a simplified equivalent circuit and use of the results in Fig. 3, the following expressions can be used to determination the relationship between the parameters of the two equivalent circuits under consideration:

$$R'_2 = \mathrm{Re}((Z'_{12} + Z'_{13})\|(Z'_{24} + Z'_{34}) + Z'_{23}), \qquad (7)$$

$$X'_2 = \mathrm{Im}((Z'_{12} + Z'_{13})\|(Z'_{24} + Z'_{34}) + Z'_{23}). \qquad (8)$$

Here the parallel connection operator of two arbitrary complex impedances Z_1 and Z_2 is defined as:

$$Z_1\|Z_2 = Z_1 Z_2 /(Z_1 + Z_2).$$

With the help of expressions (7) and (8) and analyzing the processes and functional dependencies between all parameters of the refined equivalent circuit in Fig. 2,*b*, one can pass to the simplified circuit in Fig. 2,*c* and then use the graphical dependencies in Fig. 3 or

directly expressions (1) and (2), and in the case of small increments, expressions (5) and (6).

In practice, the inverse problem is usually solved: from the measured input impedance of the inductor the resistances Z'_{12}, Z'_{13}, Z'_{24}, Z'_{34}, and Z'_{23} are determined. For this, it is proposed to create a certain database of resistance values for various liner defects. For its filling, the values of Z'_{12}, Z'_{13}, Z'_{24}, Z'_{34}, and Z'_{23} are defined by a search of possible variants, where the upper and lower limits are determined from the electrical and geometrical characteristics of the parts of the melt channel, and the degree of sampling (step of changing in values) – from practical industrial necessity.

For each combination of resistances of channel parts, the values of R'_2 and X'_2 are determined. And as a consequence, by measuring them in practice, it is possible to set a suitable combination of channel resistance areas from the database.

The technique for calculating the influence of the parameters of the liquid-metal circuit on the values of the input impedances of the inductor. Let us consider the following example showing how the previously obtained results can be used to estimate the relationship between the parameters of a particular induction furnace.

We shall use the furnace with a defect-free lining with data according to (3) and base values according to (4), which correspond to the simplified equivalent circuit in Fig. 2,*c*. In the case of a defect-free lining, the secondary circuit parameters will be equal:

$$R'_2 = R'_2\big|_0 = 1{,}2 \text{ m}\Omega, \quad X'_2 = X'_2\big|_0 = 24 \text{ m}\Omega. \quad (9)$$

Turning to the refined equivalent circuit in Fig. 2,*b*, we consider that for the case of a defect-free lining the electrical parameters of the parts of branches (based on their configuration) are equal:

$$Z'_{12} = Z'_{24} = 0.8{+}\text{j}16 \text{ m}\Omega, \quad Z'_{13} = Z'_{34} = 0.8{+}\text{j}16 \text{ m}\Omega,$$

$$Z'_{23} = 0.4{+}\text{j}8 \text{ m}\Omega. \quad (10)$$

As an example, let us consider such «defect» when the lining thickness h in the branch V (in Fig. 2,*a*) becomes thinner by 10 %. Because of this fact, the complex impedance of the branch Z_{24}' will decrease by approximately 10 % of the value in expression (10) and amount to $Z_{24}' = 0.72 + \text{j}14.4$ mΩ.

In order to move to the simplified circuit from refined equivalent circuit, it is necessary to substitute new value Z_{24}' and all other values according to (10) in expressions (7) and (8). Then, performing transformations, we obtain new perturbed values of the parameters of the secondary circuit for the circuit in Fig. 2,*c*: $R_2' = 1.18$ mΩ, $X_2' = 23.6$ mΩ.

Comparing with the values for the defect-free lining (9), we can see how change in the value Z_{24}' by 10 % varies R_2' and X_2'. The new relative values R_2' and X_2' for the basis quantities according to (9) will be equal to

$$R'_2 / R'_2\big|_0 = 1.18/1.2 = 0.98, \quad X'_2 / X'_2\big|_0 = 23.6/24 = 0.98.$$

Further, using expression (5) for the case of small perturbations of the parameters values, let us finally determine how the inductor parameters change:

$$\begin{bmatrix} \dfrac{\Delta R_{input}}{R_{input}\big|_0} \\[2ex] \dfrac{\Delta X_{input}}{X_{input}\big|_0} \end{bmatrix} = \begin{bmatrix} 0.9 & -0.075 \\ 0.1 & 0.35 \end{bmatrix} \begin{bmatrix} 0.02 \\ 0.02 \end{bmatrix} = \begin{bmatrix} 0.017 \\ 0.009 \end{bmatrix}.$$

Thus, this example shows that decrease in the parameters of one branch in the circuit in Fig. 2,*b* by 2 % leads to decrease in the parameters of the entire secondary circuit in Fig. 2,*c* and this result in decrease in the input parameters of the inductor by 1.7 % for the pure resistance and by 0.9 % for the image impedance.

The sequence of operations for calculating the change in the values of the inductor parameters when the values of the equivalent circuit parameters are changed can be represented as a calculation technique consisting of the sequential execution of the following steps.

Step 1. For the investigated furnace, two equivalent circuits are selected – refined one and simplified one as in Fig. 2,*b* and *c*, respectively. Then, for simplified circuit, the graphics dependences are plotted according to Fig. 3,*a*, and for the case of small increments, the dependence (5) is constructed with determination of the sensitivity matrix A.

Step 2. To assess the effect of any lining defects we determine the influence degree of this defect on the particular branch parameters of the refined equivalent circuit in Fig. 2,*b*. It can be done, for example, using the basic expressions for calculating the transformer parameters or using the program packages to solve the corresponding field task.

Step 3. Using the expressions (7) and (8) the transition to the perturbed values of the parameters of the simplified circuit in Fig. 2,*c* is made, and then, according to the graphics dependences as in Fig. 3 for the investigated furnace or using the expression (5) in the case of small increments, the new values of the inductor parameters are determined.

Step 4. Based on the results of such calculations, a database is created for the different types of lining defects for a given furnace. The use of this database makes it possible to predict the state of furnace lining by periodic measurements of the inductor parameters.

Conclusions.

1. The paper considers one of the methods for diagnosing the state of the lining of an induction channel furnace. The method is based on comparison of the measured values of the complex impedances of the furnace inductor with a defect-free lining and lining with defects. In this case, only defects leading to a change in the electrical parameters of the secondary liquid-metal circuit are taken into account.

2. Using two electric equivalent circuits of the inductor, the analytic expressions and graphics dependencies determining a quantitative relationship between the parameters of the liquid-metal circuit and the inductor parameters measured in practice are obtained. In the case of small changes in these parameters (less than 10 %), a linear relationship between their increments is

---

used with the determination of a sensitivity matrix A, which clearly demonstrates the presence of strong or weak coupling between the perturbed values of the secondary circuit parameters and the inductor ones.

3. The technique for calculating the increments of equivalent inductor parameters as a function of increments of the parameters of the secondary liquid-metal circuit is proposed. The use of this technique allows to develop the database for various types of lining defects for a given furnace and on its basis predict the state of its lining by means of periodic measurements of the inductor parameters.

REFERENCES

1. Rudnev V., Loveless D., Cook R. *Handbook of induction heating.* CRC press, 2017. 736 p.
2. Vivek R. Gandhewar, Satish V. Bansod, Atul B. Borade. Induction Furnace – A Review. *International Journal of Engineering and Technology*, 2011, vol.3, no.4, pp. 277-284.
3. Lucia O., Maussion P., Dede E.J., Burdio J.M. Induction Heating Technology and Its Applications: Past Developments, Current Technology, and Future Challenges. *IEEE Transactions on Industrial Electronics*, 2014, vol.61, no.5, pp. 2509-2520. **doi: 10.1109/TIE.2013.2281162**.
4. Jin S., Harmuth H., Gruber D. Thermal and thermomechanical evaluations of channel induction furnace applying strong insulation containing lightweight aggregates. *Ironmaking & Steelmaking*, 2017, pp. 1-5. **doi: 10.1080/03019233.2017.1291153.**
5. Zolotarev V.M., Shcherba M.A., Zolotarev V.V., Belyanin R.V. Three-dimensional modeling of electromagnetic and thermal processes of induction melting of copper template with accounting of installation elements design. *Technical Electrodynamics*, 2017, no.3, pp. 13-21. **doi: 10.15407/techned2017.03.013**.
6. Asad A., Bauer K., Chattopadhyay K., Schwarze R. Numerical and Experimental Modeling of the Recirculating Melt Flow Inside an Induction Crucible Furnace. *Metallurgical and Materials Transactions B*, 2018, vol.49, no.3, pp. 1378-1387. **doi: 10.1007/s11663-018-1200-4.**
7. Lope I., Acero J., Carretero C. Analysis and Optimization of the Efficiency of Induction Heating Applications With Litz-Wire Planar and Solenoidal Coils. *IEEE Transactions on Power Electronics*, 2016, vol.31, no.7, pp. 5089-5101. **doi: 10.1109/TPEL.2015.2478075.**
8. Pham H.N., Fujita H., Ozaki K., Uchida N. Dynamic Analysis and Control for Resonant Currents in a Zone-Control Induction Heating System. *IEEE Transactions on Power Electronics*, 2013, vol.28, no.3, pp. 1297-1307. **doi: 10.1109/TPEL.2012.2210286**.
9. Zolotaryov V.M., Shcherba M.A., Belyanin R.V., Mygushchenko R.P., Kropachek O.Yu. Comparative analysis of electrical and thermal control of the lining state of induction apparatus of copper wire manufacture. *Electrical engineering & electromechanics*, 2018, no.1, pp. 35-40. **doi: 10.20998/2074-272X.2018.1.05.**
10. UPCAST®, Finland. *UPCAST technical documentation* Available at: http://www.upcast.com (accessed 12 May 2017).

O.D. Podoltsev[1], *Doctor of Technical Science, Professor,*
V.M. Zolotaryov[2], *Doctor of Technical Science, Professor,*
M.A. Shcherba[1], *Candidate of Technical Science,*
R.V. Belyanin[2],
[1] The Institute of Electrodynamics of the NAS of Ukraine, 56, prospekt Peremogy, Kiev-57, 03680, Ukraine, phone +380 44 3662460, e-mail: m.shcherba@gmail.com
[2] Private Joint-stock company Yuzhcable works, 7, Avtogennaya Str., Kharkiv, 61099, Ukraine, phone +380 57 7545228, e-mail: zavod@yuzhcable.com.ua

I.N. Khlopenko, S.A. Rozhkov, N.J. Khlopenko

STABILITY AND ACCURACY OF THE ROBUST SYSTEM FOR STABILIZING THE ROTOR FLUX-LINKAGE OF AN ASYNCHRONOUS ELECTRIC DRIVE AT RANDOM VARIATIONS OF THE UNCERTAIN PARAMETERS WITHIN THE SPECIFIED BOUNDARIES

Purpose. The aim is to investigate the stability and the accuracy of a robust system for stabilizing the rotor flux-linkage of an asynchronous electric drive at random variations of the uncertain parameters of the object and the regulator within the specified boundaries. Methodology. To make the research, the mathematical model of the rotor flux-linkage channel of the vector control system of an asynchronous electric drive with parametric uncertainty was applied. The transfer function of the H_∞-suboptimal regulator was calculated using the mixed sensitivity method. This transfer function was used to construct the regulator structural scheme in the form of a connection of proportional and integrating links and several adders. Analytical dependences of the coefficients of the regulator's transfer function on the parameters of links of such a connection are determined. These dependences served to researching the influence of uncertain parameters of the regulator links and the object on the stability of the robust system and the accuracy of flux-linkage stabilization. Results. Investigations of the robust system stability and the accuracy of flux-linkage stabilization in the Robust Control Toolbox are done. The curves of the flux-linkage transient processes and the Bode diagram for the open system at random variations of the indeterminate parameters of the object and the regulator links within the specified boundaries are constructed. A choice of variable parameters was carried out by the Monte Carlo method. By the scatter of the obtained curves of the transient processes, the accuracy of flux-linkage stabilization was determined, and according to the Bode diagram, stability reserves in the amplitude and the phase of the robust system were determined. A high accuracy of flux-linkage stabilization (deviation less than 1 %) in fairly wide ranges of changing the uncertain parameters of the object and the regulator, while maintaining the stability of the system with permissible reserves in amplitude and phase, is established. Originality. For the first time, analytical dependences of the coefficients of the transfer function of the H_∞-suboptimal regulator on the parameters of its structural scheme, which represented in the form of a connection of proportional and integrating links, are obtained. The method for calculating the stability of a robust flux-linkage control system and the accuracy of its stabilization at random variations of the uncertain parameters of the object and the regulator links within the specified boundaries is developed. Practical value. The use of the proposed method allows, during the design of the regulator, to ensure the selection of its elements from standard series. References 10, figures 3.
Key words: **electric drive, vector control, flux-linkage channel, stabilizing robust system, stability, accuracy.**

Цель. Целью работы является исследование устойчивости и точности робастной системы стабилизации потокосцепления ротора асинхронного электропривода при случайных вариациях неопределенных параметров объекта и регулятора в заданных границах. Методология. Для проведения исследований применялась математическая модель канала потокосцепления ротора системы векторного управления асинхронного электропривода с параметрической неопределенностью. Рассчитывалась передаточная функция H_∞-субоптимального регулятора по методу смешанной чувствительности. Эта передаточная функция использовалась для построения структурной схемы регулятора в виде соединения пропорциональных и интегрирующих звеньев и нескольких сумматоров. Определялись аналитические зависимости коэффициентов передаточной функции регулятора от параметров звеньев такого соединения. Эти зависимости служили для исследования влияния неопределенных параметров звеньев регулятора и объекта на устойчивость робастной системы и точность стабилизации потокосцепления. Результаты. Проведены исследования устойчивости робастной системы и точности стабилизации потокосцепления в пакете Robust Control Toolbox. Построены кривые переходных процессов потокосцепления и диаграмма Боде для разомкнутой системы при случайных вариациях неопределенных параметров объекта и звеньев регулятора в заданных границах. Выбор варьируемых параметров осуществлялся по методу Монте-Карло. По разбросу полученных кривых переходных процессов определялась точность стабилизации потокосцепления, а по диаграмме Боде – запасы устойчивости по амплитуде и фазе робастной системы. Установлена высокая точность стабилизации потокосцепления (отклонение менее 1 %) в достаточно широких диапазонах изменения неопределенных параметров объекта и регулятора при сохранении устойчивости системы с допустимыми запасами по амплитуде и фазе. Новизна. Впервые получены аналитические зависимости коэффициентов передаточной функции H_∞-субоптимального регулятора от параметров его структурной схемы, представленной в виде соединения пропорциональных и интегрирующих звеньев. Построена методика расчета устойчивости системы робастного управления потокосцепления и точности его стабилизации при случайных вариациях неопределенных параметров объекта и звеньев регулятора в заданных границах. Практическое значение. Использование предложенной методики позволяет в процессе конструирования регулятора обеспечить выбор его элементов из стандартных рядов. Библ. 10, рис. 3.
Ключевые слова: **электропривод, векторное управление, канал потокосцепления, робастная система стабилизации, устойчивость, точность.**

Introduction. In [1] the method of structural synthesis is constructed and the structure of the stabilizing robust H_∞-suboptimal regulator is obtained in the form of a connection of proportional and integrating links for the flux-linkage channel of the vector control system of an

asynchronous electric drive with parametric uncertainty of the control object. However, when designing such a regulator from analog devices (operational amplifiers and RC-circuit) there are rounding errors of its gain factors and time constants due to the selection of elements (resistors, capacitors) of these devices from standard series. The consideration of such rounding errors in the calculation model of the regulator with parametric uncertainty of the object is of fundamental importance for ensuring the stability of the robust system and the necessary accuracy of flux-linkage stabilization.

Robust systems of stabilizing the parameters of asynchronous electric drives are engaged in a number of domestic and foreign scientists [2-9]. They solved many problems both in the development of mathematical methods of research, and in studying the stability, accuracy of regulation, and the speed of systems with a given uncertainty of the object. However, the problem of the influence of the parametric uncertainty of the robust regulator on the stability and accuracy of the flux-linkage stabilization system was not considered. In this connection, the problem of studying the stability of a robust system and the accuracy of stabilizing the rotor flux-linking with the parametric uncertainty of the object and the regulator within given boundaries seems to be actual.

The goal of the work is study of the stability and accuracy of a robust system for stabilizing the rotor flux-linkage of an asynchronous electric drive at random variations of the indeterminate parameters of the object and the regulator within given boundaries.

Methods and results of research. The paper [1] contains a system of equations of state of an object consisting of a frequency converter and stator and rotor windings in the normal operator form:

$$px_1 = -\frac{1}{T_2}x_1 + \frac{L_{12}I_n}{T_2\Psi_n}x_2 ;$$

$$px_2 = -\frac{1}{T_{1eq}}x_2 + \frac{E_n}{R_{1eq}T_{1eq}I_n}x_3 ; \qquad (1)$$

$$px_3 = -\frac{1}{T_{fc}}x_3 + \frac{K_{fc}U_n}{T_{fc}E_n}u ,$$

where

$$x_1 = \frac{\Psi}{\Psi_n} ; \quad x_2 = \frac{I}{I_n} ; \quad x_3 = \frac{E}{E_n} ; \quad u = \frac{U}{U_n} ;$$

p is the Laplace operator; E is the frequency converter's EMF; U is the control action; I is the current in the rotor flux-linkage channel; Ψ is the rotor flux-linkage vector's module; T_{fc} is the time constant of the frequency converter; $T_{1eq}=L_{1eq}/R_{1eq}$ is the electromagnetic time constant of the stator winding, where $R_{1eq}=R_1+(k_r)^2R_2$ and $L_{1eq}=\sigma L_1$ are its equivalent resistance and the leakage inductance; R_1, R_2 are the active resistances of the stator and rotor windings; $T_2=L_2/R_2$ is the electromagnetic time constant of the rotor winding; L_1, L_2 are the inductances of the stator and rotor windings; L_{12} is the mutual

inductance of the stator and rotor windings; $\sigma=1 - (L_{12})^2/(L_1 L_2)$ is the coefficient of magnetic field scattering; $k_r=L_{12}/L_2$.

In this paper, this system of equations, together with the undefined parameters K_{fc}, R_{1eq}, R_2, L_1, L_2 and L_{12} of the object, is used to construct a mathematical model for the stability and accuracy of a robust system for stabilizing the rotor flux-linkage of an asynchronous electric drive at random variations of uncertain parameters within given boundaries.

To construct such a model, the system of equations (1) is reduced to the canonical form [1]:

$$px = Ax + B_1w + B_2u ;$$

$$z = C_1x + D_{11}w + D_{12}u ; \qquad (2)$$

$$y = C_2x + D_{21}w + D_{22}u ,$$

where

$$A = \begin{bmatrix} -\dfrac{R_{2n}}{L_{2n}} & \dfrac{R_{2n}}{L_{2n}} & 0 \\ 0 & -\dfrac{R_{1eqn}}{L_{1eqn}} & \dfrac{R_{1eqn}}{L_{1eqn}} \\ 0 & 0 & -\dfrac{1}{T_{fc}} \end{bmatrix} ;$$

$$B_1 = \begin{bmatrix} 0 & 0 & 0 & \dfrac{p_{R_2}}{L_{2n}} & \dfrac{p_{L_{12}}}{L_{2n}} & -p_{L_2} & -\dfrac{p_{R_2}}{L_{2n}} \\ 0 & -p_{L_{1eq}} & -\dfrac{p_{R_{1eq}}}{L_{1eqn}} & 0 & 0 & 0 & 0 \\ \dfrac{p_{K_{fc}}}{T_{fc}} & 0 & 0 & 0 & 0 & 0 & 0 \end{bmatrix} ;$$

$$C_1 = \begin{bmatrix} 0 & 0 & 0 \\ 0 & -\dfrac{R_{1eqn}}{L_{1eqn}} & \dfrac{R_{1eqn}}{L_{1eqn}} \\ 0 & R_{1eqn} & 0 \\ 0 & R_{2n} & 0 \\ 0 & R_{2n} & 0 \\ -\dfrac{R_{2n}}{L_{2n}} & \dfrac{R_{2n}}{L_{2n}} & 0 \\ R_{2n} & 0 & 0 \end{bmatrix} ; \quad C_2 = \begin{bmatrix} 1 & 0 & 0 \end{bmatrix};$$

$$D_{11} = \begin{bmatrix} 0 & 0 & 0 & 0 & 0 & 0 & 0 \\ 0 & -p_{L_{1eq}} & -\dfrac{p_{R_{1eq}}}{L_{1eqn}} & 0 & 0 & 0 & 0 \\ 0 & 0 & 0 & 0 & 0 & 0 & 0 \\ 0 & 0 & 0 & 0 & 0 & 0 & 0 \\ 0 & 0 & 0 & p_{R_2} & 0 & 0 & 0 \\ 0 & 0 & 0 & \dfrac{p_{R_2}}{L_{2n}} & \dfrac{p_{L_{12}}}{L_{2n}} & -p_{L_2} & -\dfrac{p_{R_2}}{L_{2n}} \\ 0 & 0 & 0 & 0 & 0 & 0 & 0 \end{bmatrix} ;$$

$$B_2^T = \begin{bmatrix} 0 & 0 & \dfrac{1}{T_{fc}} \end{bmatrix} ; \quad D_{12}^T = \begin{bmatrix} 1 & 0 & 0 & 0 & 0 & 0 & 0 \end{bmatrix};$$

$$D_{21} = \begin{bmatrix} 0 & 0 & 0 & 0 & 0 & 0 & 0 \end{bmatrix} ; \quad D_{22} = \begin{bmatrix} 0 \end{bmatrix};$$

$x = (x_1, x_2, x_3)^T$ is the phase vector; y is the one-dimensional output vector which closes the feedback; $z = (z_1, z_2, \ldots, z_7)^T$, $w = (w_1, w_2, \ldots, w_7)^T$ are, respectively, the input and output uncertainty vectors interconnected by the matrix expression $w(p) = \Delta(p) \cdot z(p)$ in which the uncertainty matrix $\Delta(p)$ has a diagonal form.

The written canonical form of equations (2) together with the weight functions [10] for control the quality of the robust stabilization system, allows in the Robust Control Toolbox to calculate the transfer function of the H_∞-suboptimal regulator for the nominal object. This transfer function can be represented in the form

$$K(p) = k \frac{p^2 + b_1 p + b_2}{p^3 + a_1 p^2 + a_2 p + a_3}, \qquad (3)$$

where k, a_1, a_2, a_3, b_1, b_2 are the regulator parameters.

We assume that the transfer function of the regulator (3) retains its form for random variations of the parameters k, a_1, a_2, a_3, b_1, b_2.

Then, expanding (3) into a continued fraction by the Euclidean algorithm, we obtain the block diagram of the regulator shown in Fig. 1. It contains the undefined parameters k, k_1, k_2, k_3, T_1, T_2, caused, as already noted earlier, by rounding errors that occur when designing the regulator.
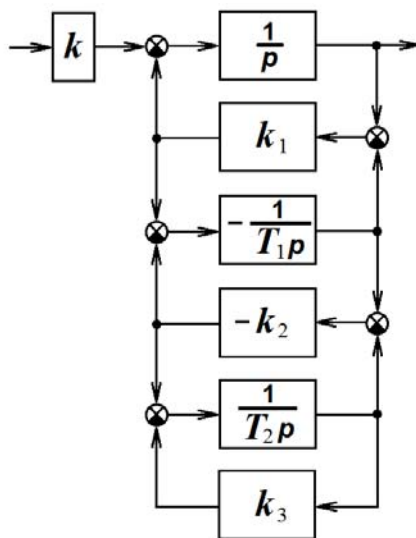

Fig. 1. Structural scheme of H_∞-suboptimal stabilizing robust controller

We replace the structural scheme shown in Fig. 1 by equivalent circuit under the rules of transformation of structural schemes. Then we obtain the following expressions for the coefficients of the polynomials of the numerator and denominator of the transfer function of the robust regulator (3):

$$b_1 = \frac{1}{T_1}(k_2 - k_1) + \frac{1}{T_2}(k_3 - k_2); \quad a_1 = k_1 + b_1;$$

$$b_2 = \frac{1}{T_1 T_2}\left[k_3(k_2 - k_1) + k_1 k_2\right]; \qquad (4)$$

$$a_2 = b_2 + k_1\left[\frac{k_2}{T_1} + \frac{1}{T_2}(k_3 - k_2)\right]; \quad a_3 = \frac{k_1 k_2 k_3}{T_1 T_2}.$$

The system of equations (1) together with (3) and expressions (4) serves to investigate the stability and accuracy of the rotor flux-linkage stabilization system at random variations of the indeterminate parameters of the object and regulator within given boundaries.

The accuracy of flux-linkage stabilization is determined by the spread of the curves of its modulus of transient processes, and the stability reserves by amplitude and phase - according to the Bode diagram at various random variations of the undefined parameters of the regulator k, k_1, k_2, k_3, T_1, T_2 and the object K_{fc}, R_{1eq}, R_2, L_1, L_2, L_{12} within specified boundaries. In this case, the Monte Carlo method is used for random choice of parameters [10]. Calculations are performed in MATLAB and terminated when, in the steady state mode of the system, transients do not exceed the boundaries of a one-percent «tube».

The procedure for calculating the stability and accuracy of the rotor flux-linkage stabilization system at random variations of undefined parameters within given boundaries is reduced to the following sequence of actions:

1. The transfer function (3) of the regulator for the nominal object is calculated.

2. The decomposition of the found transfer function into a continued fraction is performed.

3. The block diagram of the regulator is formed (see Fig. 1) corresponding to a continued fraction, and its nominal parameters k_n, k_{1n}, k_{2n}, k_{3n}, T_{1n}, T_{2n} are calculated.

4. The transfer function of the object (1) is programmatically determined.

5. The system is formed by the command of flux-linkage stabilization from the series-connected transfer functions of the regulator (3) and the object (1) covered by a single feedback.

6. The curves of the flux-linkage transients and the Bode diagram for the open system are calculated with random variations of the parameters of the object K_{fc}, R_{1eq}, R_2, L_1, L_2, L_{12} and regulator k, k_1, k_2, k_3, T_1, T_2 within the specified boundaries.

7. The accuracy of the flux-linkage stabilization is determined from the scales of the curves of the transients, and the stability reserves in the amplitude and phase are determined from the Bode diagram.

The numerical solution was carried out at the following values of the initial data: $T_{fc} = 0.001$ s; $R_{1n} = 2.65$ Ω; $R_{2n} = 2.0$ Ω; $L_{1n} = 0.186$ H; $L_{2n} = 0.189$ H; $L_{12n} = 0.179$ H; $\sigma = 0.0996$ corresponding the asynchronous electric drive with motor MDXMA100-32.

The nominal parameters of the regulator calculated from these data turned out to be equal to: $k_n = 5.016 \cdot 10^5$; $k_{1n} = 1.436 \cdot 10^4$; $k_{2n} = 1.752 \cdot 10^4$; $k_{3n} = 3.473 \cdot 10^3$; $T_{1n} = 19.70$ s; $T_{2n} = 1.256 \cdot 10^3$ s.

Undefined parameters of the object varied in the ranges ±90 %, and the parameters of the regulator k_1, k_2 – in the ranges ±3 %, k –in the range ±15 %, and k_3, T_1, T_2 in the ranges ±20 % of their nominal values.

Fig. 2 shows 20 curves of transients of the rotor flux-linkage corresponding to random variations of the undefined parameters of the object and the regulator selected within the prescribed boundaries by the Monte Carlo method. They are obtained in the packages of the MATLAB application for a single step change in the control action.

As can be seen, the curves of the transients shown in Fig. 2 do not exceed the limits of 1 % of the tube.
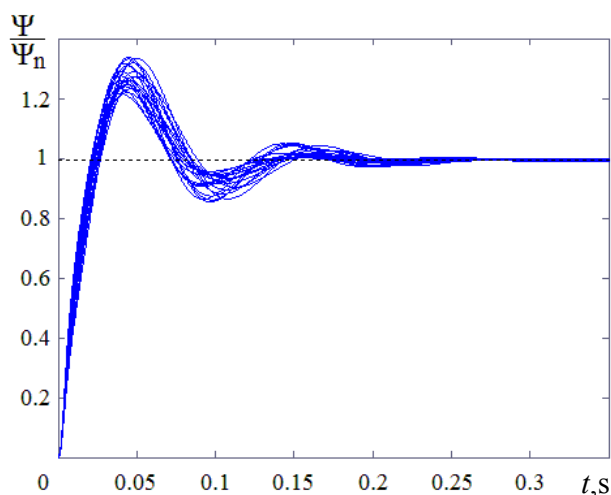

Fig. 2. Transients of the rotor flux-linkage

Fig. 3 shows the Bode diagram with 20 generated curves of amplitude $L(\omega)$ and 20 phase $\varphi(\omega)$ frequency characteristics with the same uncertain parameters as in the previous case.
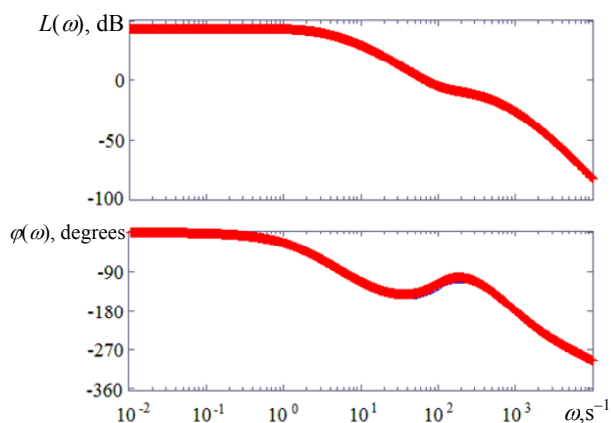

Fig. 3. The Bode diagram of the open system

From the amplitude $L(\omega)$ and phase $\varphi(\omega)$ characteristics presented in this diagram, it is seen that the system is stable, since the amplitude characteristic crosses the abscissa axis before the phase characteristic, finally decaying, goes over the value of the angle −180°. In this case, the calculated value of the stability reserve in amplitude is 19.9 dB, and in phase – 47.9° for nominal values of the object and regulator parameters for variance of random curves not exceeding 4 dB for amplitude and 15° for phase frequency characteristics.

Thus, the results of the calculations confirm the expediency of using the proposed method for constructing robust H_∞-suboptimal regulators from elementary links.

Conclusions.

1. For the first time, analytical dependences of the coefficients of the transfer function of the H_∞-suboptimal regulator from the parameters of its structural scheme represented as a combination of proportional and integrating links are obtained.

2. A method is developed for calculating the stability and accuracy of a robust system for stabilizing the rotor flux-linkage of an asynchronous electric drive at random variations of the indeterminate parameters of the object and the regulator within given boundaries.

3. The results of the calculations show a high accuracy of flux-linkage stabilization (deviation less than 1 %) and a low sensitivity of the robust stabilization system to random variations of uncertain parameters within given wide enough boundaries.

REFERENCES
1. Khlopenko N.J., Khlopenko I.N. Structural synthesis of a stabilizing robust controller of the rotor flux linkage. *Electrical engineering & electromechanics*, 2017, no.1, pp. 21-25. (Rus). **doi: 10.20998/2074-272X.2017.1.04.**
2. Elistratov V.D., Ilina A.G. Robust control by servo drive with non-rigid load with H-infinity norm limitation. *Vestnik of Astrakhan State Technical University. Series: Marine Engineering and Technologies*, 2016, no.4, pp. 89-94. (Rus).
3. Kuznetsov B.I., Nikitina T.B., Kolomiets V.V., Khomenko V.V. Investigation of the effect of nonlinearities and variations of the control object parameters on dynamic characteristics of the electromechanical servo systems. *Bulletin of NTU «KhPI»*, 2015, no.12(1121), pp. 68-71. (Rus).
4. Nesenchuk A.A., Opeiko O.F., Odnolko D.S. Dynamics simulation and calculation of robust parameters for the electric drive control system on the basis of the root locus portraits. *Artificial Intelligence*, 2014, no.3, pp. 90-103. (Rus).
5. Nikitina T.B. Pareto optimal solution of multiobjective synthesis of robust controllers of multimass electromechanical systems based on multiswarm stochastic multiagent optimization. *Electrical engineering & electromechanics*, 2017, no.2, pp. 34-38. **doi: 10.20998/2074-272X.2017.2.05.**
6. Peresada S.M., Kovbasa S.N., Bovkunovich V.S. Rough vector control torque and flux induction motor. *Technical electrodynamics*, 2010, no.1. pp. 60-66. (Ukr).
7. Potapenko E.M., Kazurova A.E., Savranskaya A.V. Review of works on dynamics of multimass uncertain electromechanical systems carried out in ZNTU electric drive department. *Electrical Engineering and Power Engineering*, 2011, no.1, pp. 7-10. (Rus). **doi: 10.15588/1607-6761-2011-1-1.**
8. Ostroverkhov M.J., Pyzhov V.M. Robust speed vector control system of gated inductor type electrical drive.

Electromechanical and energy saving systems, 2015, iss.3/2015(31), pp. 32-38. (Ukr).
9. Rudnev E.S., Morozova D.I. μ-synthesis of robust speed controller of synchronous electric drives. *Electrotechnic and computer systems*, 2015, no.20, pp. 42-50. (Rus). **doi: 10.15276/eltecs.20.96.2015.06.**
10. Richard Y., Chiang R., Michael G., Safonov M. *MATLAB: Robust Control Toolbox. User's Guide. Version 2*, 1998. 230 p. Available at: http://www.mathworks.com (Accessed 12 May 2016).

I.N. Khlopenko[1]*, Master of Science,*
S.A. Rozhkov[1]*, Doctor of Technical Sciences, Professor,*
N.J. Khlopenko[2]*, Doctor of Technical Sciences, Professor,*
[1] Kherson State Marine Academy,
20, Ushakov Ave., Kherson, 73009, Ukraine,
e-mail: rozhkov_ser@meta.ua
[2] Admiral Makarov National University of Shipbuilding,
3, Central Ave., Nikolaev, 54021, Ukraine,
e-mail: khlopenko.n@gmail.com

V.M. Boev

CALCULATION OF TRANSIENTS IN ELECTRICAL CIRCUITS WITH «INCORRECT» INITIAL CONDITIONS WITH THE HELP OF THE DUHAMEL INTEGRAL AND DISCONTINUOUS FUNCTIONS

A technique for calculating transients using the Duhamel integral and discontinuous functions is presented. On specific examples, the procedure for calculating «incorrect» problems with respect to differential equations, compiled according to Kirchhoff laws, and using the Duhamel integral is presented. In this case, the Kirchhoff law and the transition characteristic in the Duhamel integral are written using unitary discontinuous functions for the electrical circuit as a whole (before and after commutation). It is shown that the application of discontinuous functions for describing piecewise continuous input signals and switching in an electric circuit extends the domain of applicability of the Duhamel integral. References 9, figures 3.
Key words: **transients, Duhamel integral, discontinuous functions.**

Излагается методика расчета переходных процессов с использованием интеграла Дюамеля и разрывных функций. На конкретных примерах излагается порядок расчета «некорректных» задач по дифференциальным уравнениям, составляемым по законам Кирхгофа, и с помощью интеграла Дюамеля. При этом законы Кирхгофа и переходная характеристика в интеграле Дюамеля записываются с помощью единичных разрывных функций для электрической цепи в целом (до и после коммутации). Показано, что применение разрывных функций для описания кусочно-непрерывных входных сигналов и переключений в электрической цепи расширяет область применимости интеграла Дюамеля. Библ. 9, рис. 3.
Ключевые слова: **переходные процессы, интеграл Дюамеля, разрывные функции.**

The state of the art and problem definition. In theoretical electrical engineering, the basic methods for calculating transients in electrical circuits are: classical, operator, frequency (spectral) and based on the use of the Duhamel integral [1]. The domain of preferential application of the Duhamel integral is electrical circuits with an input signal of arbitrary shape.

In recent years, publications have appeared in which the Duhamel integral is used to calculate the process of propagation of the electromagnetic field (lightning discharges, industrial interferences, etc.) in an inhomogeneous medium [2, 3]. In this case, the field problem is represented by a substitution circuit in the form of a long line or a four-terminal network [3, 4]. The transition characteristic required for the Duhamel integral is determined by the substitution circuit. In [5], the Duhamel integral is used in the calculation of the electromagnetic field in a layered medium. Thus, the Duhamel integral remains a sought-after method and the extension of its applicability range (in this case to electric circuits with «incorrect» initial conditions, when the switching laws in the formulation for current in the inductance and the voltage on the capacitance are not applicable) is relevant.

The drawbacks of the Duhamel integral include the requirement of zero initial conditions and the impossibility of taking into account the switching that changes the structure of the electrical circuit. These constraints can be leveled by using discontinuous (stepwise) functions to describe piecewise continuous input signals and changes in the structure of the circuit during switching.

The connection of an electric circuit at a constant voltage U_1 at zero initial conditions can be considered as an action of the input voltage $U = 1(t)U_1$ in the circuit already switched on [1], where $1(t)$ is the Heaviside unit function (connection function) (see Fig. 1). This statement is also true for the variable input voltage

$u(t) = u(t) = 1(t) \cdot u_1(t)$. Then the Duhamel integral can be represented in the form of the integral

$$ i(t) = \int_{-0}^{t} u'(\Theta) h(t - \Theta) d\Theta , \qquad i(t) = \int_{-t_0}^{t} u'(\Theta) h(t - \Theta) d\Theta , \quad (1) $$

where

$$ u'(\Theta) = \frac{du(t)}{dt}\Big|_{t=\Theta} = [1(t)u_1(t)]^1\big|_{t=\Theta} = [\delta(t)u_1(0) + $$
$$ + 1(t)u'(t)_1]\big|_{t=\Theta} = \delta(\Theta)u_1(0) + 1(\Theta)u_1'(\Theta). $$

Then

$$ i(t) = \int_{-t_0}^{t} [\delta(\Theta)u_1(0) + 1(\Theta)u_1'(\Theta)] h(t - \Theta) d\Theta = $$

$$ = u_1(0)h(t)\int_{-t_0}^{t}\delta(\Theta)d\Theta + \int_{-t_0}^{t} u_1'(\Theta)h(t-\Theta) \cdot 1(\Theta) d\Theta = \quad (2) $$

$$ = u_1(0)h(t) + \int_{0}^{t} u_1'(\Theta)h(t-\Theta)d\Theta. $$

Here, the filtering property of the unit function and the δ-function is taken into account. Θ is the time of occurrence of voltage surges into which the input voltage $u_1(t)$ in accordance with the physical meaning of the Duhamel integral is divided, $(t - \Theta)$ is the time of action of each of the voltage jumps, $h(t - \Theta)$ is the transition conductivity for each of the voltage jumps.

Formula (2) is one of the varieties of the Duhamel integral. Formulas (1), (2) are written for the current. But the output function can be voltage (or current) in any branch of the electrical circuit and then the transition conductivity $h(t - \Theta)$ should be replaced by the corresponding voltage (or current) transition function.

If the input signal $u_1(t)$ starts to act at $t < 0$, then in the formulas (1), (2) the lower limit of integration can be referred to infinity $t_0 = \infty$.

It was shown in [6, 7] that the transient occurring in an electrical circuit under the action of a complex piecewise continuous signal (including the one starting to act at $t = t_0 < 0$) can be calculated in two ways:

1. Description of the input signal and the general form of the solution by one analytical expression with the help of single stepwise functions and substitution of the general form of the solution in the differential equation for the sought value.

2. By the formulas of the Duhamel integral. In this case, the description of the input signal by one analytical expression with the help of discontinuous (stepwise) functions allows us to use the Duhamel integral for signals that begin to act also for $t = t_0 < 0$.

Examples of such calculations are given in [6, 7].

Non-zero initial conditions take place in the electrical circuit when the transient occurs as a result of a change in the structure of the circuit (connection or disconnection of individual circuit elements). The transient can also be calculated in the following two ways:

1. The change in the parameters of the electric circuit is described by means of discontinuous functions and is found in the differential equation for the sought value. The input voltage is assumed to be switched on in some preceding commutation time $t = t_0 < 0$. We write the solution of the differential equation with the aid of discontinuous functions as consisting of two parts (for $t < 0$ and $t > 0$) and substitute it into the differential equation. If the process is assumed to be steady before the commutation ($t = 0$), then this will be the initial state of the circuit with non-zero initial conditions (in this case, only the forced component is used in the solution for $t < 0$).

2. In the formulas of the Duhamel integral, the input voltage is also considered to begin to act at the time $t = t_0 < 0$ which is written using discontinuous functions. The transient function $h(t)$ (with respect to current or voltage) is written using discontinuous functions as consisting of two parts, corresponding to the circuits before and after commutation.

In [6, 7], examples are given with switching in circuits that change the active resistance R. The question of transients for the general case, with switching changes in the inductance L and capacitance C (when the switching laws in the formulation for the current in the inductance and the voltage in the capacitor not applicable) remains unresolved, which is the subject of this paper.

The goal of the paper is to justify the possibility of calculating transients in an electrical circuit with «incorrect» initial conditions using the Duhamel integral and discontinuous functions.

Main part. To describe the sudden changes in the voltages, currents and parameters of the electrical circuit, we use discontinuous functions written with the aid of the modulo function [6] (Fig. 1):

- Fig. 1,*a*: $f_1(t) = 1(t-a) = \dfrac{1}{2}\left(1 + \dfrac{|t-a|}{t-a}\right)$ – unit

Heaviside function;

- Fig. 1,*b*:

$$f_2(t) = 1(t-a) + 1(b-t) - 1 = \frac{1}{2}\left(\frac{|t-a|}{t-a} - \frac{|t-b|}{t-b}\right), \quad a < b;$$

- Fig. 1,*c*: $f_3(t) = 1(b-t) = \dfrac{1}{2}\left(1 - \dfrac{(t-b)}{t-b}\right)$ – inverse
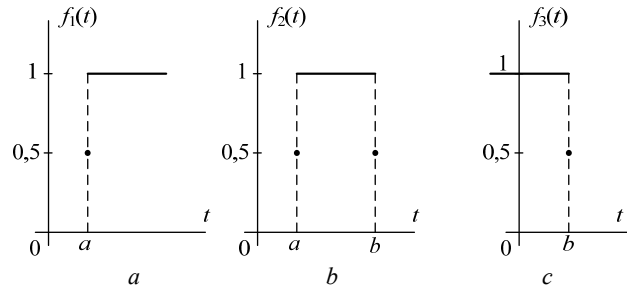
Heaviside function.

Fig. 1

We also calculate the differential equations, compiled according to Kirchhoff laws, and the Duhamel integral. In the first case, Kirchhoff laws are compiled for the electrical circuit as a whole (before and after commutation), and the difference of these circuits is taken into account for by unitary discontinuous functions.

In the second case, the transition characteristic in the Duhamel integral is written for the circuit as a whole (before and after commutation) by means of unit discontinuous functions.

We consider the circuit (Fig. 2), in which the current in the inductance changes abruptly.
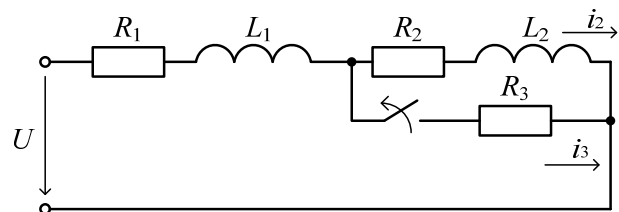

Fig. 2

Kirchhoff laws for such a circuit:

$$R_1 i_1 + L_1 \frac{di_1}{dt} + R_2 i_2 + L_2 \frac{di_2}{dt} = U; \qquad (3)$$

$$R_2 i_2 + L_2 \frac{di_2}{dt} = R_3 i_3; \qquad (4)$$

$$i_1 = i_2 + i_3 \frac{1}{2}\left(1 - \frac{|t|}{t}\right). \qquad (5)$$

Here we took into account the change in the structure of the parallel section with the help of single discontinuous functions, and written Kirchhoff laws for the circuit as a whole (before and after switching).

From (4) we find

$$i_3 = \frac{R_2}{R_3} i_2 + \frac{L_2}{R_3} \frac{di_2}{dt}.$$

We solve the problem with respect to the current i_2:

$$i_2(t) = \frac{1}{2}\left(1 - \frac{|t|}{t}\right)i_0(t) + \frac{1}{2}\left(1 + \frac{|t|}{t}\right)i(t).$$

Then from equation (5) we obtain:

$$i_1(t) = \frac{1}{2}\left(1 - \frac{|t|}{t}\right)(i_0 + i_3) + \frac{1}{2}\left(1 + \frac{|t|}{t}\right)i =$$

$$= \frac{1}{2}\left(1 - \frac{|t|}{t}\right)\left(i_0 + \frac{R_2}{R_3}i_0 + \frac{L_2}{R_3}\frac{di_0}{dt}\right) + \frac{1}{2}\left(1 + \frac{|t|}{t}\right)i.$$

We substitute this in equation (3):

$$\frac{1}{2}\left(1 - \frac{|t|}{t}\right)\left[\left(1 + \frac{R_2}{R_3}\right)R_1 i_{0+} \frac{R_1}{R_3}L_2 \frac{di_0}{dt}\right] + L_1\left[\left(1 + \frac{R_2}{R_3}\right)\frac{di_0}{dt} +$$

$$+ \frac{L_2}{R_3}\frac{d^2 i_0}{dt^2}\right]\frac{1}{2}\left(1 - \frac{|t|}{t}\right) + L_1\left[\left(1 + \frac{R_2}{R_3}\right)i_0 + \frac{L_2}{R_3}\frac{di_0}{dt}\right](-\delta(t)) +$$

$$+ \frac{1}{2}\left(1 - \frac{|t|}{t}\right)\left[R_2 i_0 + L_2\frac{di_0}{dt}\right] - \delta(t)i_0 L_2 + \frac{1}{2}\left(1 + \frac{|t|}{t}\right)\times$$

$$\times\left[(R_1 + R_2)i + (L_1 + L_2)\frac{di}{dt}\right] + \delta(t)(L_1 + L_2)i =$$

$$= U = \frac{1}{2}\left(1 - \frac{|t|}{t}\right)U + \frac{1}{2}\left(1 + \frac{|t|}{t}\right)U.$$

We equate multipliers for the same discontinuous functions:

1) $\quad \frac{1}{2}\left(1 - \frac{|t|}{t}\right) : \frac{R_3 + R_2}{R_3}\left(R_1 i_0 + \frac{di_0}{dt}L_1\right) +$

$$+ \frac{L_2}{R_3}\left(R_1\frac{di_0}{dt} + L_1\frac{d^2 i_0}{dt^2}\right) + R_2 i_0 + L_2\frac{di_0}{dt} = U, \qquad (6)$$

2) $\quad \frac{1}{2}\left(1 + \frac{|t|}{t}\right) : (R_1 + R_2)i + (L_1 + L_2)\frac{di}{dt} = U, \qquad (7)$

3) $\delta(t) : L_1\frac{R_3 + R_2}{R_3}i_0 + \frac{L_1 L_2}{R_3}\cdot\frac{di_0}{dt} + L_2 i_0 = (L_1 + L_2)i. \quad (8)$

Equation (6) is the differential equation of the circuit before commutation:

$$\frac{L_1 L_2}{R_3}\frac{d^2 i_0}{dt^2} + \left(\frac{R_1}{R_3}L_2 + \frac{R_3 + R_2}{R_3}L_1 + L_2\right)\frac{di_0}{dt} +$$

$$+ \frac{R_3 + R_2}{R_3}R_1 i_0 + R_2 i_0 = U.$$

Its solution:

$$i_0(t) = i_{\text{force}} + i_{\text{free}} = i_{\text{force}} + A_1 e^{k_1 t} + A_2 e^{k_2 t},$$

where i_{force}, i_{free} are the forced and free current components respectively.

But before commutation, we are interested in the steady-state process, i.e. $i_{\text{force}} = \text{const}$:

$$i_{\text{force}} = i_0 = \frac{UR_3}{(R_2 + R_3)R_1 + R_2 R_3} = i_2(0-). \qquad (9)$$

Equation (7) is the differential equation of the circuit after commutation. Its solution:

$$i(t) = i_{\text{force}} + i_{\text{free}} = \frac{U}{R_1 + R_2} + Ae^{-\frac{t}{\tau}}; \quad \tau = \frac{L_1 + L_2}{R_1 + R_2}. \quad (10)$$

In equation (8) we take into account that $di_0/dt = 0$,

since $i_0 = i_{\text{force}} = \text{const}$ and $\dfrac{R_3 + R_2}{R_3}i_0 = i_1(0-)$. Then

$$L_1 i_1(0-) + L_2 i_2(0-) = (L_1 + L_2)i_2(0+),$$

since in our notation $i(0) = i_2(0+)$.

Thus, equation (8) is the first commutation law for flux linkages.

We substitute values:

$$\left(\frac{R_2 + R_3}{R_3}L_1 + L_2\right)\frac{UR_3}{R_1(R_2 + R_3) + R_2 R_3} =$$

$$= \left(\frac{U}{R_1 + R_2} + A\right)(L_1 + L_2).$$

We found the constant A:

$$A = \frac{U}{L_1 + L_2}\cdot\frac{(R_2 + R_3)L_1 + R_3 L_2}{R_1(R_2 + R_3) + R_2 R_3} - \frac{U}{R_1 + R_2} =$$

$$= \frac{UR_2(L_1 R_2 - L_2 R_1)}{(L_1 + L_2)(R_1 + R_2)(R_1 R_2 + R_1 R_3 + R_2 R_3)}. \qquad (11)$$

The same solution was obtained in [8].

If $R_3 = 0$, i.e. before switching the section $(R_2 - L_2)$ was short-circuited, then

$$A = \frac{U(L_1 R_2 - L_2 R_1)}{(L_1 + L_2)(R_1 + R_2)R_1},$$

which coincides with the solution given in [1].

We solve this problem using the Duhamel integral and obtain the same result. We believe that the electrical circuit before switching was switched on to the voltage U at the time $t = -t_0 < 0$

$$u(t) = \frac{1}{2}\left(1 + \frac{|t + t_0|}{t + t_0}\right)U. \qquad (12)$$

Assuming that the transient from the switching on to the time of commutation $t = 0$ has already ended, we write the transient conductivity of the circuit before commutation for the current i_2 by the forced component (9):

$$h_0(t) = \frac{R_3}{R_1 R_2 + R_1 R_3 + R_2 R_3}.$$

The transient conductivity for the circuit after commutation, according to (10), (11), is equal to:

$$h(t) = \frac{1}{R_1 + R_2} + \frac{R_2(L_1 R_2 - L_2 R_1)}{(L_1 + L_2)(R_1 + R_2)(R_1 R_2 + R_1 R_3 + R_2 R_3)}e^{-\frac{t}{\tau}}.$$

Then, according to (1), we obtain:

$$i_2(t) = \int_{-0}^{t} u'(\Theta')\left[\frac{1}{2}\left(1 - \frac{|t|}{t}\right)h_0(t - \Theta') + \frac{1}{2}\left(1 + \frac{|t|}{t}\right)h(t - \Theta')\right]d\Theta' =$$

$$= \int_{-t_0}^{t} U\delta(\Theta + t_0)\left[\frac{1}{2}\left(1 - \frac{|t|}{t}\right)\frac{R_3}{R_1 R_2 + R_1 R_3 + R_2 R_3} + \frac{1}{2}\left(1 + \frac{|t|}{t}\right)\times\right.$$

$$\times\left[\frac{1}{R_1 + R_2} + \frac{R_2(L_1 R_2 - L_2 R_1)}{(L_1 + L_2)(R_1 + R_2)(R_1 R_2 + R_1 R_3 + R_2 R_3)}\times\right.$$

$$\left.\left.\times e^{-\frac{(t - \Theta - t_0)}{\tau}}\right]\right]d\Theta = \frac{1}{2}\left(1 - \frac{|t|}{t}\right)\frac{R_3 U}{R_1 R_2 + R_1 R_3 + R_2 R_3} +$$

$$+\frac{1}{2}\left(1+\frac{|t|}{t}\right)\left[\frac{U}{R_1+R_2}+\right.$$

$$\left.+\frac{R_2(L_1R_2-L_2R_1)U}{(R_1R_2+R_1R_3+R_2R_3)(L_1+L_2)(R_1+R_2)}e^{-\frac{t}{\tau}}\right].$$

Here: $\Theta' = \Theta + t_0$ is the input signal coordinate

$$\int\limits_{-t_0'}^{t}\delta(\Theta+t_0)d\Theta=1 \ ; \quad \int\limits_{-t_0'}^{t}\delta(\Theta+t_0)fd\Theta=f(-t_0).$$

Here: the lower limit $-t_0'$ is less than $-t_0$ by an infinitesimal value (i.e. $-t_0' = -t_0 - 0$);

$$\frac{1}{2}\left(1-\frac{|t|}{t}\right)=1 \ \ (\text{at } t < 0) \text{ is the current multiplier}$$

before commutation;

$$\frac{1}{2}\left(1+\frac{|t|}{t}\right)=1 \ \ (\text{at } t > 0) \text{ is the current multiplier}$$

before commutation;

These multipliers do not take part in integration with respect to Θ, since they separate the range of the formulas of the transient conductivity of the output signal before and after switching.

We consider a circuit with a capacitive energy storage device, where commutation changes the capacitance in the circuit (Fig. 3).
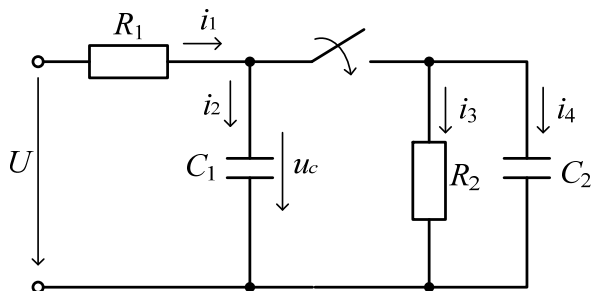

Fig. 3

Initial data: $U = 60$ V, $R_1 = R_2 = 1$ kΩ, $C_1 = 1$ μF, $C_2 = 2$ μF. We determine i_1.

Kirchhoff laws for the circuit as a whole (before and after switching):

$$R_1 i_1 + u_c = U \ ;$$

$$i_1 = i_2 + \frac{1}{2}\left(1+\frac{|t|}{t}\right)(i_3+i_4);$$

$$i_2 = c_1\frac{du_c}{dt} \ ;$$

$$i_3 = \frac{u_c}{R_2} \ ;$$

$$i_4 = c_2\frac{du_c}{dt} \ .$$

We substitute the currents into the first equation:

$$R_1 c_1\frac{du_c}{dt}+u_c+\frac{1}{2}\left(1+\frac{|t|}{t}\right)\left(R_1 c_2\frac{du_c}{dt}+\frac{R_1}{R_2}u_c\right)=U \ . \ \ (13)$$

We write the voltage u_c as the sum of the voltages before and after the commutation separated by unit discontinuous functions.

$$u_c(t)=\frac{1}{2}\left(1-\frac{|t|}{t}\right)u_0+\frac{1}{2}\left(1+\frac{|t|}{t}\right)u \ .$$

We substitute into the differential equation (13)

$$\frac{1}{2}\left(1-\frac{|t|}{t}\right)\left[u_0+R_1 c_1\frac{du_0}{dt}\right]-\delta(t)R_1 c_1 u_0+$$

$$+\frac{1}{2}\left(1+\frac{|t|}{t}\right)\left[\left(1+\frac{R_1}{R_2}\right)u+R_1(c_1+c_2)\frac{du}{dt}\right]+$$

$$+\delta(t)R_1(c_1+c_2)u=U \ .$$

We equate multipliers for the same discontinuous functions:

1) $\quad \frac{1}{2}\left(1-\frac{|t|}{t}\right): \ R_1 c_1\frac{du_0}{dt}+u_0=U \ ;$ (14)

2) $\ \frac{1}{2}\left(1+\frac{|t|}{t}\right): \ R_1(c_1+c_2)\frac{du}{dt}+\left(1+\frac{R_1}{R_2}\right)u=U \ ;$ (15)

3) $\quad \delta(t): \ -R_1 c_1 u_0+R_1(c_1+c_2)u=0 \ .$ (16)

The solution of equation (14) for the circuit before commutation has the form:

$$u_0(t)=U+Ae^{-\frac{t}{\tau}}=U-Ue^{\frac{-(t+t_0)}{\tau}} \ ; \quad \tau=\frac{1}{R_1 c_1}.;$$

Since before the commutation at some time $t = -t_0 < 0$ the circuit $(R_1 - c_1)$ was switched on to the voltage U, then this transient is considered to be completed before the time $t = 0$. Then:

$$u_0(t)=u_{c_1}(0-)=U \ .$$

The solution of equation (15) for the circuit after commutation is:

$$u_0(t)=\frac{UR_2}{R_2+R_1}+Ae^{\frac{-t}{\tau}}=30+Ae^{\frac{-t}{\tau}} \ ;$$

$$\tau=(c_1+c_2)\frac{R_1 R_2}{R_1+R_2}=1{,}5\cdot10^{-3} \text{ c.}$$

Equation (16) is the second commutation law for charges

$$c_1 u_0(0-)=(c_1+c_2)u(0+),$$

i.e.

$$c_1 u_{c_1}(0-)=(c_1+c_2)u_c(0+).$$

After substitution, we obtain equality for the determination of the constant A

$$c_1 U=(c_1+c_2)\left[\frac{UR_2}{R_1+R_2}+A\right].$$

From here:

$$A=U\left(\frac{c_1}{c_1+c_2}-\frac{R_2}{R_1+R_2}\right)=60\left(\frac{1}{3}-\frac{1}{2}\right)=-10 \ .$$

Then:

$$u_c(t)=\frac{1}{2}\left(1-\frac{|t|}{t}\right)60+\frac{1}{2}\left(1+\frac{|t|}{t}\right)\left(30-10e^{-\frac{2}{3}\cdot10^3 t}\right).$$

The source current:

$$i_1(t) = (c_1 + c_2)\frac{du_c}{dt} + \frac{u_c}{R_2} = 3 \cdot 10^{-2} + 10^{-2} e^{-\frac{2}{3} \cdot 10^3 t}.$$

The same result was obtained in [9].

We solve the same problem with the help of the Duhamel integral. The transient response of the circuit for the voltage before and after commutation has the form:

$$h(t) = \frac{1}{2}\left(1 - \frac{|t|}{t}\right) \cdot 1 + \frac{1}{2}\left(1 + \frac{|t|}{t}\right)\left[\frac{R_2}{R_1 + R_2} + \right.$$

$$\left. + \left(\frac{c_1}{c_1 + c_2} - \frac{R_2}{R_1 + R_2}\right)e^{\frac{-(t - \Theta')}{\tau}}\right].$$

We assume that the circuit was switched on at a certain time $t = -t_0 < 0$ by the voltage (12) before the commutation, and this transient ended before the commutation time $t = 0$. Then the Duhamel integral (1) has the form:

$$u_c(t) = \int_{-0}^{t} u'(\Theta')h(t - \Theta')d\Theta' = \int_{-t_0}^{t} U\delta(\Theta + t_0)\left[\frac{1}{2}\left(1 - \frac{|t|}{t}\right) + \right.$$

$$+ \frac{1}{2}\left(1 + \frac{|t|}{t}\right)\left[\frac{R_2}{R_1 + R_2} + \left(\frac{c_1}{c_1 + c_2} - \frac{R_2}{R_1 + R_2}\right) \times\right.$$

$$\left.\left.\times e^{\frac{-(t - \Theta - t_0)}{\tau}}\right]\right]d\Theta = \frac{1}{2}\left(1 - \frac{|t|}{t}\right)U + \frac{1}{2}\left(1 + \frac{|t|}{t}\right) \times$$

$$\times \left[\frac{R_2 U}{R_1 + R_2} + U\left(\frac{c_1}{c_1 + c_2} - \frac{R_2}{R_1 + R_2}\right)e^{\frac{-t}{\tau}}\right].$$

The same solution for u_c was obtained above. If in this solution $R_2 \to \infty$, then we obtain a solution for the circuit (Fig. 3) without R_2, which is given in [1]:

$$u_c(t) = U + U\left(\frac{c_1}{c_1 + c_2} - 1\right)e^{\frac{-t}{\tau}}.$$

Conclusions.

1. For the first time, the possibility of calculating transients in an electric circuit with «incorrect» initial conditions with the help of the Duhamel integral and discontinuous functions is justified.

2. The proposed solution of the problem of calculating transients in the electrical circuit with non-zero and «incorrect» initial conditions with the help of the Duhamel integral is more compact than the known ones.

REFERENCES
1. Neyman L.R., Demirchyan K.S. *Teoreticheskie osnovy elektrotekhniki. V 2-kh t. T. 1* [Theoretical bases of electrical engineering. In 2 vols. Vol. 1]. Leningrad, Energoizdat Publ., 1981, p. 536. (Rus).
2. Kochetov S.V., Wollenberg G. Stable and Effective Full-Wave PEEC Models by Full-Spectrum Convolution Macromodeling. *IEEE Transactions on Electromagnetic Compatibility*, 2007, vol.49, no.1, pp. 25-34. **doi: 10.1109/temc.2006.888183.**
3. Konnikov I.A. Interference of an elementary source of an electromagnetic field in an electronic module. *Technology of electromagnetic compatibility*, 2006, no.4, pp.18-26. (Rus).
4. Elmore W.C. The Transient response of Damped Linear Networks with Particular Regard to wideband Amplifiers. *Journal of Applied Physics*, 1948, vol.19, no.1, pp. 55-63. **doi: 10.1063/1.1697872.**
5. Konnikov I.A. Calculation of the electromagnetic field in a layered medium. *Electricity*, 2017, no.7, pp. 60-67. (Rus).
6. Boev V.M. The use of discontinuous functions for the calculation of transient processes and impulse actions in linear electric circuits. 1. Transient processes. *Electronic modeling*, 2002, vol.24, no.6, pp. 67-79. (Rus).
7. Boev V.M. The use of discontinuous functions for the calculation of transient processes and impulse actions in linear electric circuits. 2. Impulse effects. *Electronic modeling*, 2003, vol.25, no.1, pp. 83-97. (Rus).
8. Rybalko M.P., Esaulenko V.O., Kostenko V.I. *Teoretichni osnovi elektrotehniki. Liniyni elektrichni kola: Pidruchnik.* [Theoretical foundations of electrical engineering. Linear electric circuits: Textbook]. Donetsk, Novyi Svit Publ., 2003. 513 p. (Ukr).
9. Shebes M.P. *Zadachnik po teorii lineynyih elektricheskih tsepey* [Tasks of problems in the theory of linear electrical circuits]. Moscow, Vysshaya Shkola Publ., 1982. 488 p. (Rus).

Received 03.04.2018

V.M. Boev, Doctor of Technical Science, Professor,
National Technical University «Kharkiv Polytechnic Institute»,
2, Kyrpychova Str., Kharkiv, 61002, Ukraine,
phone +380 57 7076961

M.I. Baranov, S.G. Buriakovskyi, S.V. Rudakov

THE TOOLING IN UKRAINE OF MODEL TESTS OF OBJECTS OF ENERGY, AVIATION AND SPACE-ROCKET ENGINEERING ON RESISTIBILITY TO ACTION OF PULSED CURRENT OF ARTIFICIAL LIGHTNING

Purpose. Presentation and analysis of the modern state of the tooling in Ukraine of model tests of objects of energy, aviation and space-rocket engineering on resistibility to the action of pulsed current of artificial lightning. Methodology. Electrophysics bases of technique of high-voltage and high pulsed currents, theoretical bases of electrical engineering, engineering of high electric and magnetic fields. Scientific methods of analysis of research and technical information. Results. Information regarding the modern consisting of Ukraine of high-voltage high-current pulsed engineering intended for the leadthrough of model tests of aircrafts and power objects on resistibility to the direct or indirect action on them of pulsed current of artificial lightning in accordance with the requirements of normative documents of the USA SAE ARP 5412: 2013, SAE ARP 5416: 2013 and International Standard IEC 62305-1: 2010. Basic technical descriptions are presented of developed and created in Ukraine for the aims of model tests of the technical objects marked higher on resistibility to lightning of two powerful high-voltage generators of current of lightning (GCL) of type of UITOM-1 and GTM-10/350, playback on the tested objects the pulses of current of artificial lightning with the rationed peak-temporal parameters in obedience to the indicated normatively-technical documents. Examples are resulted and the results of model tests are indicated on described domestic GCL of some elements and devices of the tested technical objects on resistibility to direct action on them of pulsed current of artificial lightning. It is shown that technical descriptions indicated domestic powerful GCL conform to the high requirements of operating in the leading countries of the world of normative documents to on resistibility to lightning objects of industrial energy, aviation and space-rocket engineering. Originality. First in the summarizing concentrated kind possibilities are shown developed and created domestic scientists and specialists of unique high-voltage high-current electrophysics equipment for the aims of leadthrough of integration model tests on resistibility and fire safety of aircrafts and power objects at lightning strike. Practical value. Application in practice of model tests of objects of industrial energy, aviation and space-rocket engineering on complex resistibility and fire safety to the striking action on them of pulsed current of artificial lightning, generated in discharge circuits of two described powerful domestic GCL, will be instrumental in the successful decision of global in the world problem of protecting from lightning of air and surface technical objects and being in them personnel. References 20, tables 2, figures 15.
Key words: **domestic powerful high-voltage high-current generators of current of lightning, objects of energy, aviation and space-rocket engineering, results of model tests of some technical objects on resistibility to the direct action of pulsed current of artificial lightning.**

Изложено современное состояние инструментального обеспечения в Украине натурных испытаний объектов промышленной энергетики, авиационной и ракетно-космической техники на стойкость к прямому (косвенному) воздействию на них импульсного тока искусственной молнии. Показано, что подобные испытания технических объектов на молниестойкость могут проводиться в полевых условиях на уникальном отечественном высоковольтном сильноточном электрооборудовании в соответствии с требованиями нормативных документов США SAE ARP 5412: 2013, SAE ARP 5416: 2013 и международного стандарта IEC 62305-1: 2010. Описаны основные технические характеристики разработанных и созданных в Украине для целей натурных испытаний отмеченных выше технических объектов на молниестойкость двух мощных высоковольтных генераторов тока молнии (ГТМ) типа УИТОМ-1 и ГТМ-10/350, воспроизводящих на испытываемых объектах импульсы тока искусственной молнии с нормированными амплитудно-временными параметрами согласно указанных технических документов. Приведены примеры и указаны результаты натурных испытаний на описанных ГТМ некоторых устройств технических объектов на стойкость к прямому воздействию на них импульсного тока искусственной молнии. Библ. 20, табл. 2, рис. 15.
Ключевые слова: **отечественные мощные высоковольтные сильноточные генераторы тока молнии, объекты энергетики, авиационной и ракетно-космической техники, результаты натурных испытаний некоторых технических объектов на стойкость к прямому действию импульсного тока искусственной молнии.**

Introduction. Technical progress in modern society objectively leads to the complication of the various techniques used by people and the active use in it of low-current electronics sensitive to the action of external powerful electromagnetic interference (PEMI) on it [1]. One source of such PEMI is a long spark discharge in the air atmosphere of the Earth of a thundercloud (lightning) into the ground, a neighboring cloud, a protected aircraft or a ground object [2-4]. The frequency of such discharges in the terrestrial troposphere is numerically in average of about 100 s^{-1} [2, 3]. The total electric charge accumulated in a thundercloud due to bipolar electrification processes in the warm ascending air flows of its fine-dispersed inclusions (for example, small droplets and water vapor, fine solid dielectric particles,

small granules and ice crystals [5, 6] of ±(50-200) C at the indicated discharge of a thunderstorm cloud causes a powerful pulsed current of a complex time shape in the plasma channel to flow with amplitude up to ± (30-200) kA [2, 3]. Thus, the US technical guidelines SAE ARP 5412: 2013 [7] and SAE ARP 5416: 2013 [8] define the requirements for the normalized amplitude-time parameters (ATP) of artificial lightning current pulses, generated by powerful high-voltage generators of currents of lightning (GCL) and used for field testing of aviation and rocket and space equipment for lightning resistibility. International Standard IEC 62305-1: 2010 [9] regulates the current requirements for normalized ATPs of generated by a powerful high-voltage GCL aperiodic

current pulse of artificial lightning with a time shape of 10/350 µs characteristic of a short thunderstorm strike in a protected ground facility and applied in field tests of many industrial facilities of power engineering for lightning resistibility. The development, creation and practical application of these GCLs are topical tasks in the world.

The goal of the paper is to describe and analyze the current state of tooling in Ukraine for testing power engineering, aviation and rocket and space equipment for resistibility to the action of pulsed current of artificial lightning.

1. General information and basic ATPs for pulsed current of artificial lightning. According to [10], when analyzing the scientific and technical problems we are considering, the notion of «*resistibility*» of an object to lightning includes the following three definitions:

• «*electromagnetic resistibility*» of the object, which means the ability of the object under investigation to resist the action of pulsed voltages and currents induced from the flow of linear lightning in the electrical circuits of its constituent elements to a certain level, while maintaining its operative state;

• «*electrothermal resistibility*» of the object, which means the ability of the object under investigation to resist the effect of the temperature of the heating of the materials of its structural elements arising in the dynamic mode from the current of the linear lightning, to its specified level, while maintaining its operative state;

• «*electromechanical resistibility*» of the object, which means the ability of the object under investigation to resist the dynamic effect of mechanical stresses arising from the flow of linear lightning current in the materials of its structural elements to a certain level, while maintaining its operative state.

In this connection, when carrying out the corresponding complex tests of technical facilities for lightning resistibility with the help of powerful high-voltage high-current GCL, it is necessary to comply with all the technical requirements of normative documents [7-9] in order to determine the above-mentioned types of resistibility based on the results of these tests. Sometimes by the test program and technique of testing technical objects for lightning resistibility the rest team can also be limited to the experimental determination of their most critical resistibility to the effect of artificial lightning current with given normalized ATPs [10]. As a rule, tests for the lightning resistibility of technical objects according to [7-9] are carried out by direct action of the plasma channel of the simulated lightning discharge to the test elements of the object. It is also possible to test objects by indirectly action the indicated discharge channel to the elements of the object located near the lightning passage.

According to the current technical requirements [7, 8], when testing aircraft and rocket and space equipment for lightning resistibility, the following components of artificial lightning current generated in high-voltage high-current GCL circuits can be used: pulse *A*- (or repetitive pulsed *D*-), intermediate *B*- and long-term *C*- (or shortened long-term *C**-) current components

of artificial lightning. In the practice of tests for the lightning resistibility of various devices and systems of civil and military aircrafts, the following combinations of these lightning current components are most often used [7, 8, 11]: *A*-, *B*- and *C*-components; *A*-, *B*- and *C** -components; *D*-, *B*- and *C**-components. The main normalized by [7, 8] ATPs, typical for such components of the current of artificial lightning in the circuits of GCL, are summarized below in Table 1.

From the data of Table 1 and the practice of testing technical objects for lightning resistibility it follows that the values of I_m and τ_f determine the electromagnetic and electromechanical resistibility of the tested elements of the object under the influence of the artificial lightning current component under consideration. At the same time, the values of q_0, τ_p and J_a determine the thermal energy released on the test element of the technical object, and accordingly its electrothermal resistibility to the lightning current. It can be seen that the pulsed *A*- component and the long-term *C*- component of the lightning current are the main components in the total lightning current. It depends on them the lightning resistibility of the object being tested in the discharge circuits of a powerful GCL. It should be noted that in the practical implementation of a powerful GCL on the basis of high-voltage capacitive energy storage (capacitor banks), each of the listed in Table 1 component of artificial lightning current is formed on the electric load of the test element of the object by separate capacitor banks of different energy intensities having different charging voltages. In this regard, the task of synchronizing the operation of such batteries as part of a single GCL comes to the fore.

Table 1

Normalized ATPs of the main components
of artificial lightning current [7, 8]

Lightning current component	I_m, kA	I_c, kA	q_0, C	J_a, 10^6 J/Ω	τ_f, µs	τ_p, ms
A	200±20	–	–	2±0.4	≤50	≤0.5
B	–	2±0.4	10±1	–	–	5±0.5
C	0.2÷0.8	–	200±40	–	–	$(0.25÷1)·10^3$
C*	–	0.4	6÷18	–	–	15÷45
D	100±10	–	–	0.25±0.05	≤25	≤0.5

Note. I_m –current pulse amplitude; I_c – average current value; q_0 – amount of flowed charge; J_a – current pulse action integral; τ_f, τ_p – respectively, the duration of the pulse front between the levels $(0.1-0.9)I_m$ and the current pulse on the level $≤0.1I_m$.

In accordance with the requirements of the current standards [9, 12], power engineering facilities for lightning resistibility are tested by an aperiodic current pulse of the time shape of 10/350 µs of both polarities, generated by a special powerful GCL. Normalized ATPs of this test current pulse of artificial lightning, corresponding to a short lightning strike into the protected technical object, are given in Table 2.

From the data of Table 1, 2 it follows that the test pulse of the current of 10/350 µs on the energy parameters (primarily on the value of the integral of its action J_a) substantially exceeds the corresponding values for the pulsed *A*- and repetitive pulsed *D*- components of

artificial lightning current used in aircraft lightning resistibility tests. Thus, for the level I of lightning protection of a ground object for the same values of the current amplitude $I_m=\pm(200\pm20)$ kA, this difference with respect to the pulse A- component of the total current of artificial lightning is for the integral of the action of the current J_a within five times.

Table 2
Normalized ATPs of an aperiodic pulse current of the time shape 10/350 μs [9, 12]

Name of the current pulse parameter	Lightning protection level of the facility according to the standard IEC 62305-1: 2010		
	I	II	III-IV
Front duration τ_f, μs	10±2	10±2	10±2
Pulse puration at half-descend τ_p (on the level 0,5I_m), μs	350±35	350±35	350±35
Current amplitude I_m, kA	200±20	150±15	100±10
Action integral J_a, 10^6 J/Ω	10±3.5	5.6±1.96	2.5±0.875
Charge q_0, C	100±20	75±15	50±10

In this connection, testing of technical objects for lightning resistibility with the use instead of pulsed A-component of an artificial lightning of an aperiodic current pulse of a time shape of 10/350 μs (the case of a short lightning strike by [9, 12]) should be considered as more stringent than their lightning resistibility tests according to requirements [7, 8]. At the same time, one should not overlook the strong electrothermal effect on the metal and composite elements of the test object of the long-term C-current component of artificial lightning, according to [7, 8], which carries through its round support zone at the object of relatively small outer diameter (up to 6 mm [10]) the huge values of the electric charge q_0 (up to ±200 C).

2. The generator of artificial lightning current type УИТОМ-1. In 2007, a unique powerful high-voltage high-current GCL of the УИТОМ-1 type [11] was created by the staff of the Scientific-&-Research Planning-&-Design Institute «Molniya» of the NTU «KhPI» at its experimental range (Andreevka village, Kharkiv region) [11], capable of field testing the objects aviation and rocket and space technology for lightning resistibility in accordance with stringent requirements [7, 8]. The general view of this GCL is shown in Fig. 1, and its principal electrical circuit is shown in Fig. 2. It can be seen from this circuit that a powerful generator of the УИТОМ-1 type includes five separate high-voltage pulse current generators (PCG), which form the required normalized components of the artificial lightning current on the common electrical (as a rule, active-inductive) load. In this case, the types of current components determine the name of these generators: PCG-A, PCG-B, PCG-D, PCG-C and PCG-C*.

The use of electrical jumpers in the circuit in Fig. 2 allows the combination of the current components required by [7, 8] to be obtained at the total load (TO). The generators PCG-A and PCG-D are equipped in parallel with high-voltage low-inductance capacitors of

Fig. 1. General view of a powerful high-voltage high-current generator of artificial lightning current of the type УИТОМ-1 (in the foreground there is a desktop with a high-voltage three-electrode air controlled switch with steel electrodes for a voltage of ±50 kV and pulsed sinusoidal lightning current up to ±220 kA, a tested sample of the skin of an aircraft and an air drawing system, and in the background – separate high-voltage pulse current generators for the corresponding current components A, B, C, C* and D) [11]
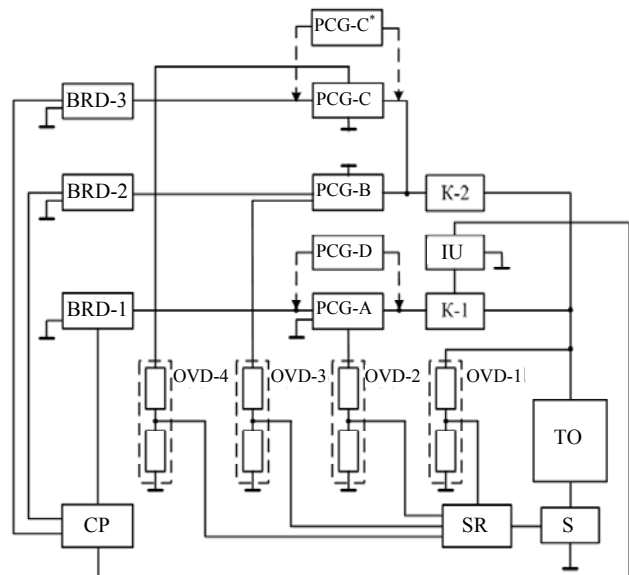

Fig. 2. Principal block electrical circuit for constructing a powerful lightning current generator of the type УИТОМ-1, containing individual pulse current generators PSG-A, *PSG*-B, PSG-D, PSG-C and PSG-C* (K-1, K-2 – high-voltage air switches for ±50 and ±5 kV; IU – ignition unit for ±100 kV; BRD-1, BRD-2 and BRD-3 – boost-rectifying devices for charging high-voltage capacitors of generators PSG-A, PSG-B, PSG-D, PSG-C and PSG-C*, CP – control panel, OVD-1, OVD-2, OVD-3 and OVD-4 – ohmic voltage dividers for voltage measurement on capacitors of generators PSG-A, PSG-B, PSG-D, PSG-C and PSG-C*, SR – system for recording measured voltages and currents in the circuits of generators PSG-A, PSG-B, PSG-D, PSG-C and PSG-C*; S – measuring shunt; TO – tested object) [11]

the type ИК-50-3 (rated voltage ±50 kV, nominal capacity 3 μF), respectively, in the amount of 111 and 36 pcs. At the same time, PCG-A is characterized by a nominal stored energy of 416 kJ, and PCG-D – 135 kJ. The generators PCG-B, PCG-C and PCG-C* are equipped

with parallel-connected high-voltage low-inductance capacitors of ИМ-5-140 type (rated voltage ±5 kV; nominal capacity 140 µF) in the amount of 18, 324 and 34 pcs., respectively.

In this regard, they have a nominal energy capacitance of 31.5, 567 and 59.5 kJ. As a result, the nominal energy capacitance of a powerful GCL of the УИТОМ-1 type is approximately 1.21 MJ [11]. Each capacitor of the generators PSG-*A*, PSG-*B*, PSG-*D*, PSG-*C* and PSG-*C** (with their total number of 523 pieces) from the emergency operation modes of these capacitor batteries (for example, electrical breakdown of one of the capacitors on the stage of charge or discharge) is equipped with a protective device mounted on its high-voltage terminal and made of several parallel-connected protective constant graphite-ceramic resistors of the ТВО-60 type of nominal of 24 or 100 Ω [13].

Switching in high-current discharge circuits of the PSG-*A* and PSG-*D* generators is carried out by a controlled high-voltage air cascade type K-1 discharger (see Fig. 2) for a nominal voltage of ±50 kV [11, 14]. This discharger is controlled by feeding a high-voltage microsecond voltage pulse of a damped sinusoidal shape of amplitude of ±100 kV from a special starting generator of the ГВПИ-100 type (IU in Fig. 2) to its middle electrode. To switch the high-current discharge circuits of the PSG-*B*, PSG-*C* and PSG-*C** generators, a high-voltage air two-electrode K-2 discharger (see Fig. 2) is used for a voltage of ±5 kV, rectangular electrodes of which are made of erosion-resistant graphite brushes from a powerful electric machines [11, 14]. The discharger K-2 is triggered by a starting voltage pulse applied from the IU to the K-1 discharger.

Measurement of the ATPs of formed *A*-, *D*-, *B*-, *C*-, and *C**- components of artificial lightning current is carried out simultaneously with the help of one special high-current shunt (S) of the type ШК-300, which passed the state metrological certification [11, 15]. The GCL of the УИТОМ-1 type is equipped with several such measuring shunts having different S_i conversion coefficients. Thus, to measure ATPs of the *A*- and *D*-components of the artificial lightning current, shunts with these coefficients approximately equal to $S_{iA} \approx 11.26 \cdot 10^3$ A/V and $S_{iA} \approx 25 \cdot 10^3$ A/V are used. When measuring ATPs of *B*-, *C*-, and *C**- components of artificial lightning current, the same shunts are used, but with the conversion coefficients of $S_{iC} \approx 5.64 \cdot 10^3$ A/V and $S_{iC} \approx 12.5 \cdot 10^3$ A/V.

Fig. 3, 4 show typical oscillograms of the pulsed *A*- and long-term *C*- components of the current of artificial lightning with normalized ATPs recorded in high-current discharge circuits of generators PCG-*A* and PCG-*C* of high-power GCL of the УИТОМ-1 type using the above-mentioned measuring shunts and digital storage oscilloscopes series Tektronix TDS 1012, located far from this GCL in the buried measuring bin.

Note that when obtaining the current oscillograms shown in Fig. 3, 4, the charging voltage of the capacitors in the high-power high-voltage generator PSG-*A* was approximately $U_{3A} \approx -29.7$ kV, and in the powerful high-voltage generator PCG-*C* − $U_{3C} \approx -4$ kV. The lumped active-inductive load in this experimental case had the following electrical parameters: an active resistance of about 0.1 Ω, and an inductance of about 1 µH [10].
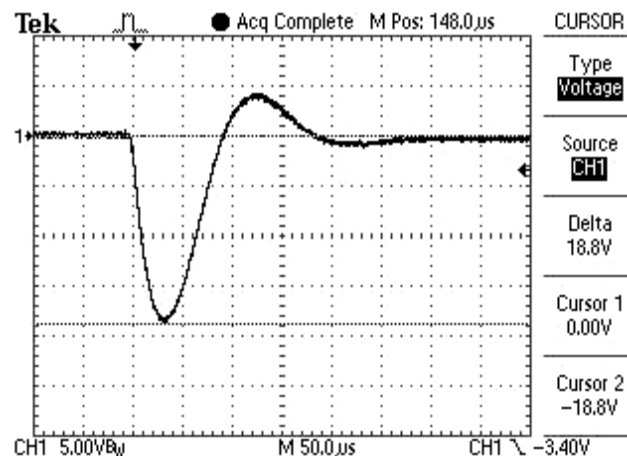

Fig. 3. Oscillogram of the pulsed *A*- component of the artificial lightning current with normalized ATPs in the high-current discharge circuit of the high-voltage generator PSG-*A* of the powerful domestic GCL of the УИТОМ-1 type ($U_{3A} \approx -29.7$ kV; $I_{mA} \approx -212$ kA; $J_{aA} \approx 2.09 \cdot 10^6$ J/Ω; $\tau_f \approx 32$ µs; $\tau_p \approx 500$ µs, vertical scale −56.3 kA/division, horizontal scale – 50 µs/division)
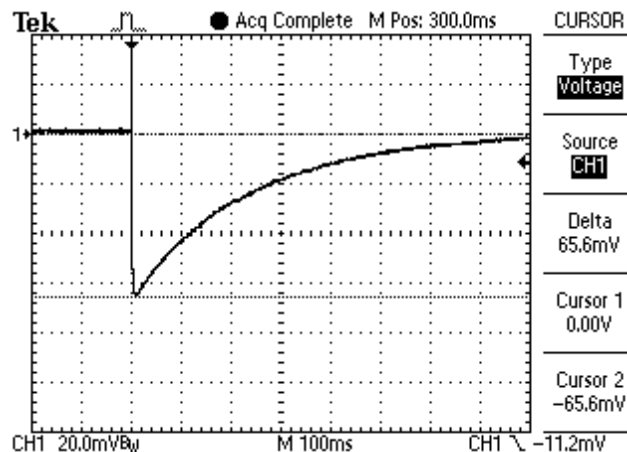

Fig. 4. Oscillogram of the long-term *C*- component of the artificial lightning current with normalized ATPs in the high-current discharge circuit of the high-voltage generator PCG-*C** of the powerful GCL of the УИТОМ-1 type ($U_{3C} \approx -4$ kV; $I_{mC} \approx -738$ A; $q_{0C} \approx -182$ C; $\tau_f \approx 9$ ms; $\tau_p \approx 1000$ ms, vertical scale – 225 A/division, horizontal scale – 100 ms/division)

2.1. Some examples and results of full-scale testing of technical facilities on a powerful GCL type УИТОМ-1. Fig. 5, 6 show the results of direct action on the experimental model of the receiving and transmitting antenna of the domestic production aircraft of the pulsed *A*- component of the artificial lightning current, normalized by [7, 8], ATPs of which corresponded to the data shown in Fig. 3 ($I_{mA} \approx -212$ kA; $J_{aA} \approx 2.09 \cdot 10^6$ J/Ω; $\tau_f \approx 32$ µs; $\tau_p \approx 500$ µs).

From the experimental data of Fig. 5, 6 it follows that the experimental model of the receiving and transmitting antenna of aeronautical engineering of full-scale tests, developed and created without taking into account the requirements for lightning protection, according to the normative documents of the USA SAE ARP 5416: 2013 [7] and SAE ARP 5416: 2013 [8] could not stand: it was destroyed and is disabled [10].

Fig. 7 shows the results of direct simultaneous action in high-current discharge circuits of GCL type УИТОМ-1 on a prototype sheet sample of roofing of a technical structure made of 12X18H10T stainless steel with a thickness of 1 mm normalized by [7, 8], first of the pulsed A- component of artificial lightning current ($I_{mA}≈-192$ kA; $J_{aA}≈1.9·10^6$ J/Ω; $τ_f≈34$ μs; $τ_p≈500$ μs) and immediately behind it a long-term C- component of the current of the simulated lightning discharge ($I_{mC}≈-804$ A; $q_{0C}≈-165$ C; $τ_f≈9$ ms; $τ_p≈448$ ms).
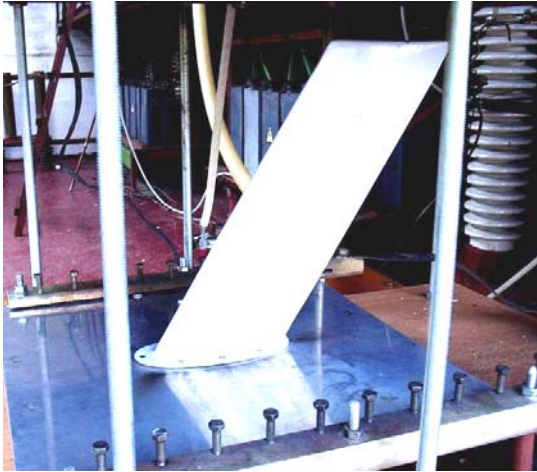

Fig. 5. External view of the experimental model of the aerial receiving and transmitting antenna prior to direct impact on it in the high-current discharge circuit of the PCG-A generator of the powerful GCL of the УИТОМ-1 type of the pulsed A- component of the artificial lightning current with normalized [7, 8] ATPs [10]
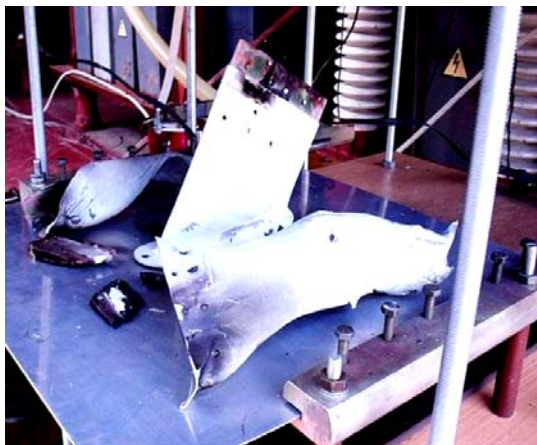

Fig. 6. External view of the experimental model of the aerial receiving and transmitting antenna after the direct impact on it in the high-current discharge circuit of the PCG-A generator of the powerful GCL of the УИТОМ-1 type of the pulsed A- component of the artificial lightning current with normalized [7, 8] ATPs [10]

From the data in Fig. 7 it can be seen that at this current loading of the experimental steel sheet specimen, its rounded through melting with a diameter of up to 12 mm occurs due to the electrothermal effect of the long-term C- component of the current of the simulated lightning discharge used in the experiment [16, 17]. Due to the action on the considered experimental specimen made of the mentioned stainless steel of the pulsed A- component of the current of artificial lightning in the round zone with a diameter of up to 58 mm, a surface melting (up to a depth of 50 μm) with characteristic colors of tarnishing occurs [16, 17].
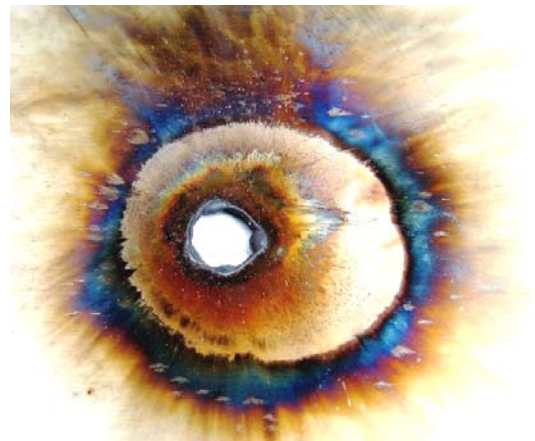

Fig. 7. General view of the affected area in an experimental sheet specimen made of stainless steel grade 12X18H10T of 1 mm thickness from the direct simultaneous action on it of a pulsed A-component ($I_{mA}≈-192$ kA; $J_{aA}≈1.9·10^6$ J/Ω; $τ_f≈34$ μs; $τ_p≈500$ μs) and a long-term C- component of the artificial lightning current ($I_{mC}≈-804$ A; $q_{0C}≈-165$ C; $τ_f≈9$ ms; $τ_p≈448$ ms) formed in high-current discharge circuits of the powerful high-voltage GCL of the УИТОМ-1 type [16]

Fig. 8 shows the results of the damaging action of the pulsed A- component of the current of artificial lightning with the normalized [7, 8] ATPs indicated in Fig. 3 ($I_{mA}≈-212$ kA; $J_{aA}≈2.09·10^6$ J/Ω; $τ_f≈32$ μs; $τ_p≈500$ μs) on the sheet prototype of the composite plating of an airplane of 3 mm thickness and 500×500 mm in plan. In this case, the multilayered composite of the test sample in its composition had fiberglass with an epoxy matrix, carbon fiber with an epoxy phenol matrix and several thin planar metal meshes that act as a reinforcer of the investigated composite material [10, 18]. It can be seen that this sample does not withstand the given effect of the plasma channel of artificial lightning sample does not withstand.

Fig. 8. General view of the damage zone with a diameter of up to 100 mm with a through burn in an experimental sheet specimen of 3 mm thickness of the composite plating of an aircraft tested in the high-current circuit of the powerful GCL of the УИТОМ-1 type, at a direct action on it of normalized by [7, 8] pulsed A- components of artificial lightning current [10]

3. Generator of current of artificial lightning of the type ГТМ-10/350. In 2014, a unique powerful high-voltage high-current generator of the current of a lightning short-term shock of the type ГТМ-10/350 [19] was developed at the experimental site of the Scientific-&-Research Planning-&-Design Institute «Molniya» of the NTU «KhPI», indicated in section 2, where field tests can be performed for the ground objects of industrial power engineering for lightning resistibility in accordance with stringent requirements [9, 12]. A general view of this GCL is shown in Fig. 9, and Fig. 10 shows its principal electric circuit diagram. It can be seen that the composition of this GCL includes four powerful high-voltage pulsed current generators: PCG-1, PCG-2, PCG-3 and PCG-4. The PCG-1 − PCG-3 generators are equipped with high-voltage pulse capacitors of the type ИК-50-3 (rated voltage ±50 kV, nominal capacitance 3 μF), and the PCG-4 generator with high-voltage pulse capacitors of the ИМ2-5-140 type (rated voltage ±5 kV, nominal capacity 140 μF) [19]. In the generators PCG-1 − PCG-3, their capacitors (correspondingly in the amount of 16, 44 and 111 pcs.) are connected in parallel to a rated voltage of ±50 kV, and in the generator PCG-4, the capacitors (288 pcs.) are in series-parallel (by two series-connected capacitors in each of the 144 parallel sections) to a rated voltage of ±10 kV. In this regard, the nominal energy capacitance for these generators is for: PCG-1 – 60 kJ; PCG-2 – 165 kJ; PCG-3 – 416 kJ; PCG-4 – 504 kJ. As a result, the total nominal power capacitance of a powerful generator of artificial lightning current type ГТМ -10/350 is approximately equal to 1.15 MJ [19]. The lumped capacitances $C1 − C4$ for the PCG-1 − PCG-4 generators are 48, 132, 333 and 10080 μF, respectively (see Fig. 10). The intrinsic active resistances $R1 − R4$ of low-resistance discharge circuits of these generators are approximately equal to 375, 136, 57 and 83 mΩ, respectively. The intrinsic inductances $L1 − L4$ of the low-inductance discharge circuits of the mentioned PCG-1 − PCG-4 generators are approximately 1, 1.3, 2.5 and 1.5 μH, respectively. The forming inductances $L31$ and $L41$ (see Fig. 10) are chosen to be approximately equal to 40 and 7 μH.

Fig. 9. General view of a powerful high-current generator of artificial lightning current type ГТМ-10/350 (in the foreground there is its working table with placed on top of it a controlled high-voltage three-electrode air switch with graphite electrodes for voltage of ±50 kV and pulsed aperiodic lightning current of amplitude up to ±220 kA and the tested sample of cable-conductor products, and in the background – the electrical engineering elements of the charge-discharge circuits of its separate high-voltage pulsed current generators PCG-1, PCG-2, PCG-3 and PCG-4) [19]
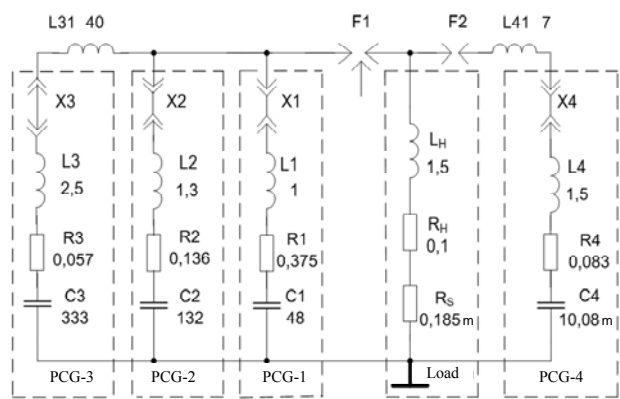

Fig. 10. Principal replacing electric circuit of high-current discharge circuits of four separate high-voltage generators PCG-1 – PCG-4 in the composition of a powerful current pulse generator 10/350 μs of artificial lightning of the type ГТМ-10/350 ($X1−X4$ − current-carrying jumpers of discharge circuits of generators PCG-1 − PCG-4) [19]

The active-inductive load in the circuit in Fig. 10 contains a lumped active resistance $R_H≈0.1$ Ω and a concentrated inductance $L_H≈1.5$ μH. In sequence with the electrical load parameters, the intrinsic resistance R_S of the ШК-300 measuring shunt, numerically equal to about 0.185 mΩ [11, 15], is connected. Such a value of R_S practically does not influence the electromagnetic processes in the discharge circuits of the GCL and the electrical circuits of the tested ground object.

The switching of the high-current discharge circuits of the PCG-1 − PCG-3 generators as part of a powerful current generator of a short-time thunder-storm strike type ГТM-10/350 is performed by a three-electrode air controlled switch with graphite electrodes (Fig. 11) specially designed for this purpose [19].

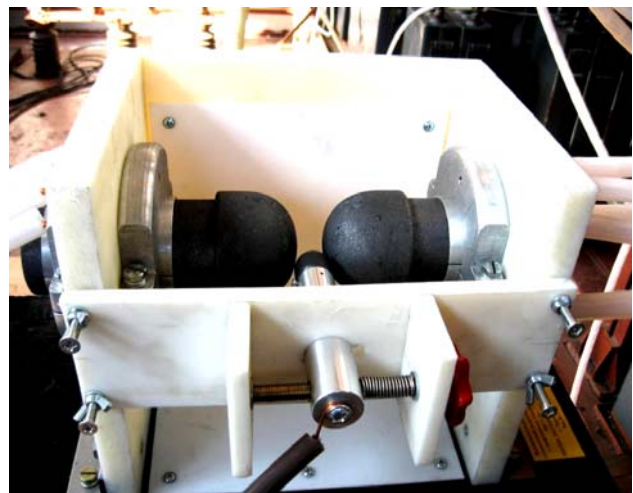Fig. 11. External view of the high-voltage three-electrode air controlled switch $F1$ with graphite electrodes at a rated DC voltage of ±50 kV and a pulsed current of artificial lightning of the time shape of 10/350 μs with amplitude up to ±220 kA in the GCL circuit [19]

As for the switching of the discharge circuit of the PCG-4 generator, it is performed using a two-electrode $F2$ air switch with graphite electrodes for a rated voltage of ±10 kV and a pulse current of up to ±100 kA. The switch $F2$ is started by the pulse overvoltage that occurs

on the electrical load when the switch $F1$ is activated and the pulse discharge current from the PCG-1 − PCG-3 generators begins to flow in it.

Fig. 12 shows the oscillogram of obtained in the discharge circuit of the ГТМ-10/350 generator with a low-resistance active-inductive load ($R_\text{H} \approx 0.1$ Ω; $L_\text{H} \approx 1.5$ μH) aperiodic current pulse of artificial lightning with normalized [9, 12] ATPs.
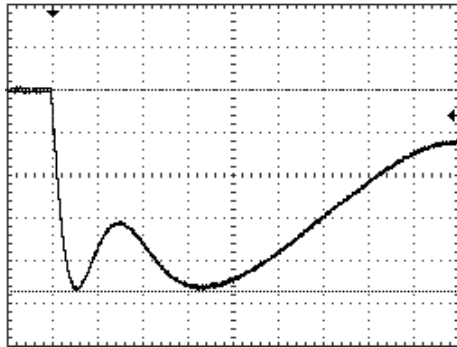

Fig. 12. Oscillogram of an aperiodic current pulse of the time shape of 15/340 μs in the high-current discharge circuit of the powerful high-voltage generator of artificial lightning current type ГТМ-10/350 with a low-resistance RL-load ($U_{\text{C1-3}} \approx -15$ kV; $U_{\text{C4}} \approx -2.25$ kV; $I_m \approx -106$ kA; $J_a \approx 3.03 \cdot 10^6$ J/Ω; $q_0 \approx 52.2$ C ; $\tau_f \approx 15$ μs; $\tau_p \approx 340$ μs; $R_\text{H} \approx 0.1$ Ω; $L_\text{H} \approx 1.5$ μH; vertical scale - 22.52 kA/division; horizontal scale -50 μs/division) [19]

The charging voltage $U_{\text{C1-3}}$ of the negative polarity of all the capacitors for the PCG-1 − PCG-3 generators in this case was about 15 kV, and the charging voltage U_{C4} of the same polarity of the individual capacitors for the PCG-4 generator was about 2.25 kV.

3.1. Some examples and results of full-scale tests of energy facilities on a powerful generator of artificial lightning current type ГТМ-10/350. Fig. 13 shows the working table of the generator type ГТМ-10/350 with the prepared according to the requirements [9, 12] for the tests on the electrothermal resistivity to the direct action of the artificial lightning current pulse 10/350 μs the pilot sample of the radio frequency coaxial cable of the РК 50-7-11 type with the belt polyethylene insulation having a split copper core of section $S \approx 3.2$ mm^2.
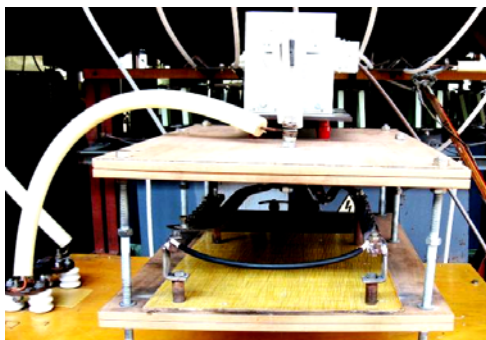

Fig. 13. External view of the working table of the generator of artificial lightning current type ГТМ-10/350 with fixed on its steel electrodes a splintered round copper core of 3.2 mm^2 cross section and of 0.5 m length of the radio frequency coaxial cable of РК 50-7-11 type with solid polyethylene insulation and its «drowned» external copper braiding before the action of an aperiodic current pulse of 17/310 μs of a lightning discharge by an amplitude of ~82.9 кА [20]

This cable could not stand the direct action in a high-current discharge circuit of a powerful generator of the type ГТМ-10/350 of the aperiodic current pulse 17/310 μs ($I_m \approx 82.9$ kA; $J_a \approx 1.59 \cdot 10^6$ J/Ω; $q_0 \approx 36.3$ C; $\tau_f \approx 17$ μs; $\tau_p \approx 310$ μs) on its copper core. At a current density in the copper core of about $\delta_m \approx I_m/S \approx 25.9$ кА/mm^2, an electric explosion (EE) occurred, which led to the destruction of the cable and its failure.

Fig. 14 shows a visual demonstration of the EE phenomenon of a continuous aluminum core with a cross section of 6 mm^2 of the network wire АППВнг2×6 with polyvinyl chloride insulation, which occurred at supply to it in the discharge circuit of the powerful generator of the type ГТМ-10/350 an aperiodic current pulse of the time shape of 17/265 μs of positive polarity ($I_m \approx 83,8$ kA; $J_a \approx 1.41 \cdot 10^6$ J/Ω; $q_0 \approx 31.7$ C; $\tau_f \approx 17$ μs; $\tau_p \approx 265$ μs) [20]. We point out that the current density in the aluminum core of the wire was then $\delta_m \approx I_m/S \approx 14$ кА/mm^2.
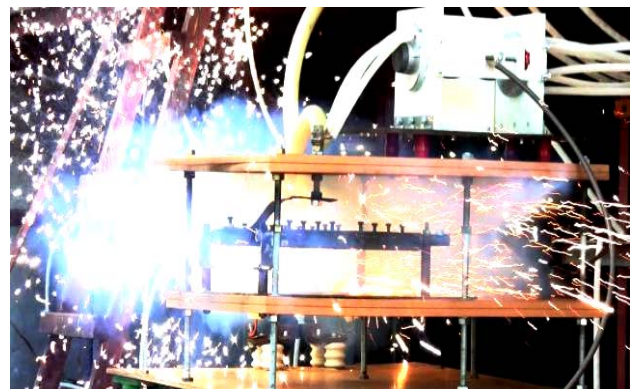

Fig. 14. General view of the EE phenomenon of a solid round aluminum core of 6 mm^2 cross-section of the АППВнг2×6 network cable with polyvinyl chloride insulation in the high-current discharge circuit of the powerful high-voltage generator type ГТМ-10/350 ($U_{\text{C1-3}} \approx 15$ kV; $U_{\text{C4}} \approx 2.1$ kV; $I_m \approx 83.8$ kV; $J_a \approx 1.41 \cdot 10^6$ J/Ω; $q_0 \approx 31.7$ C; $\tau_f \approx 17$ μs; $\tau_p \approx 265$ μs) [20]

Fig. 15 shows the oscillogram of this test pulse of the current of a short-term lightning strike.
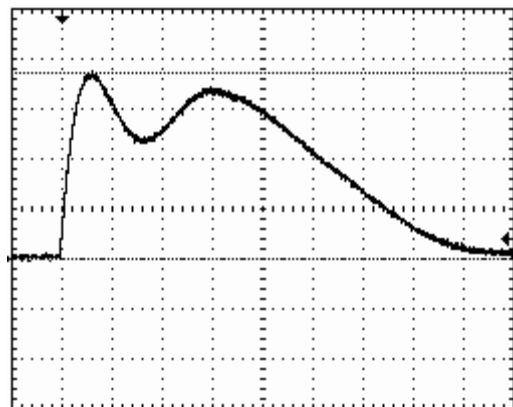
Fig. 15. Oscillogram of the aperiodic current pulse of 17/265 μs of artificial lightning in the high-current discharge circuit of the powerful high-voltage generator ГТМ-10/350 at EE of a solid round aluminum core with cross section of 6 mm^2 and length of 0,5 m of a network wire АППВнг2×6 with polyvinyl chloride insulation ($U_{\text{C1-3}} \approx 15$ kV; $U_{\text{C4}} \approx 2.1$ kV; $I_m \approx 83.8$ kV; $J_a \approx 1.41 \cdot 10^6$ J/Ω; $q_0 \approx 31.7$ C; $\tau_f \approx 17$ μs; $\tau_p \approx 265$ μs; vertical scale – 22.52 kA/division; horizontal scale – 50 μs/division) [20]

From a comparison of the data in Fig. 12, 15 it follows that the electrophysical processes in the elements of the tested object that proceed during the tests on the lightning resistibility according to the requirements of [9, 12] can substantially deform the first of all the falling part of the current pulse of artificial lightning. This is particularly evident in the EE of current-carrying elements of the object, which interrupt the current flow of the simulated lightning discharge current from the generator of the type ГТМ-10/350.

Conclusions.

1. Analysis of the current state in Ukraine of tooling for full-scale testing of industrial power engineering facilities, aircraft and rocket and space equipment for lightning resistibility shows that on domestic high-voltage high-current electrical equipment, including unique powerful generators such as УИТОМ-1 and ГТМ-10/350, developed and created at the Scientific-&-Research Planning-&-Design Institute «Molniya» of the NTU «KhPI» certification electromagnetic tests of the elements and systems of indicated objects on a direct or indirect effect of pulsed current of artificial lightning, meeting the requirements of the current US regulatory documents SAE ARP 5412: 2013, SAE ARP 5416: 2013 and the International Standard IEC 62305-1: 2010, can be conducted in the field.

2. The presented results and the world experience of the damaging effect on the technical and biological objects of linear lightning that develops and flows in the air troposphere of our planet unequivocally point to the necessity of carrying out the considered full-scale tests of structural elements and engineering networks of aircrafts and ground power facilities for complex resistibility to pulse lightning current.

3. Real actual tests for lightning resistibility and fire safety of objects of domestic and foreign aviation equipment (for example, onboard receiving and transmitting radio engineering devices, metal and composite elements of the frames of the aircrafts of the Antonov and Boeing) conducted in recent years on powerful generators of the УИТОМ-1 and ГТМ-10/350 types and industrial power engineering (for example, prototypes of multi-layer panels with an outer layer of thin sheet stainless steel of an expensive large-size protective containment of the 4th power unit of the Chernobyl Nuclear Power Plant) testify to the full compliance of the technical characteristics of domestic generators of artificial lightning current with the high requirements of the normative documents in force in the leading countries of the world.

REFERENCES

1. Baranov M.I. An anthology of the distinguished achievements in science and technique. Part 42: Electronics: retrospective view, successes and prospects of its development. *Electrical engineering & electromechanics*, 2018, no.1, pp. 3-16. **doi: 10.20998/2074-272X.2018.1.01.**
2. Uman M.A. Natural and artificially-initiated lightning and lightning test standards. *Proceedings of the IEEE*, 1988, vol.76, no.12, pp. 1548-1565. **doi: 10.1109/5.16349.**
3. Kuzhekin I.P., Larionov V.P., Prohorov E.N. *Molnija i molniezashchita* [Lightning and protection from lightning]. Moscow, Znak Publ., 2003. 330 p. (Rus).

4. Dyakov A.F., Kuzhekin I.P., Maksimov B.K., *Temnikov A.G. Elektromahnitnaya sovmestimost' i molniezashchita v elektroenergetike* [Electromagnetic compatibility and lightning protection in the power]. Moscow, MEI Publishing House, 2009. 455 p. (Rus).
5. Bortnik I.M., Beloglovskiy A.A., Vereshchagin I.P., Vershinin Yu.N., Kalinin A.V., Kuchinskiy G.S., Larionov V.P., Monastyrskiy A.E., Orlov A.V., Temnikov A.G., Pintal' Yu.S., Sergeev Yu.G., Sokolova M.V. *Elekrophizicheskie osnovy tehniki vysokih naprjazhenij* [Electrophysics bases of technique of high voltage]. Moscow, Publishing house of MEI, 2010. 704 p. (Rus).
6. Baranov M.I. New hypothesis and electrophysics nature of additional mechanisms of origin, accumulation and division of electric charges in the atmospheric clouds of Earth. *Electrical engineering & electromechanics*, 2018, no.1, pp. 46-53. **doi: 10.20998/2074-272X.2018.1.07.**
7. SAE ARP 5412: 2013. Aircraft Lightning Environment and Ralated Test Waveforms. SAE Aerospace. USA, 2013. − pp. 1-56.
8. SAE ARP 5416: 2013. Aircraft Lightning Test Methods. SAE Aerospace. USA, 2013. − pp. 1-145.
9. IEC 62305-1: 2010 «Protection against lightning. Part 1: General principles». Geneva, IEC Publ., 2010.
10. Baranov M.I. *Izbrannye voprosy elektrofiziki. Monografiya v 3kh tomakh. Tom 2, Kn. 2: Teoriia elektrofizicheskikh effektov i zadach* [Selected topics of Electrophysics. Monograph in 3 Vols. Vol.2, Book 2. A theory of electrophysical effects and tasks]. Kharkiv, Tochka Publ., 2010. 407 p. (Rus).
11. Baranov M.I., Koliushko G.M., Kravchenko V.I., Nedzel'skii O.S., Dnyshchenko V.N. A Current Generator of the Artificial Lightning for Full-Scale Tests of Engineering Objects. *Instruments and Experimental Technique*, 2008, no.3, pp. 401-405. **doi: 10.1134/s0020441208030123.**
12. *GOST R MEK 62305-1-2010. Menedzhment riska. Zashhita ot molnii. Chast' 1: Obshhie principy* [GOST R IEC 62305-1-2010. Risk management. Protection from lightning. Part 1: General principles]. Moscow, Standartinform Publ., 2011, 46 p. (Rus).
13. Baranov M.I. Improvement of resistance protection of high-voltage capacitors of powerful capacitive energy storage systems from emergency overcurrent. *Russian Electrical Engineering*, 2017, vol.88, no.1, pp. 19-22. **doi: 10.3103/S1068371217010060.**
14. Baranov M.I., Koliushko G.M., Kravchenko V.I., Nedzel'skii O.S., Nosenko M.A. High-voltage high-current air-filled spark gaps of an artificial-lightning-current generator. *Instruments and Experimental Techniques*, 2008, vol.51, no.6, pp. 833-837. **doi: 10.1134/s0020441208060109.**
15. Baranov M.I., Kniazev V.V., Rudakov S.V. A coaxial disk shunt for measurement in the high-current circuit of high-voltage generator of storm discharges of pulses of current of artificial lightning with the integral of action up to $15 \cdot 10^6$ J/Ohm. *Electrical engineering & electromechanics*, 2017, no.5, pp. 45-50. **doi: 10.20998/2074-272X.2017.5.07.**
16. Baranov M.I., Kniaziev V.V., Kravchenko V.I., Rudakov S.V. Results of calculation-experimental investigations of electro-thermal resistibility of sheet steel samples to action of rationed components of pulsed current of artificial lighting. *Electrical engineering & electromechanics*, 2016, no.3, pp. 40-49. **doi: 10.20998/2074-272X.2016.3.07.**
17. Baranov M.I., Nosenko M.A. Influence of the thermal action of artificially-initiated lightning current on specimens of the metal skin of an aircraft. *Journal of Engineering Physics and Thermophysics*, 2009, vol.82, no.5, pp. 978-987. **doi: 10.1007/S10891-009-0272-z.**
18. Baranov M.I. An anthology of the distinguished achievements in science and technique. Part 41: Composite materials: their classification, technologies of making, properties

and application domains in modern technique. *Electrical engineering & electromechanics*, 2017, no.6, pp. 3-13. **doi: 10.20998/2074-272X.2017.6.01.**

19. Baranov M.I., Koliushko G.M., Kravchenko V.I., Rudakov S.V. A generator aperiodic current pulses of artificial lightning with a rationed temporal form of 10/350 μs with an amplitude of ± (100-200) kA. *Instruments and Experimental Techniques*, 2015, vol.58, no.6, pp. 745-750. **doi: 10.1134/S0020441215060032.**

20. Baranov M.I., Rudakov S.V. Electrothermal action of the pulse of the current of a short artificial-lightning stroke on test specimens of wires and cables of electric power objects. *Journal of Engineering Physics and Thermophysics*, 2018, vol.91, no.2, pp. 544-555. **doi: 10.1007/s10891-018-1775-2.**

M.I. Baranov[1], Doctor of Technical Science, Chief Researcher,
S.G. Buriakovskyi[1], Doctor of Technical Science,
S.V. Rudakov[2], Candidate of Technical Science, Associate Professor,
[1] Scientific-&-Research Planning-&-Design Institute «Molniya», National Technical University «Kharkiv Polytechnic Institute», 47, Shevchenko Str., Kharkiv, 61013, Ukraine,
phone +380 57 7076841,
e-mail: baranovmi@kpi.kharkov.ua, sergbyr@i.ua
[2] National University of Civil Protection of Ukraine, 94, Chernyshevska Str., Kharkiv, 61023, Ukraine,
phone +38 057 7073438,
e-mail: serg_73@i.ua

G.V. Bezprozvannych, I.A. Mirchuk

CORRELATION BETWEEN ELECTRICAL AND MECHANICAL CHARACTERISTICS OF CABLES WITH RADIATION-MODIFIED INSULATION ON THE BASIS OF A HALOGEN-FREE POLYMER COMPOSITION

Introduction. The high saturation of the cable routes of nuclear and thermal stations, wind parks and solar power plants, on-board systems imposes stringent requirements in the field of fire safety of cables, which makes it necessary to use highly flame retardant halogen-free compositions. The introduction of flame retardants causes the mandatory modification (crosslinking) of the polymer matrix. Purpose. Determination of the optimal radiation dose based on the correlation between the mechanical and electrical characteristics of a radiation-modified halogen-free ethylene vinyl acetate copolymer with high-strength flame retardant insulation cables. Methodology. Mechanical and electrical tests of samples of radiation-modified cables with a copper conductor cross section of 1.0 mm^2 and a halogen-free filled insulation based on an EVA copolymer with a thickness of 0.7 mm have been performed. Results. A strong correlation is established between the elongation at break and the tensile strength, between the insulation resistance and the breakdown voltage. It is shown that at the optimum value of the irradiation coefficient in the range from 7 to 5, the insulation resistance increases more than twice, and the breakdown voltage at the direct current is increased by 1.3 times. The elongation at break is within the allowed values. References 12, figures 3.
Key words: **halogen-free composition, radiation modification, irradiation coefficient, mechanical and electrical characteristics, correlation coefficient.**

Исследовано влияние коэффициента облучения ускоренных электронов с энергией 0,5 МэВ на механические и электрические характеристики кабельной высоконаполненной антипиренами изоляции из не распространяющей горение безгалогенной композиции на основе сополимера етиленвинилацетата. Установлена сильная корреляционная связь между относительным удлинением при разрыве и прочностью при растяжении, между сопротивлением изоляции и пробивным напряжением. Показано, что при оптимальном значении коэффициента облучения в диапазоне от 7 до 5, сопротивление изоляции возрастает более чем в два раза, а пробивное напряжение на постоянном токе – в 1,3 раза. Относительное удлинение при разрыве остается в пределах допустимых значений. Библ. 12, рис. 3.
Ключевые слова: **безгалогенная композиция, радиационное модифицирование, коэффициент облучения, механические и электрические характеристики, коэффициент корреляции.**

Introduction. High saturation of the cable routes of nuclear and thermal stations, wind parks and solar power stations, on-board systems makes stringent requirements in the field of fire safety of cables [1]. All this necessitates the use of new class materials, such as halogen-free compositions, for the insulation and sheath of cables. The term «halogen-free composition» is not a strict designation of the polymer from a technical point of view, such as polyethylene or polyvinyl chloride. However, this term is used in the cable industry and in fact is a separate class of materials [1]. Halogen-free compositions are polymeric materials that do not contain or contain very little (less than 0.5 % by weight) halogens, and which do not spread combustion under the influence of fire. The absence of halogens in insulation, filling and sheathing of cables is one of the most important characteristics of their fire safety. To ensure high resistance to the spread of combustion, the polymer is filled with a large amount (up to 70 % by weight) of inorganic flame retardants (mainly aluminum or magnesium hydroxides). However, the introduction of fire retardants necessitates a mandatory modification (crosslinking) of the polymer matrix, which leads to the creation of a spatial structure. The most preferred method of crosslinking is radiation modification [2-4], in which the probability of formation of low-molecular products, including moisture, is significantly lower in comparison with the chemical method [5].

Sources of ionizing radiation for modifying the polymer insulation of cables and wires with conductor cross-section up to 240 mm^2 are electron accelerators with energies (0.3-5) MeV and power up to hundreds of kW [6, 7].

The required dose for polyethylene crosslinking is 20-40 Mrad [5, 8-11]. For fluoropolymers – from (0.5-2) to (20-30) Mrad [5]. Crosslinking of polymers allows to significantly increase their mechanical strength, heat resistance, resistance to the action of chemically active substances, cracking [8-11].

The most interesting as halogen-free compositions are compositions based on copolymers of ethylene (ethylene-vinyl acetate, ethylene-acrylate, ethylene-propylene, etc.) with the introduction of flame retardants and other additives in the polymer matrix that increase the resistance of the material to the spread of combustion, as well as better dispersion of fillers in the polymer [12].

The presence in the macromolecule of ethylene units, as well as double bonds, provides a polymer composition based on an ethylene-vinyl acetate copolymer, as well as polyethylene, crosslinking under the influence of ionizing radiation. The dose of irradiation is determined at the stage of investigation of the cable composition and cable development.

The goal of the paper is determination of the optimal radiation dose based on the correlation between the mechanical and electrical characteristics of a radiation-modified halogen-free ethylene vinyl acetate copolymer high-strength flame retardant cable insulation.

Technological parameters of radiation modification. When irradiated as a result of the

ionization of molecules and the disruption of C-H bonds, free macroradicals and atomic hydrogen are formed in the polymer. As a result of further recombination of macroradicals and the formation of crosslinks between macromolecules, the polymer acquires a three-dimensional (spatial) structure. However, at irradiation, not only the process of crosslinking of macromolecules proceeds, but also the process of their destruction, caused by the rupture of valence bonds in the macromolecule. The possibility of carrying out the radiation crosslinking of a polymer is determined by the ratio of the rates of the «crosslinkage – destruction» processes and depends on which of these processes prevails.

The technological parameters of radiation modification and, as a consequence, the dose of irradiation, have a significant influence on the ratio of the processes of crosslinking and degradation.

At a fixed voltage of the electron accelerator, the technological dose of irradiation is directly proportional to the current of the electron beam and inversely proportional to the transmission speed of the cable under this beam [5]: $D = \dfrac{120 \cdot I \cdot N}{L \, V}$, Mrad, where I is the electron beam current (mA), N is the number of wire passes under the electron beam, L is the length of the beam scan perpendicular to the direction of the workpiece pulling, V is the velocity of the passage under the electron beam (m/min).

In practice, at the radiation modification of insulation and cable sheaths, the irradiation factor (K) is used, which is controlled by the change in the cable passage velocity under the electron beam at the electron beam current unchanged: the higher K, the less the irradiation of the material [5]. The radiation factor is the result of a compromise between the mechanical and electrical properties of the insulation and the technical requirements imposed on the finished cable.

To ensure uniform crosslinking over the entire volume of insulation, the stability of the accelerator operation is a prerequisite, which makes the parameters of the electron beam constant.

Test samples and parameters of irradiation. On an industrial accelerator of charged particles ЕЛВ-1 radiation modification of samples of insulated wire 5 m long with copper cores of 1.0 mm^2 cross section has been carried out (Fig. 1). Insulation of 0.7 mm thickness is halogen-free composition based on ethylene-vinyl acetate copolymer, highly filled to 70 % by mass with flame retardants. The wire samples are irradiated with different irradiation factors K: 17; 15; 13; 11; 10; 9; 8; 7; 6; 5 and 4 at accelerated electron energy of 0.5 MeV. One sample is control one (not exposed to radiation). The electron beam current is 10 mA. The number of wire passes under the electron beam is 80.

Correlation between the electrical and mechanical characteristics of radiation-crosslinked insulation. In the initial state (before irradiation) and after exposure, mechanical and electrical tests of wire samples were carried out.

Fig. 2 shows the correlation dependences of the mechanical (Fig. 2,*a*) and electrical (Fig. 2,*b*)

characteristics on the irradiation factor: mechanical elongation at break $\Delta\varepsilon$ and the tensile strength σ (Fig. 2,*a*); insulation resistance R_{ins} and breakdown voltage U_{br} (Fig. 2,*b*), respectively.

Fig. 1. The layout of the electron accelerator for irradiating insulation of cables and wires
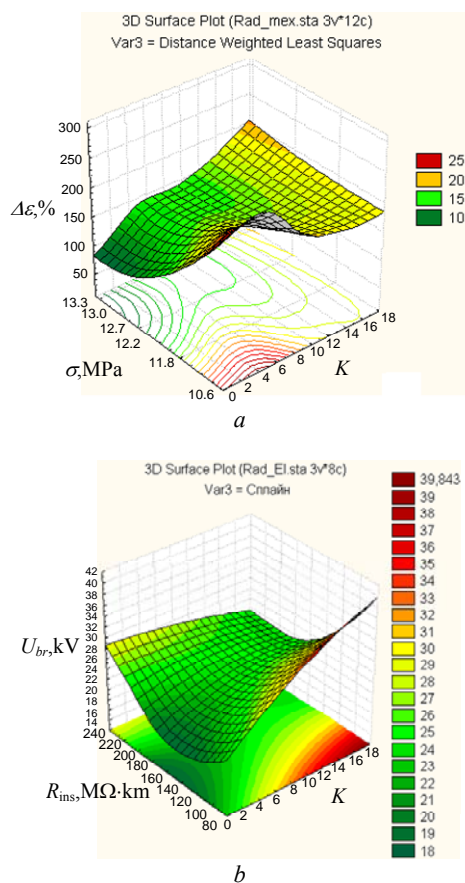

a

b

Fig. 2. To establish the correlation dependence between the mechanical (*a*) and electrical (*b*) characteristics of radiation-crosslinked insulation

A strong correlation is observed for mechanical and electrical characteristics. Here, between the relative elongation at break and the tensile strength this is negative; between the resistance of insulation and breakdown voltage this is positive. The correlation coefficients are 0.9189 and 0.8045, respectively. At decrease in the irradiation coefficient, i.e. with increasing radiation dose, tensile strength, insulation resistance and breakdown voltage at constant current increase to a

certain value, after which they begin to decrease; the relative elongation at mechanical break decreases monotonically.
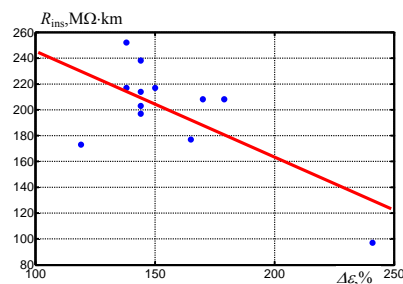
For mechanical characteristics, the correlation is more pronounced, which is also confirmed by the Spearman rank correlation analysis: a significance test for 100 % of the data at a *p*-level of 0.001496. For electrical characteristics, the significance test is only for 25 % of the measured values at a *p*-level of 0.617075.

Such a difference is due to the sample size of the samples measurements for each dose of radiation: the mechanical characteristics are averaged for 5 measurements, electrical – for the 1st one.
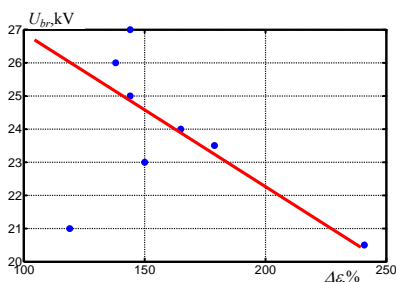
Between the mechanical and electrical characteristics there is also a correlation relationship (Fig. 3).
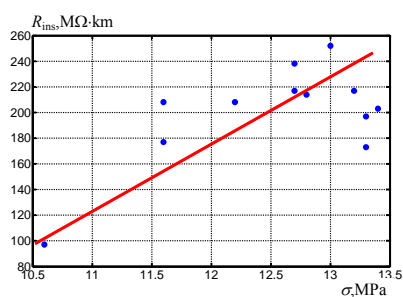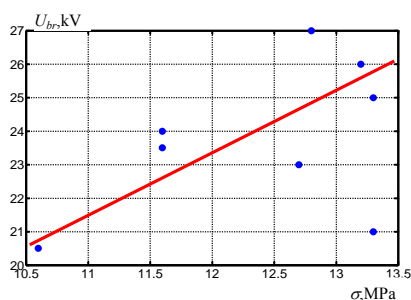

a

b

c

d

Fig. 3. Correlation dependence between mechanical and electrical characteristics of radiation-crosslinked insulation

The correlation coefficient between the insulation resistance and the tensile strength is positive and equal to 0.6253 (Fig. 3,*a*), between the insulation resistance and the relative elongation (Fig. 3,*b*) is negative and equal to **-0.7105**. The correlation between the breakdown voltage and the relative elongation (Fig. 3,*c*), between the breakdown voltage and the tensile strength (Fig. 3,*d*) is weak: the Pearson pair correlation coefficients are **–0.4980** and **0.4964**, respectively.

Considering that the resistance to radiation of materials is determined by the radiation index (RI) according to [2] as the logarithm of the absorbed dose in Grays, at which the relative elongation decreases by no more than 50 % (twice) relative to the initial value, the optimum value of the irradiation coefficient lies in the range from 7 to 5. In this range of values of the irradiation coefficient, the maximum value of tensile strength (see Fig. 2), insulation resistance and breakdown voltage at constant current is observed (see Fig. 3). The insulation resistance increases more than twofold, the breakdown voltage at constant current is 1.3 times that of the unirradiated state, which is associated with an increase in the homogeneity and orderliness of the molecular structure of the polymer after crosslinking. With a decrease in the irradiation coefficient, i.e. an increase in the irradiation dose, a trend is observed toward a reduction in electrical characteristics due to the accumulation in the polymer of charge carriers and free radicals formed during irradiation.

Conclusions.

The influence of the coefficient of irradiation of accelerated electrons with an energy of 0.5 MeV on the mechanical and electrical characteristics of a cable high-fire-retardant insulation made of a non-halogen composition based on an ethylene-vinyl acetate copolymer is investigated and a strong correlation relationship between the relative elongation at mechanical break and tensile strength, between insulation resistance and breakdown voltage is determined.

For the first time, the optimal range of the insulation coefficient of insulation of cables, ranging from 5 to 7, has been determined, with which the electrical insulation resistance increases more than twice, the breakdown voltage at constant current increases by 1.3 times, and the elongation at mechanical break remains within the permissible values.

REFERENCES
1. IEC 60092-359:2014. Electrical Installations In Ships – Part 359: Sheathing Materials For Shipboard Power And Telecommunication Cables By IEC TC/SC 18A. 50 p.
2. Standard IEC 5444-4. Guide for determining the effects of ionizing radiation on insulating materials. Part 4: Classification system for service in radiation environments. 1986. 22 p.
3. Cleland M.R. *High Power Electron Accelerators for Industrial Radiation Processing of Polymers*. Hanser Publ., Munich and Oxford University Press. New York, 1992. 23 p.
4. Studer N. Electron beam crosslinking of insulated wire and cable: Process economics and comparison with other technologies. *International Journal of Radiation Applications and Instrumentation. Part C. Radiation Physics and Chemistry*, 1990, vol.35, no.4–6, pp. 680-686. **doi: 10.1016/1359-0197(90)90296-t.**

5. Finkel E.E., Leschenko S.S., Braginsky R.P. *Radiatsionnaia khimiia i kabel'naia tekhnika* [Radiation chemistry and cable technology]. Moscow, Atomizdat Publ., 1968. 313 p. (Rus).

6. Machi S. Role of radiation processing for sustainable development. *Emerging applications of radiation processing*, 2004, Vienna: IAEA. (IAEA-TECDOC-1386), pp. 5-13.

7. Zimek Z., Przybytniak G., Nowicki A., Mirkowski K., Roman K. Optimization of electron beam crosslinking for cables. *Radiation Physics and Chemistry*, 2014, vol.94, pp. 161-165. **doi: 10.1016/j.radphyschem.2013.07.005.**

8. Bezprozvannych G.V., Naboka B.G., Morozova E.V. Radiating resistance of common commercial cables of internal laying. *Electrical engineering & electromechanics*, 2006, no.3, pp. 82-86. **doi: 10.20998/2074-272X.2006.3.16.** (Rus).

9. Bezprozvannych G.V., Naboka B.G., Morozova E.V. Change in the mechanical properties of materials of structural elements of optical cables under the influence of radiation. *Bulletin of NTU «KhPI»*, 2004, no.7, pp. 28-35. (Rus).

10. Bezprozvannych G.V., Morozova EV, Sokolenko A.N. Effect of ionizing radiation on the capacitance and tangent of the dielectric loss angle of network cables. *Bulletin of NTU «KhPI»*, 2003, no.9, vol.4, pp. 3-8. (Rus).

11. Berejka A.J. Radiation response of industrial materials: Dose-rate and morphology implications. *Nuclear Instruments and Methods in Physics Research Section B: Beam Interactions with Materials and Atoms*, 2007, vol.261, no.1–2, pp. 86-89. **doi: 10.1016/j.nimb.2007.03.097.**

12. IEC 60811-2-1:2001. Common test methods for insulating and sheathing materials of electric and optical cables – Part 2-1: Methods specific to elastomeric compounds – Ozone resistance, hot set and mineral oil immersion tests. – 32 p.

G.V. Bezprozvannych[1], *Doctor of Technical Sciences, Professor,*
I.A. Mirchuk[2], *Postgraduate Student,*
[1] National Technical University «Kharkiv Polytechnic Institute»,
2, Kyrpychova Str., Kharkiv, 61002, Ukraine,
phone +380 57 7076010,
e-mail: bezprozvannych@kpi.kharkov.ua
[2] Private Joint Stock Company «Ukraine Scientific-Research Institute of Cable Industry»,
2-P, Promychlennaya Str., Berdyansk, Zaporozhye Region, 71101, Ukraine,
phone +380 66 8288554,
e-mail: garik710@ukr.net

J. Gerlici, I.O. Shvedchykova, J.A. Romanchenko, I.V. Nikitchenko

DETERMINATION OF THE RATIONAL GEOMETRICAL PARAMETERS OF PLATE TYPE ELEMENTS OF MAGNETIC MATRIX OF THE POLYGRADIENT SEPARATOR

Introduction. Polygradient magnetic separation has wide application in industry and in biomedicine. Working process in polygradient separators takes place in a matrix, magnetic elements of which create magnetic forces sufficient to remove small ferro- and paramagnetic inclusions. Problem. The influence of mutual arrangement of elements on character of distribution of magnetic field is not taken into account during calculation of characteristics of magnetic field in magnetic matrixes. It makes comparative analysis of matrixes of different configurations quite difficult. Fulfillment of comparative analysis of strength characteristics of magnetic fields of multicomponent matrixes of polygradient separators of various configurations requires further researches. Goal. To determine the dependence of the strength characteristics of the polygradient electromagnetic separator on the geometrical parameters of the plate type elements of the multicomponent matrix. Methodology. The finite element method for calculation of power characteristics of separator magnetic field, method of comparative analysis and simple search method for determination of rational geometric parameters of the matrix have been used during the solution of the paper problem. Results. Estimation of entire spectrum of force field in plane of working zones of investigated structures in two-dimensional location for determination of rational variants of polygradient matrixes has been done. The main stages of computational experiment are given. Method of comparative analysis of power characteristics of investigated variants of matrix structures with corresponding characteristics of basic version of separator for determination of rational geometrical variants of polygradient matrixes has been applied. By results of calculations the rational geometric parameters of polygradient matrix has been chosen. The characteristics of power magnetic fields in working gaps of matrixes of polygradient separator have been studied. It made possible to determine the rational structural variants of matrix on basis of parameter of effective area of working zone. Practical value. The results of research can be used in practice of design of electromagnetic separators with polygradient matrixes. References 10, table 1, figures 4.
Key words: **electromagnetic separator, polygradient matrix, inhomogeneity coefficient, working zone, criteria of geometric similarity.**

Осуществлена оценка спектра силового поля в плоскости рабочих зон исследуемых структур полиградиентных матриц электромагнитного сепаратора в двумерной постановке. Приведены основные этапы вычислительного эксперимента. Для решения задачи по определению рациональных вариантов полиградиентных матриц был задействован метод сравнительного анализа силовых характеристик исследуемых вариантов структур матрицы с соответствующими характеристиками базового варианта сепаратора. Произведён выбор рациональных геометрических параметров пластинчатых элементов магнитной матрицы сепаратора по критерию эффективной площади рабочей зоны матрицы. Проведен сравнительный анализ полученных данных с результатами других исследователей. Библ. 10, табл. 1, рис. 4.
Ключевые слова: **электромагнитный сепаратор, полиградиентная матрица, коэффициент неоднородности, рабочая зона, геометрические критерии подобия.**

Introduction. Polygradient magnetic separation has been widely used in industry and in biomedicine. In polygradient separators, the working process takes place in a matrix, whose magnetized elements create magnetic forces sufficient for the removal of small ferro- and paramagnetic inclusions [1, 2].

In the practice of magnetic separation, at calculating the magnetic force F_m acting on the body of the volume V, which is removed, most often they come out of expression [2]

$$F_m = \mu_0 \chi H \text{grad}(H) V , \qquad (1)$$

where H is the magnetic field strength vector in the calculated area free of electric currents; μ_0 is the magnetic constant; χ is the average magnetic susceptibility of the removed body which depends on its shape, the ratio of the size and the magnetic permeability of the substance.

From (1) it can be seen that the direction of the extraction force F_m coincides with the direction of gradient grad(H) of the magnetic field strength H. As a result, the specific force f_m of the magnetic field of the separator is defined as the product of the magnetic field strength H on its gradient grad(H)

$$f_m = F_m /(\mu_0 \chi V) = H \text{grad}(H) . \qquad (2)$$

From (2) it follows that in order to obtain higher values of the extraction force f_m, it is necessary to increase the magnetic field strength H and its gradient grad(H). An increase in the magnetic field strength H in separators with electromagnetic excitation has its limit, due to the saturation of the elements of the magnetic circuit. The H growth is also associated with an increase in power consumption, which leads to a higher cost of devices. At the same time, increasing the values of grad(H) can be achieved by optimizing the shape, geometric sizes and the relative position of the elements of the multicomponent magnetic matrix of the separator. Research in this area represents the greatest practical and theoretical interest.

Analysis of literary data and problem definition. Analytical, numerical and experimental methods have been used to calculate the magnetic characteristics of polygradient separators. In [3], the influence of the shape of the intersection of the elements of the magnetic medium on the distribution of the magnetic flux density and the gradient of the magnetic field of the polygradient separator was studied. In this work, using the ANSYS software system implementing the finite element method,

it has been established that the strongest and most heterogeneous magnetic field is provided by a polygradient medium based on triangular elements. In view of this, a large number of publications are devoted to studies of polygradient matrices based on triangular elements. Thus, in [4] the connection of the strength and gradient of the magnetic field around the acute angle of the magnetic matrix with the direction of the bisector of this angle with respect to the direction of the external field is substantiated. It is shown if the bisector of an acute angle is parallel to the direction of the field, then the strength and gradient of the field around the angle increase. In [5], it is shown that the width of the gaps between the triangular plates of the matrix should be 1.5-2 times larger than the maximum particle size, since reducing the gap width will lead to a rapid closure of the matrix. When choosing a tooth angle, pole height and plate height, the magnetic force and the zone of removal of inclusions should be taken into account [6].

The analysis of literary sources [1-6] has shown that the calculation of the magnetic field in the matrices of polygradient separators is carried out mainly in a limited volume of the working zone for single, in particular, triangular elements of the matrix, followed by the application of the resulting regularities to a group of elements. This does not take into account the influence of the relative arrangement of elements on the nature of the distribution of the magnetic field, which complicates the comparative analysis of the matrices of various configurations. Therefore, further studies of approaches to conducting a comparative analysis of the strength characteristics of magnetic fields of multicomponent matrices of polygradient separators of different configurations are required.

The goal of the work is the establishment of the dependence of the strength characteristics of the polygradient electromagnetic separator on the geometric parameters of the plate type elements of the multicomponent matrix.

Research material and results. In previous studies, the authors obtained the following results:

• an advanced design of a polygradient electromagnetic separator for cleaning bulk powder-like materials from fine-grained ferromagnetic impurities of 0.005-5 mm in size is proposed [7];

• six structural variants $S_i = (S_1, S_2, …, S_6)$ of a plate type magnetic matrix of a polygradient separator based on triangular elements, whose geometric models are shown in Table 1, were obtained using mirror, portable, central and sliding symmetry operations;

• using a computational experiment, a preliminary comparative analysis of S_i structures was performed to evaluate the degree of magnetic field inhomogeneity in their working gaps [8].
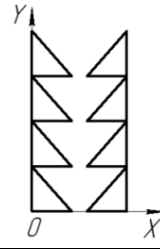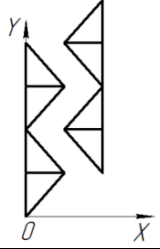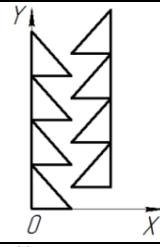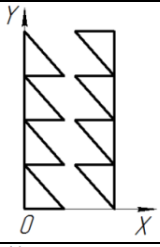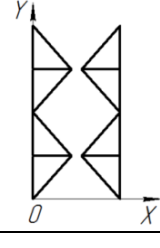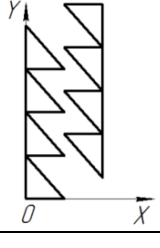
The preliminary estimation of the degree of inhomogeneity of the magnetic field in the working zones of the synthesized structures is accomplished by comparing the indices of field inhomogeneity along characteristic lines [8] as which the lines joining the vertices of opposite triangular plates and passing through the regions with the highest non-uniformity of the

magnetic field are taken. Along the characteristic lines in the working regions of the synthesized structures S_i, the local values of the magnetic field strength H field were calculated using the tools of the Elcut program. After that, for the various configurations of the polygradient media, the coefficient k_i of field heterogeneity was determined by the formula

$$k_i = (H_{max} - H_{min})/(H_{max} + H_{min}),$$

where H_{max}, H_{min} are the maximal and minimal values of the magnetic field strength, respectively.

Table 1
Geometric models of structural variants of the matrix

Code	Geometrical model	Code	Geometrical model
S_1		S_4	
S_2		S_5	
S_3		S_6	

The main geometric dimensions of the working area, which varied in the study, are shown in Fig. 1 on an example of S_3 structure. Here are the notation: δ – the interpolar working gap which corresponds to the minimum distance between the plates; α – the angle at the vertex of the pole; b – the base of the pole overhang; a – the working width of the matrix. The following geometric similarity criteria for the studied areas were given: $X_1 = b/a$ and $X_2 = \alpha$. The ranges of variation of the geometric similarity criteria X_1 та X_2 of practical interest were: $X_1 = b/a = 0.1…0.4$; $X_2 = \alpha = 0.11\pi…0.44\pi$.
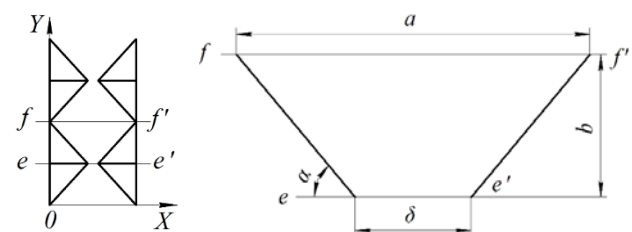

Fig. 1. Basic geometric dimensions of the working area on an example of the structure S_3

Calculated values of the heterogeneity coefficient k_i varied from zero to one and were mapped according to the classification proposed in [9]: $k_i \leq 0.3$ – a weakly homogeneous (or slightly heterogeneous) field; $0.3 < k_i \leq (0.9...1)$ is a non-uniform field. This classification is in good agreement with the coefficient of variation V, the main statistical indicator characterizing the homogeneity of the data. In mathematical statistics, it is assumed that if the value of the coefficient V is less than 33 %, then the aggregate of data is homogeneous, and if more than 33 %, then heterogeneous.

Thus, as a result of calculations, structures with weakly nonuniform fields for which $k_i \leq 0.3$ were cut off. Studies have also shown that in structures characterized by high inhomogeneity of the field, the average magnetic field strength H may be low. Therefore, at the next stage, for the purpose of determining rational variants of polygradient matrices, an estimate of the entire spectrum of the force field Hgrad(H) in the plane of the working zones of the investigated structures in the two-dimensional formulation was made. The experience of designing magnetic separators shows that the relative effect of a three-dimensional magnetic field is approximately the same for all points of plane magnetic models of working interpolar zones and does not depend on geometric similarity criteria $X_1 = b/a$ and $X_2 = \alpha$ [1]. Therefore, the magnetic field in the working zone of the separator can be considered planar parallel.

To solve the task of estimating the spectrum of the magnetic field, a program with the use of the Java 7 programming language and the Spring framework, which at the input of the input, processes the results of the calculation of the magnetic field strength H, obtained in the Elcut program in the form of Excel files, was developed. Apache POI Library is intended to work with Excel files. The result of the program execution is a new Excel file with data of calculating the force characteristic Hgrad(H) of the magnetic field. The main stages of the computational experiment are shown in Fig. 2.
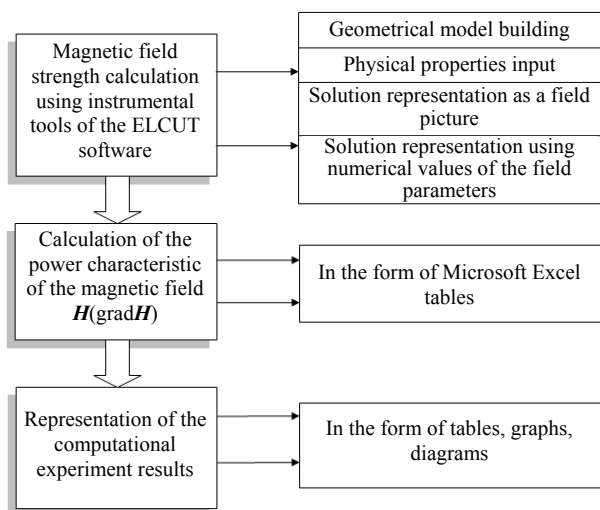

Fig. 2. Main stages of the computational experiment

To solve the problem of determining rational variants of polygradient matrices, a method of comparative analysis of force characteristics of investigated variants of matrix structures with corresponding characteristics of the basic variant of a separator, which is attributed to structure S_4, was used. The basic version of the magnetic separator was developed empirically and implemented in the form of a physical model, experimental studies of which confirmed its ability to operate [7]. The optimality test for the base version of the separator was not carried out. Characteristics of the basic separator model: structure code S_4; geometric similarity criteria $X_1 = b/a = 0.3$; $X_2 = \alpha = 0.11\pi$.

For the base model of the separator, during the computational experiment, the part P_b of the working zone (interpolar gap) of the matrix was determined, in which the power factor f_m satisfies the requirement $f_{min} \leq f_m \leq f_{max}$, where f_{min} is the minimum limiting value of the force characteristic $f_{min} = (H\text{grad}(H))_{min}$, which provides, on the basis of the experience of designing magnetic separators, sufficient efficiency of removal of ferromagnetic inclusions (in the calculations the accepted value $f_{min} = 3 \cdot 10^8$ A^2/m^3 [10]); f_{max} is the maximum value of the specific reduced force obtained by calculation for the base model of the separator, which was in the research $f_{max} = (H\text{grad}(H))_{max} = 10.8 \cdot 10^9$ A^2/m^3. This part of the area of the working zone P_b was expressed as a percentage relative to the value P of the entire area of the working zone through the parameter γ ($\gamma = P_b / P$). The parameter γ depends on the geometric criteria X_1, X_2 and can be defined as the effective area of the working zone of the matrix. For the basic variant of the separator, the parameter γ was $\gamma = 7$ %. In calculations, the parameter γ_1, which characterizes the part of the area of the working zone where the condition $f_m > f_{max} = 10.8 \cdot 10^9$ A^2/m^3 is fulfilled may also optionally be determined if necessary. Rationalities will be considered variants of the studied systems that satisfy the condition

$$\gamma = (X_1, X_2) \rightarrow \max. \qquad (3)$$

The results of the calculations obtained during the computational experiment showed that condition (3) best satisfies the structures S_4 and S_3 for which the highest values of the parameter γ were obtained (Fig. 3). The maximum values of the parameter γ for structures S_3 and S_4 were, respectively:

- at $X_2 = \alpha = 0.11\pi$ – 54.2 % and 54.6 %;
- at $X_2 = \alpha = 0.18\pi$ – 60.3 % and 65 %;
- at $X_2 = \alpha = 0.22\pi$ – 52.4 % and 53.2 %;
- at $X_2 = \alpha = 0.28\pi$ – 42.1 % and 42 %
- at $X_2 = \alpha = 0.33\pi$ – 32.0 % and 31.6 %;
- at $X_2 = \alpha = 0.39\pi$ – 23.5 % and 22.9 %.

The peculiarity of the structures S_4 and S_3 is that in both structures the single plate type element has the shape of an isosceles triangle, the direction of the bisector of an acute angle at the vertex of which coincides with the direction of the external magnetizing field. These results are in good agreement with the conclusions obtained in [2, 4], where it is established that the strength and gradient of the field around the angle of the triangular element of the matrix increase when the bisector of the acute angle is parallel to the direction of the field.
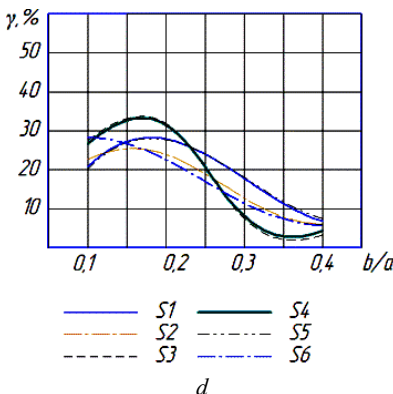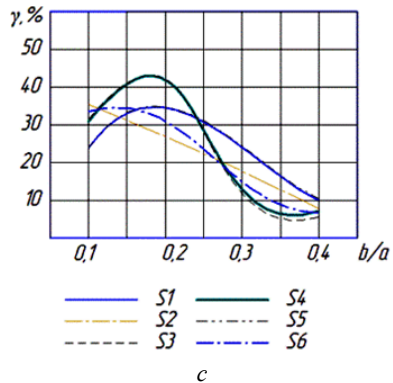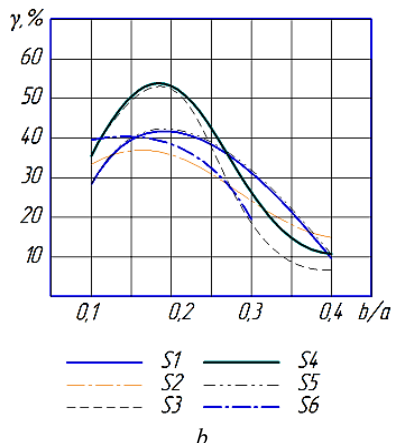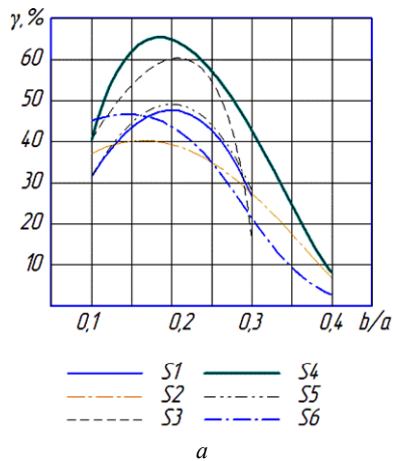
Fig. 3. Results of variant calculations of the parameter γ:
a) $X_2=\alpha=0.18\pi$; b) $X_2=\alpha=0.22\pi$; c) $X_2=\alpha=0.28\pi$; d) $X_2=\alpha=0.33\pi$

As data of Fig. 3 show, the parameter γ ($\gamma = 65$ %) becomes the maximum value for the S_4 structure at $X_1 = b/a = 0.18$. Therefore, the structure S_4 was chosen for further research.

For more accurate determination of rational geometric parameters of plate type elements of the matrix of structure S_4, the dependence $\gamma = f(X_2)$ is constructed for $X_1 = b/a = 0.18$ (Fig. 4), which has a clearly expressed extremum corresponding to the point $X_2 = \alpha = 0.15\pi$, for which γ becomes $\gamma = 73.3$ %. Thus, the parameters $X_1 = b/a = 0.18$ and $X_2 = \alpha = 0.15\pi$ should be considered as rational for the structure S_4 (accordingly, the angle at the vertex of the triangular element of the matrix is $2\alpha = 0.3\pi$). Such a result is consistent with the data given in [6], where it is established that the magnetic strength and intensity of the magnetic field in the edge of the tooth tend to increase, when the angle 2α at the tooth top satisfies the condition $2\alpha \leq 0.37\pi$.
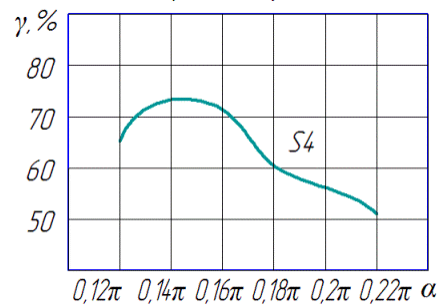

Fig. 4. Dependence of the parameter $\gamma = f(X_2)$ at $X_1 = b/a = 0.18$

Conclusions.

The dependence of the force characteristics of the polygradient electromagnetic separator on the geometric parameters of the plate type elements of the multicomponent matrix is established.

The analysis carried out in the work showed that the S_4 structure with the parameters $X_1 = b/a = 0.18$ and $X_2 = \alpha = 0.15\pi$ can be considered rational in terms of the high value of the effective area of the working zone ($\gamma = 73.3$ %). The results of the study are in agreement with the works of other authors.

REFERENCES
1. Zagirnyak M.V., Branspiz Yu.A., Shvedchikova I.A. *Magnitnye separatory. Problemy proektirovanija* [Magnetic separators. Problems of designing]. Kiev, Tehnika, 2011. 224 p. (Rus).
2. Ge W., Encinas A., Araujo E., Song S. Magnetic matrices used in high gradient magnetic separation (HGMS): A review. *Results in Physics*, 2017, vol.7, pp. 4278-4286. **doi: 10.1016/j.rinp.2017.10.055.**
3. Ren L., Zeng S., Zhang Y. Magnetic field characteristics analysis of a single assembled magnetic medium using ANSYS software. *International Journal of Mining Science and Technology*, 2015, vol.25, no.3, pp. 479-487. **doi: 10.1016/j.ijmst.2015.03.024.**
4. Song C.C., Ning G.H., Yuan Z.Y., Jing L.X., Hui C.C., Yao M.S. Investigation of the influence of different matrix rotation angles on the surrounding magnetic field in a uniform magnetic field. *Ming Metall Eng*, 2014, no.34, pp. 290-294.
5. Svoboda J. *Magnetic Techniques for the Treatment of Materials*. Boston, Kluwer Academic Publ., 2004, 99 p. **doi: 10.1007/1-4020-2107-0.**
6. Shun Z.Y., Liang S.C., Juan W.H., Yue W.F. Experimental study on magnetic separation by conical flux gathering media and optimization of its cone angle. *Min Process Equip*, 2012, pp. 74-79.

7. Shvedchikova I.A., Lutsenko I.A., Romanchenko Ju.A. A study of polygradient media structure regularities. *Eastern-European Journal of Enterprise Technologies*, 2015, vol.4, no.7(76), pp. 62-67. (Rus) **doi: 10.15587/1729-4061.2015.47785.**

8. Shvedchykova I., Romanchenko J., Nikitchenko I. Comparative analysis of inhomogeneity degree of magnetic field of polygradient magnetic separators for purification of bulk materials. *2017 International Conference on Modern Electrical and Energy Systems (MEES)*, Nov. 2017. **doi: 10.1109/mees.2017.8248873.**

9. Nikolov N.A. Quantitative criterion of the spatial inhomogeneity of the electromagnetic field in the near-field zone of a loop radiator. *Cybernetics and Systems Analysis*, 2013, vol.49, no.2, pp. 309-315. **doi: 10.1007/s10559-013-9513-4.**

10. Popov Yu.V. The examination practice of industrial safety of magnetic protection equipment (magnetic separators and columns) of production facilities for storage, processing and use of plant raw materials. *Federal Service information bulletin*, 2006, no.24, pp. 48-57. (Rus).

Juraj Gerlici[1], *Professor, Dr. Ing.,*
I.O. Shvedchykova[2], *Doctor of Technical Sciences, Professor,*
J.A. Romanchenko[3], *Lecturer,*
I.V. Nikitchenko[3], *Senior Instructor,*
[1] University of Žilina, Žilina, Slovak Republic,
1, Univerzitná, SK 01026 Žilina, Slovak Republic,
phone 421(41)513 2550,
e-mail: juraj.gerlici@fstroj.uniza.sk
[2] Kyiv National University of Technologies and Design,
2, Nemirovich-Danchenko Str., Kyiv, 01011, Ukraine,
phone +380 50 9712574,
e-mail: ishved89@gmail.com
[3] Volodymyr Dahl East Ukrainian National University,
59-a, pr. Central, Severodonetsk, Lugansk region 93400, Ukraine,
phone +380 99 0326854,
e-mail: romanchenkojulia@i.ua

V.G. Zhekul, O.V. Khvoshchan, O.P. Smirnov, E.I. Taftaj, I.S. Shvets

ANALYSIS AND DEVELOPMENT OF THE BUBBLE MODEL OF THE FORMATION STAGE OF HIGH-VOLTAGE BREAKDOWN OF THE WATER GAP

Purpose. A high-voltage underwater electric explosion, realized by discharging a capacitor into a water gap, is characterized by three main stages: the stage of formation of the plasma channel, the channel stage and post-discharge one. Substantially, the channel, post-discharge stages and the efficiency of energy release in the channel and the increase in the hydrodynamic effect on the object being processed depend on the parameters of the stage of formation. The purpose of the work was to review the existing mechanisms for the formation of a high-voltage discharge channel with the analysis and development of a bubble model of the stage of formation of water gap breakdown. Methodology. We have applied the analysis of existing theories on the formation of a high-voltage discharge channel, the carrying out of electrophysical studies with the processing of the obtained data. Results. A review and analysis of modern concepts of pre-breakdown processes in a high-voltage electric discharge in a liquid showed that the «bubble» model of the ignition of a discharge is applicable at an electric field strength (36 – 180) kV/cm. We have further developed the bubble model of the stage of formation of high-voltage breakdown on the results of experimental studies of the electrical characteristics of the discharge in the aqueous electrolyte with increased hydrostatic pressure and minimum voltage providing ignition of the discharge. A qualitative description of three phases of the stage of formation of the plasma channel in the liquid electrolyte is proposed. Originality. We have further developed the bubble model of the stage of formation of high-voltage breakdown of the liquid electrolyte on the results of experimental studies of the electrical characteristics of the discharge in the aqueous electrolyte with increased hydrostatic pressure and minimum voltage providing ignition of the discharge. A qualitative variation of the resistance of the gap in the pre-breakdown stage of the discharge is considered. Practical value. Determination of the scientific basis for creating a methodology for calculating the pre-breakdown characteristics of an electric discharge to improve the efficiency of electric discharge devices. References 19, figures 4.
Key words: **high-voltage electric discharge, liquid electrolyte, oscillogram, pre-breakdown processes, bubble model**.

Выполнен обзор и анализ современных представлений о предпробойных процессах при высоковольтном электрическом разряде в жидкости. Показано, что «пузырьковая» («bubble») модель зажигания разряда применима при напряженности электрического поля (36 – 180) кВ/см. По результатам экспериментальных исследований электрических характеристик разряда в водном электролите при повышенном гидростатическом давлении и минимальном напряжении, обеспечивающем зажигание разряда, получила дальнейшее развитие пузырьковая модель стадии формирования его высоковольтного пробоя. Предложено качественное описание трех фаз стадии формирования плазменного канала в жидком электролите. Библ. 19, рис. 4.
Ключевые слова: **высоковольтный электрический разряд, жидкий электролит, осциллограмма, предпробойные процессы, пузырьковая модель.**

Introduction. The development of electrohydraulic technologies in the second half of the twentieth century caused an increased interest in studying the characteristics of a pulsed electric discharge in liquids throughout the world. In the case of a high-voltage underwater electric explosion, realized by discharging a capacitor into a water gap [1], three main stages are selected:

1) the stage of formation of the plasma channel closing the interelectrode gap;

2) the channel stage, characterized by a sharp increase in the discharge current and the rapid release of electrical energy in the channel of high conductivity, which closes the opposite electrodes;

3) post-discharge stage – pulsation of the vapor-gas cavity after the end of the release of electrical energy in the discharge channel.

To a large extent, the channel and post-discharge stages, and, consequently, the efficiency of energy release in the channel and the increase in the impact on the object depend on the parameters of the stage of formation.

The goal of the work is a review of the existing mechanisms of the formation of a high-voltage discharge channel with the analysis and development of a bubble model of the stage of formation of water gap breakdown.

Basic definitions. Fig. 1 shows typical oscillograms of current and voltage for a high-voltage breakdown of a conducting liquid [2]. According to the oscillograms, the following parameters of the stage of formation of the current-carrying channel are determined:

• pre-leader time (discharge ignition time) t_{dl} is the time from the moment of voltage application to the electrode system U_0 up to the moment of the beginning of the current increase corresponding to the instant of appearance of the plasma leader on one of the electrodes;

• leader time t_l is the time from the moment when the current rises up to the beginning of a sharp decrease in the voltage U_{0a} and a simultaneous increase in the rate of current rise, which characterizes the onset of the channel stage of the discharge.

The pre-lieder stage corresponds to approximately constant current i_{dl} and a slowly decreasing voltage U_{dl}, the slope of which is determined by the time constant of the storage discharge. The growth of the leader system at the leader stage leads to a decrease in the resistance of the gap, an increase in the current i_l and a decrease in the voltage U_l. Under the ignition voltage of the discharge U_z we mean the minimum voltage at which the plasma branch is formed on the electrode, and under the breakdown voltage the minimum voltage at which the discharge passes to the channel stage. The time of the pre-breakdown stage of the formation of a conductive channel t_{pp} is calculated by the formula:
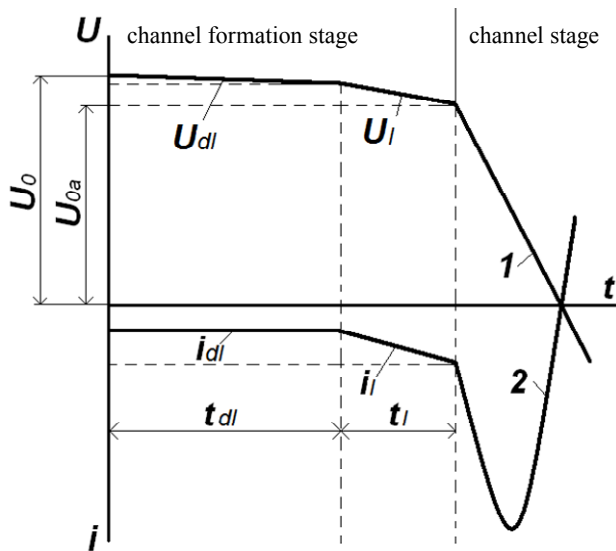
$$t_{pp} = t_{dl} + t_l. \tag{1}$$

Fig. 1. Oscillograms of current and voltage in breakdown of conductive fluid: 1 – voltage U; 2 – current i

A brief review of the concepts of pre-breakdown processes in a liquid. Immediately after applying voltage to the electrode system in the liquid, filling the interelectrode gap, processes that can lead, ultimately, to the formation of plasma branches begin. The influence of the field is accompanied by the appearance of currents, which can be registered with the help of special equipment. A further change in the electric field in the interelectrode gap will be observed due to a decrease in the voltage on the capacitor and phenomena occurring in the liquid itself when the field is applied.

The theory of the development of breakdown phenomena in liquids was originally based on the study of discharges in gases. In the thirties of the twentieth century, the Soviet scientist L.A. Yutkin received the first experimental results on the electro-hydraulic effect, and special attention was paid to processes at the high-voltage breakdown of liquids beginning in the second half of the twentieth century.

Initially, two groups of hypotheses about the mechanism of formation of a discharge in liquids were selected, depending on how they explain the appearance of charge carriers. The first group united hypotheses in which the process of discharge formation did not imply a violation of the phase homogeneity of the liquid. The second group provided for gas formation in a liquid and only then – ionization and breakdown. V.Ia. Ushakov combined the first group of mechanisms by the term electrical breakdown, the second one – by the electrothermal breakdown [3]. Electrical breakdown provides for the development of ionization processes in the liquid, and the electrothermal breakdown – the development of primary ionization processes in the gas phase after the boiling of the liquid.

Under the electrothermal initiation mechanism of the discharge, the author meant the following set of phenomena: the flow of the conduction current under the applied electric field, the heating of the liquid in the near-electrode regions with the maximum field strength, the boiling of the liquid, the ionization of the vapor gas cavities, and the formation of the rudiment of the plasma channel. This mechanism can be realized for large values of the product of the specific electrical conductivity of a liquid on the duration of the voltage action. Since for pulse actions the duration of the voltage applied to the opposite electrodes does not usually exceed several hundred microseconds, such an initiation mechanism is likely in liquids with a high electrical conductivity, especially in electrolytes. The author considered the electrothermal initiation mechanism to be rare for pulsed breakdown of liquids.

I.P. Kuzhekin interpreted the mechanism of water breakdown with a specific electric conductivity of $2.5 \cdot 10^{-4}$ S/cm by electrothermal [4] at field strengths at the tip electrodes $E = (8\text{-}36)$ kV/cm. In hundreds – thousands of microseconds from the moment of applying a voltage, near the tip a glow appears, the expansion of which leads to breakdown of the gap. At $E = (36\text{-}180)$ kV/cm, the leader form of the discharge takes place, and the formation of the leaders is preceded by the luminescence of a high-voltage electrode. At $E > 180$ kV/cm, the luminescence to the emergence of leaders is not observed. For small E, the movement of the leaders is a stepwise one, for large ones it is continuous.

Calculation of the dynamics of the formation of a gas bubble in water and its heating under the influence of the voltage applied to the electrodes by the electrothermal model at electric field strength up to 10 kV/cm is given in [5]. The use of a multiphysical calculation model in the COMSOL program showed that a discharge in water with a conductivity of 3 S/m of a 5 mF storage capacitance charged to a voltage of 3 kV leads to an increase in the temperature in the interelectrode gap to (300-800) K and the transition of water to a vapor state.

The electrical breakdown mechanism was identified by V.Ia. Ushakov [3] by the absence of gas formation in the liquid before the appearance of luminescence, high speed of germination of the breakdown branch (up to 10^5 m/s and more), the absence of dependence of the electrical strength on the liquid temperature up to the boiling point and on the electrical conductivity of the liquid.

Considering the breakdown of low-conducting and dielectric liquids, the authors of [6] advance the idea of the significant role of emission, impact ionization, and autoionization of liquid molecules. In their opinion, autoionization occurs in the near-electrode layer of a liquid under the action of the field of the electrode surface microrelief. The strength of such a field can exceed by three orders of magnitude the average field strength in the gap, and the electrons arising during autoionization move to the anode, multiplying along the path due to impact ionization.

In [7], the effect of nanosecond voltage pulses on the breakdown of distilled water was studied with the justification of electrostriction as a factor in the development of optical density perturbations and rarefaction of water initiating the breakdown.

A brief review of the mechanisms of formation of streamer discharges in a liquid [8] mentions the influence of molecular ionization and ion dissociation factors, which depends on the electric field, Auger mechanism, accompanying the electric breakdown mechanism.

The work [9] is devoted to the investigation of the electrical and hydrodynamic characteristics of the discharge in water at an elevated hydrodynamic pressure (up to 8 MPa). Here, the discharge of a capacitive storage device of 60 μF, charged to (8-13) kV, was studied. The study showed that in the range (0.1-4) MPa in water there are gas bubbles that affect both the pre-breakdown characteristics of the discharge and the amplitude of the pressure wave excited by the discharge. In this case, in the range of up to 3 MPa, the amplitude of the pressure pulse increases with increasing hydrostatic pressure, and with a further increase in the hydrostatic pressure to 8 MPa, it decreases.

Thus, the researchers clearly determine the mechanism of formation of a discharge in a liquid by an electrothermal model (with electric field strength of up to 36 kV/cm) and an electrical model (with a field strength above 180 kV/cm). In the range of strengths limited by the indicated numerical values, the scientists proposed a «bubble» model of ignition of a discharge in a liquid.

«Bubble» model of ignition of the discharge. One of the first hypotheses about the mechanism of pulsed electric breakdown of water based on the «bubble» ignition model as part of the electrothermal model was put forward by E.V. Ianshin. The results of the studies [10] allowed the authors to conclude that the motion of electrons in a condensed medium will be accompanied by the release of energy in it in an amount that will ensure the shock boiling of the liquid and the formation of microbubbles, leading to a violation of the optical uniformity of the liquid. In these bubbles, ionization phenomena develop, which leads to the formation of a breakdown branch. E.V. Ianshin notes the possibility of the development of instabilities in this stage, associating with them a disordered structure of dendrites. After the breakdown of the gas micro-gap, the neighboring liquid layer boils up at the head of the germinated leader, then the process repeats.

Further development of the «bubble» model of the breakdown of polar and nonpolar dielectric liquids was obtained in the works of S.M. Korobeinikov [11]. According to the results of the experiment, under conditions of low hydrostatic pressure, bubbles can exist both near the electrodes and be formed with time after applying voltage to them due to microcavitation, local overheating of liquid and electrostrictive phenomena. The model of the processes leading to breakdown of the dielectric presupposed discharge in the bubble when the critical voltage reached on it, the deformation of the bubble by Coulomb forces, the field amplification in the region of the poles of the bubble, and the discharge into the liquid after reaching the critical field strength. On the basis of theoretical analysis, the author analytically obtained a particular solution for estimating the growth time of a bubble, which he relates to the pre-breakdown time when a stepwise voltage is applied.

According to the author's hypothesis [11], ionization processes (partial discharges) occur in it under the action of an electric field after reaching a certain value of the voltage drop (due to both bubble growth and the voltage applied to the electrodes) on the bubble. After discharge, the field in the bubble decreases due to shielding of the external field by the settled charges, which causes weakening or termination of the ionization processes. The action of the electric field on the settled charge leads to a stretching of the bubble along the field, and also to the progress of the charge into the interior of the liquid at a rate determined by the mobility of the charge carriers. In this case, two situations are possible: maintaining a discharge in the form of a glow discharge or stopping the discharge.

In the first case, a voltage is maintained on the bubble, apparently, consistent with Paschen law. In the latter case, the voltage on the bubble rises, which leads to a repeated discharge and the motion of a new wave of charges in the liquid. The determining parameter, the pressure on the bubble wall, is due to the action of Coulomb forces on the injected and surface charges and the increase in pressure in the bubble due to the heating of the gas in it. Ignition of a discharge in a liquid occurs when the field strength near the pole of the bubble reaches a critical value.

The author considered the criterion for the ignition of a discharge in a liquid to be a certain critical strength $E_{max} = (10^7 - 10^8)$ V/cm. The proposed bubble model allows, in the author's opinion, to calculate the pre-breakdown time. However, the value of the field strength at which the breakdown of liquids occurs is determined by Martin formula:

$$E_b = \frac{A}{t^{0.5} \cdot S^{0.1}},\qquad(2)$$

where A is the constant depending on the type of liquid and the polarity of the initiating electrode, t is the duration of applied voltage pulse, S is the parameter that depends on the bare part of the electrode.

Investigations of breakdown of conducting non-degassed liquids, the results of which are given in [12], allowed the authors to conclude that in the range of the electrical conductivity of a liquid $2 \cdot 10^{-5} - 2 \cdot 10^{-3}$) S/cm in the gaps $(3.5 - 13)$ cm its breakdown in an inhomogeneous field is not associated with the preliminary formation of a continuous gas bridge even at times of several tens of microseconds. Gas bubbles are formed near the electrode or head of the discharge channel, and ionization of these bubbles contributes to the development of the discharge channel.

In [13], the processes of initiation and propagation of positive underwater streamers in water were studied using pulsed voltage with duration of 10 μs based on the oscillography of the electrical characteristics of the discharge and shadow recording of the discharge development by an ultrahigh-speed camera. Thus, at field strength of 10 MW/cm at the tip electrode, clusters of microbubbles were observed near the electrode, within which microdischarges characterized by luminescence in the liquid occurred.

The above results indicate that scientists from many countries of the world have been engaged in researching the pre-breakdown characteristics of liquids. The basis of research has almost always been an experiment using the most modern techniques to obtain the necessary empirical dependencies.

Ignition of a discharge in conducting liquids. The specialists of the Institute of Pulse Processes and Technologies (IPPT) of the National Academy of Sciences of Ukraine studied the mechanisms of discharge formation in conductive liquids for a number of years. Thus, a unified approach to the description of fast and slow spark discharges in condensed media as phase transition waves is proposed in [14]. In [15], the results of an experimental study of the effect of high hydrostatic pressure (up to 50 MPa) and temperature (up to 373 K) on the stage of formation of the discharge channel in the liquid and the channel stage of the discharge are presented. On the basis of these experimental data, the value of the discharge ignition voltage for water gaps from 30 to 40 mm is estimated by the empirical formula [15]:

$$U_z = 32.9 \cdot P_{gs}^n \cdot \left(r_{el} \big/ \sigma_0 \right)^{0.45}, \qquad (3)$$

$$n = \begin{cases} 0.1 - 0.12; & \sigma_0 = (0.5 - 0.1) S/m \\ 0.12 - 0.13; & \sigma_0 = (0.1 - 0.03) S/m \end{cases},$$

where U_z is the value of ignition voltage of the discharge, kV; P_{gs} is the hydrostatic pressure, Pa; σ_0 is the specific electrical conductivity of aqueous electrolyte, S/m; r_{el} is the radius of curvature of the rod electrode, m.

A theoretical description of the initial stage of discharge in a conducting liquid, based on the hypothesis of the development of instabilities in its volume under the action of an electric field, is presented in [16]. The mathematical model included a system of differential equations describing the development of overheating instability, taking into account electrohydrodynamic phenomena and stabilizing heat transfer factors. The possible role of electroconvective instability in the process of germination of the breakdown branch was noted. The results of calculating the time constant of the development of the overheating instability for the spherical geometry of the electrode system were compared with the duration of the pre-leader stage of the discharge, measured experimentally with a high-speed photograph of the pre-breakdown stage of the discharge of a high-voltage capacitor on a water gap with synchronous oscillography of its electrical characteristics. Comparison of the results of calculation and experiment confirmed the correctness of the theory proposed.

The development of the theory of breakdown of conducting liquids is presented in [2, 17]. It was suggested that the threshold of ignition of the discharge in the conducting liquid would be determined by conditions ensuring the independence of the discharge in the resulting gas-vapor cavern. The ignition pattern was as follows. The gas-vapor cavity is formed at the electrode with the maximum field strength, as a result of the continuous heating of the liquid it increases in its size d. The growth of the cavity is accompanied by an increase in the applied voltage $U(d)$, the value of which is determined, among other things, by the potential difference between the electrodes. The breakdown of the cavity is possible when the breakdown voltage and the gap size of the critical values are reached, which can be estimated by the Paschen formula:

$$U(d) = U_{cr}(p \cdot d), \qquad (4)$$

where p is the gas pressure in bubble.

The critical values of voltage and diameter were calculated for a system of spherical concentric electrodes with neglect of the inhomogeneity of the field in the cavity. The results of the calculations were compared with the experimental data. The experiment was carried out on the electrode system «point – plane», and the rod protruding from under the insulating tip in the shape of a hemisphere. The experimental research circuit provided a practically rectangular voltage pulse in the stage of ignition of the discharge. The experiment was carried out in water with specific conductivity $(10^{-1} - 10^{-3})$ S/m at atmospheric hydrostatic pressure. Comparison of the calculated and experimental values of the ignition voltage showed good convergence in the range of the radius of the electrode-point of $(0.5 - 5.0)$ mm and the interelectrode gap of $(60 - 100)$ mm.

In accordance with the model given in [18], the ignition voltage U_z should be determined as the maximum of two quantities:

$$U_z = \max\left(U_{thr}, U_{cr}\right), \qquad (5)$$

where U_{thr} is the threshold (minimum) voltage, at which it is possible to develop an overheating instability; U_{cr} is the critical ionization voltage of the gas in the bubbles formed in the heating zones, which leads to the breakdown of the bubble and the subsequent formation of a plasma branch of the breakdown.

The threshold for the development of an overheating instability is determined by the energy capacity of the source and is ensured by maintaining a constant voltage in the interelectrode gap. In the case where the voltage source is a charged capacitor bank, the threshold voltage is determined according to the expression

$$U_{thr} = \left(\frac{\rho \cdot c_p \cdot r_{el}^2}{\alpha \cdot \sigma_0 \cdot R \cdot C} \right), \qquad (6)$$

where ρ is the liquid density, kg/m^3; c_p is the specific heat of the liquid, J/(kg·K); σ_0 is the liquid conductivity, S/m; α is the temperature coefficient of fluid electrical conductivity, K^{-1}; R is the interelectrode gap resistance, Ω; C is the capacitor bank capacitance, F; r_{el} is the anode radius, m.

For the electrode system rod – plane, resistance of the interelectrode gap can be calculated from expression (7) using the design scheme shown in Fig. 2, in which the electrode system is modeled by concentric hemispheres [2].

$$R = \frac{1}{2 \cdot \pi \cdot \sigma_0} \cdot \left(\frac{1}{r_1} - \frac{1}{r_2} \right), \qquad (7)$$

The critical voltage U_{cr} is defined as the breakdown voltage of a bubble of diameter d_{cr} appearing in the zones of maximum liquid heating. According to [2], for the electrode system shown in Fig. 2, the critical breakdown voltage of a gas bubble can be determined from expression

$$U_{cr} = \frac{B \cdot p_0 \cdot d_{cr}}{c + \ln(p_0 \cdot d_{cr})} \cdot \left[1 - \frac{1}{h-1} \cdot \left(\frac{h}{1 + \frac{d_{cr}}{r_1}} - 1 \right) \right]^{-1} , \quad (8)$$

where B, c are the empirical constants that depend on the composition of the gas inside the bubble (for example, for water vapor at $E/p = 120 - 800$ (V·m)/N constants $B = 290$, $c = 0.3 - 0.6$); p_0 is the normal atmospheric pressure, $p_0 \approx 10^5$ Pa; $h = r_2/r_1$; d_{cr} is the critical (minimal) size of the bubble at which its breakdown occurs determined according to (9):

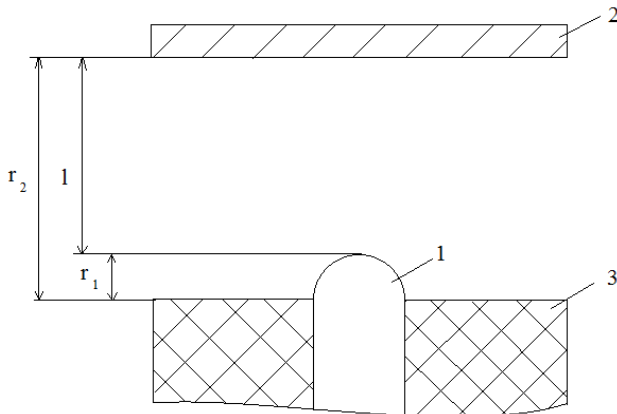$$d \cdot [c + \ln(p_0 \cdot d) - 1] = r_1 . \quad (9)$$

Fig. 2. The design scheme for calculation of the resistance of the gap in the electrode system rod – plane:
1 – electrode-anode (rod); 2 – electrode-cathode (plane);
3 – insulator; l is the length of the interelectrode gap, m;
$$r_2 = l + r_1$$

The calculation according to formula (8) assumes the following assumptions:

• the field inside the bubble is uniform;

• the pressure inside the bubble is equal to atmospheric pressure;

• the voltage $U(d)$ applied to the bubble is defined as the potential difference between the surface of the electrode-anode surface and the equipotential surface lagging behind it at a distance d;

• the distortions introduced by the bubble into the field distribution in the near-electrode region are not taken into account;

• the breakdown voltage of a bubble is determined by the Paschen similarity law.

The presented bubble model makes it possible to estimate the voltage of ignition of an electric discharge in water under normal atmospheric conditions.

Justification of the bubble discharge model based on the results of oscillography of its electrical characteristics. The physical essence of the bubble model is well analyzed when processing oscillograms of the threshold discharge modes in the water electrolyte with increased hydrostatic pressure (Fig. 3). In these modes, ignition of the discharge (luminescence) near the anode can be observed, but the streamer either does not reach the opposite electrode-cathode (Fig. 3,a), or the residual voltage on the capacitor at the beginning of the

channel stage is so small that the current of the active stage of discharge is comparable with pre-breakdown currents (Fig. 3,b). Oscillograms were obtained on a laboratory bench, which makes it possible to simulate a high-voltage breakdown of a water gap under conditions of high hydrostatic pressure [19].

As can be seen from Fig. 3,a, the moment of operation of the photodiode sensor installed at a distance of 60 mm opposite the discharge channel to record the start of the luminescence, coincides with the characteristic curve of the current curve in the stage of discharge formation. For a qualitative analysis of the physical processes occurring at this stage of the discharge, the temporal dependences of the change in the resistance of the water gap in the electrode system (the ratio of the voltage across the gap to the current in it) were constructed. The dependencies are shown in Fig. 4. They correspond to the results of processing the oscillograms shown in Fig. 3.

Analysis of the data in Fig. 4 showed that the stage of formation of an electrical discharge in a liquid can be divided into a number of time phases.
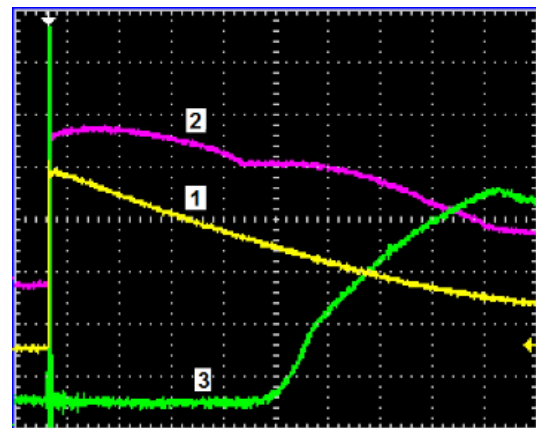
a
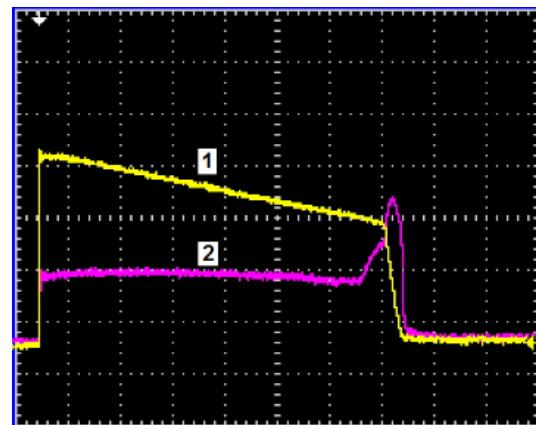
b

Fig. 3. The oscillograms of the threshold conditions for the electrical discharge of capacitance $C = 2.47$ uF charged to voltage U_0 in an electrode system «point-plane» with a tip-anode radius $r_{el} = 1.5$ mm and a length of the interelectrode gap $l = 24$ mm filled with an aqueous electrolyte with specific electrical conductivity $\sigma_0 = 0.2$ S/m at hydrostatic pressure $P_{gs} = 10$ MPa: 1 – voltage on the discharge gap; 2 – discharge current; 3 – signal of the photodiode sensor recording the luminescence near the anode; $a - U_0 = 17$ kV; $b - U_0 = 18.5$ kV
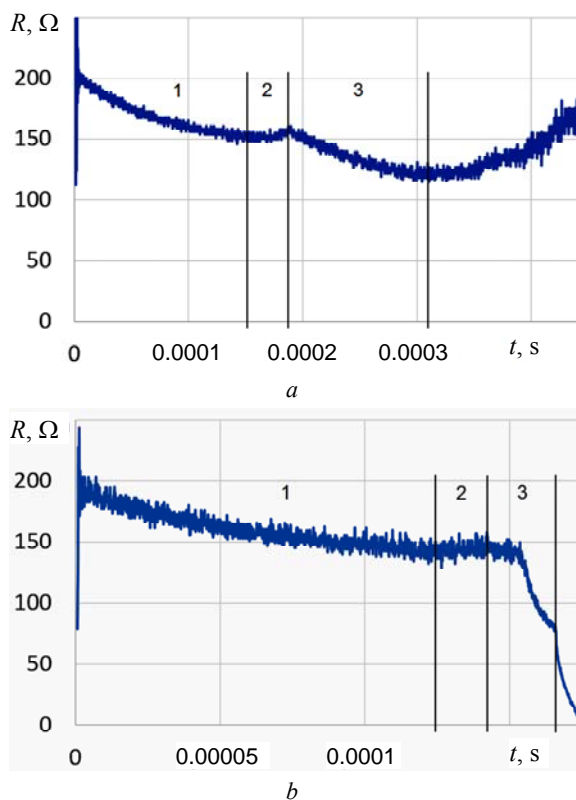
Fig. 4. The change in the resistance of the water gap
calculated from the oscillograms of Fig. 3:
$a - U_0 = 17$ kV; $b - U_0 = 18.5$ kV

When the voltage is applied to the interelectrode gap in the aqueous electrolyte, pre-breakdown currents begin to flow through it. Under their action, Joule heating occurs, which is accompanied by an increase in the temperature of the electrolyte and a decrease in the active resistance of the gap in phase 1.

At the boundary of phases 1 and 2, the resistance stabilizes with its subsequent growth in phase 2. We assume that this change is caused by the onset of the formation of gas bubbles near the electrode-cathode. As a result, the surface area of the cathode contacting the electrolyte decreases, and the current density and temperature of the contact boundary continue to increase.

At the boundary of phases 2 and 3, the resistance again begins to decrease. We believe that at this point in time the size of the gas bubble reaches a critical value at which the residual voltage applied to the electrode system contributes to the breakdown of the bubble to form a streamer. It should be noted that at a relatively small hydrostatic pressure, the liquid is already saturated with gas inclusions, therefore the duration of phases 1 and 2 in this case is much less than at elevated pressure, which has been repeatedly confirmed by experiment. The growth of the streamer (or streamer system) leads to a decrease in resistance due to a reduction in the distance between its head and the cathode, as well as a further increase in the temperature of the electrolyte. The phase of growth of streamers can be terminated by attenuation (Fig. 4,a), followed by the restoration of the gap resistance, or by the cathode achievement by a streamer, by forming a channel of low conductivity with the dissipation of energy remaining in the energy storage

device in the active stage of the discharge and a sharp decrease in resistance (Fig. 4,b).

Conclusions.

1. A review and analysis of modern concepts of pre-breakdown processes in a high-voltage electric discharge in a liquid are carried out, which showed that the «bubble» model of discharge ignition in a liquid is applicable at an electric field strength (36 – 180) kV/cm.

2. Based on the results of experimental studies of the electrical discharge characteristics in the aqueous electrolyte at increased hydrostatic pressure and the minimum voltage providing ignition of the discharge, the bubble model of the stage of its high-voltage breakdown formation was further developed. A qualitative description of the three phases of the stage of formation of a plasma channel in a liquid electrolyte is proposed.

3. Further development of the method for calculating the pre-breakdown characteristics of an electric discharge in a liquid on the basis of a bubble model can determine ways to increase the efficiency of a number of high-voltage electrical discharge devices.

REFERENCES
1. Gulyi G.A. *Osnovy razriadnoimpul'snykh tekhnologii* [Basics of discharge impulse technologies]. Kiev, Naukova Dumka Publ., 1990. 208 p. (Rus).
2. Krivitskii E.V. *Dinamika elektrovzryva v zhidkosti* [Dynamics of electric explosion in a liquid]. Kiev, Naukova Dumka Publ., 1986. 208 p. (Rus).
3. Ushakov V.Ia. Physics of breakdown of liquid dielectrics. *Bulletin of the Tomsk Polytechnic University,* 2004, vol.307, no.2, pp. 80-87. (Rus).
4. Kuzhekin I.P. Investigation of the breakdown of a liquid in an inhomogeneous field with rectangular wave stresses. *Technical Physics,* 1966, vol.36, no.12, pp. 2125-2130. (Rus).
5. Wang Y., Liao D., Zhang W., Sun H. A COMSOL modeling of the pre-breakdown heating phase in the electro-thermal breakdown of conductive water. *3rd International Conference on Materials Engineering, Manufacturing Technology and Control (ICMEMTC 2016)*, 2016, pp. 704-707. **doi: 10.2991/icmemtc-16.2016.141.**
6. Bragg J.K., Sharbouqh A.H., Crowe R.W. Cathode effects in the Dielectric Breakdown of Liquids. *Journal of Applied Physicsys*, 1954, vol.25, no.3, pp. 382-391. **doi: 10.1063/1.1721645.**
7. Seepersad Y., Fridman A., Dobrynin D. Anode Initiated Impulse Breakdown in Water: the Dependence on Pulse Rise Time For Nanosecond and Sub-Nanosecond Pulses and Initiation Mechanism Based on Electrostriction. *Journal of Physics D: Applied Physics*, 2015, vol.48, no.42, p. 424012. **doi: 10.1088/0022-3727/48/42/424012.**
8. Sun A., Zhuang J., Huo C. Formation mechanism of streamer discharges in liquids: a review. *High Voltage*, 2016, vol.1, no.2, pp. 74-80. **doi: 10.1049/hve.2016.0016.**
9. Yan D., Bian D., Zhao J., Niu S. Study of the Electrical Characteristics, Shock-Wave Pressure Characteristics, and Attenuation Law Based on Pulse Discharge in Water. *Shock and Vibration*, 2016, vol.2016, pp. 1-11. **doi: 10.1155/2016/6412309.**
10. Ianshin E.V., Ovchinnikov I.T., Vershinin Iu.N. Mechanism of pulsed electric water breakdown. *Reports of AS of the USSR*, 1974, vol.214, no.6, pp. 1303-1306. (Rus).
11. Ushakov V.Ia., Klimkin V.F., Korobeinikov S.M., Lopatin V.V. *Proboi zhidkostei pri impul'snom napriazhenii* [Breakdown of liquids under impulse voltage]. Tomsk, NTL Publ., 2005. 488 p. (Rus).

12. Clements J.S., Sato M., Davis R.N. Preliminary investigation of prebreakdown phenomena and chemical reaction using a paused high-voltage discharge in water. *IEEE Transactions on Industry Applications*, 1987, vol.IA-23, no.2, pp. 224-235. **doi: 10.1109/TIA.1987.4504897.**

13. Fujita H., Kanazawa S., Ohtani K., Komiya A., Kaneko T., Sato T. Initiation process and propagation mechanism of positive streamer discharge in water. *Journal of Applied Physics*, 2014, vol.116, no.21, p. 213301. **doi: 10.1063/1.4902862.**

14. Kuskova N.I. Spark discharges in condensed media. *Technical Physics,* 2001, vol.46, no.2, pp. 182-185. **doi: 10.1134/1.1349273.**

15. Poklonov S.G. *Vysokovol'tnye elektrorazriadnye pogruzhnye ustanovki so stabilizatsiei elektrogidroimpul'snogo vozdeistviia.* Avtoref. diss. kand. tekhn. nauk [High-voltage electric discharge submersible devices with stabilization of electrohydropulse impact. Abstracts of cand. tech. sci. diss.]. Kiev, 2004. 18 p. (Rus).

16. Zhekul V.G., Rakovskii G.B. To the theory of the formation of an electrical discharge in a conducting liquid. *Technical Physics*, 1983, vol.53, no.1, pp. 8-14. (Rus).

17. Rakovskii G.B., Khainatskii S.A, Zhekul V.G. To calculation of the discharge ignition voltage in conducting liquids. *Technical Physics*, 1984, vol.54, no.2, pp. 368-370. (Rus).

18. Rakovskii G.B. *Peregrevnaia neustoichivost' v nachal'noi stadii elektricheskogo razriada v provodiashchei zhidkosti.* Av-toref. diss. kand. fiz.-mat. nauk [Overheating instability in the initial stage of an electrical discharge in a conducting fluid. Abstracts of cand. phys.-math. sci. diss.]. Leningrad, 1984. 23 p. (Rus).

19. Smirnov A.P., Zhekul V.G., Mel'kher Iu.I., Taftai E.I., Khvoshchan O.V., Shvets I.S. Experimental study of pressure waves generated by an electric explosion in a closed volume of a liquid. *Elektronnaya obrabotka materialov*, vol.53, no.4, pp. 47-52. (Rus). **doi: 10.5281/zenodo.1053757**

V.G. Zhekul[1]*, Candidate of Technical Science, Senior Research Scientist,*
O.V. Khvoshchan[1]*, Candidate of Technical Science, Senior Research Scientist,*
O.P. Smirnov[1]*, Candidate of Technical Science, Senior Research Scientist,*
E.I. Taftaj[1]*, Research Scientist,*
I.S. Shvets[1]*, Candidate of Physics and Mathematics Sciences, Leading Research Scientist,*
[1] Institute of Pulse Processes and Technologies (IPPT) of NAS of Ukraine,
43-A, Bohoyavlensky Ave., Mykolayiv, 54018, Ukraine,
phone +380 512 224113,
e-mail: Smirnovap1978@gmail.com, Khvoshchan@gmail.com

Z. Montazeri, T. Niknam

OPTIMAL UTILIZATION OF ELECTRICAL ENERGY FROM POWER PLANTS BASED ON FINAL ENERGY CONSUMPTION USING GRAVITATIONAL SEARCH ALGORITHM

Purpose. Energy consumption is a standard measure to evaluate the progress and quality of life in a country. When used properly and logically it could be cause of progress in science, technology and welfare of the people in any country and otherwise irreparable economic losses and economic gross recession would happen. And finally, the quantity of energy consumption per GDP will increase day by day. Electrical energy, as the most prominent type of energy, is very important. In this article based on a different approach, according to the final consumption of electric energy, a proper economic planning in order to supply electrical energy is submitted. In this programming, the details of final energy consumption, will replace with the information of power network, by considering the network efficiency and power plants. Operation of power plants is based on the energy optimization entranced to a plant. By using the proposed method and gravitational search algorithm, the total cost of electrical energy can be minimized. The results of simulation and numerical studies show better convergence of gravitational search algorithm in comparison with other existing methods in this area. References 17, tables 2, figures 4.
Key words: **gravitational search algorithm, energy, electrical energy, economic distribution, final energy consumption.**

Цель. Энергопотребление является стандартной мерой для оценки прогресса и качества жизни в стране. Правильное и обоснованное ее использование может привести к прогрессу в науке, технике и благосостоянии людей в любой стране, в противном случае произойдут непоправимые экономические потери и падение валового внутреннего продукта. И, наконец, количество потребленной энергии на единицу ВВП будет возрастать с каждым днем. Электрическая энергия, как основной вид энергии, является весьма важной. В данной статье, основываясь на различных подходах, в соответствии с конечным потреблением электрической энергии, представлено соответствующее экономическое планирование подачи электроэнергии. При этом, подробности конечного потребления энергии заменяются информацией о сети электроснабжения, учитывая эффективность сети и электростанций. Работа электростанций основана на оптимизации энергии, производимой ею. Используя предложенный метод и алгоритм гравитационного поиска, можно минимизировать общую стоимость электрической энергии. Результаты моделирования и численных исследований показывают лучшую сходимость алгоритма гравитационного поиска по сравнению с другими существующими методами в данной области. Библ. 17, табл. 2, рис. 4.
Ключевые слова: **алгоритм гравитационного поиска, энергия, электрическая энергия, экономическое распределение, конечное потребление энергии.**

Introduction. The energy consumption trend in recent years has been very rapid and worrying. This process in developing countries, especially Iran has been much higher than the global average. The continuation of energy supply and ensuring long-term access to resources, needs a comprehensive energy plan, and therefore the energy planning is the undeniable necessities of economic, national and strategic in a country. One of the key topics that is discussed in the context of energy planning, is the economic distribution of electrical energy.

Economic dispatch problem using Tucker-Cohen is performing well and appropriate economic status is determined. When these conditions are met, all the plants that are in circuit, with the exception of plants that can effectively inject their maximum power into the network, due to their amount of fuel are loaded [1]. Economic dispatch methods can be placed in two groups of analytical methods and intelligent systems. One of the most famous and oldest analytical methods, is Lagrange method [2]. Including the intelligent systems, can note the optimization of the application of innovative methods in economic dispatch and entrance of plant into the circuit [3].

Despite the research conducted on the economic dispatch and as a result, the problem of entrancing the plant into the circuit, most of these studies has been appropriated by electric power consumer's expectations. In this paper a different approach with regard to the undeniable importance of energy, is presented in the field of economic distribution with needs of consumers. In describing this new and different expression, according to the final consumption of electric energy, economic distribution of this energy consumption will be established by power plants. And then based on different power plants efficiency, input energy requirements of power plants, is planned and optimized.

In this paper, first in the second part, definition and discussion of how to formulate economic distribution of energy is expressed. Then, in the third part gravitational search algorithm is presented. The fourth part of the article is devoted to the application of gravitational search algorithm in the context of economic distribution. In the fifth part the simulation results are given and finally in the sixth part of the article summary is expressed.

Problem statement and formulation. The cost of electrical power distribution for the whole system is equal to the sum of Costs of different units [4]. The basic operation of the system is that the total output powers must be equal to the total load [5]. In this case the economic dispatch is expressed by relations:

$$F_T = \sum_{i=1}^{N} F_i(P_i); \qquad (1)$$

$$\varnothing = 0 = P_R - \sum_{i=1}^{N} P_i, \qquad (2)$$

where F_T is the total cost of the operation from the system, N is the number of power plants, P_i is the share of i-th power plant from the total demand, and $F_i(P_i)$, is the cost of power plants, in order to generating power P. Ø indicating the fundamental issue P_R, is the total demand.

It should be noted that each plant is able to operate in the range of its unique ability to inject power. This range of capability is expressed as:

$$P_{i.\min} \le P_i \le P_{i.\max} , \qquad (3)$$

where $P_{i.\min}$ and $P_{i.\max}$ respectively, are the minimum and maximum power injection at the i-th power plant.

Expressions (1) and (2) show the overview of the economic distribution of electric power, we intend to extend this relation into the energy definition domain. So, in the new expression, E_R replacing with P_R and we define total electric energy demand based on final consumption of electrical energy. Therefore, this new attitude we try to provide electrical energy demand in a way to reduce the rate of its costs. The subject that expressed in fact is an optimization problem with a constraint which can be solved with optimization existing methods. However analytical methods such as Lagrange method solve this issue, but in the complex systems and real great, especially when considering the losses and efficiency of the network and in fact nonlinear problem, becomes more with computational complexity. In these situations, evolutionary optimization algorithms, represent their ability to well solve such issues. Various evolutionary optimization algorithms have been proposed and introduced by various authors [6-10].

Gravitational search algorithm. Considering the extent and complexity of the issues and the importance of speed to get answers, other classical optimization methods, do not have ability to solve many issues, and instead of searching of comprehensive space, random search algorithms are used to define the problem. This has led to the use of heuristic search algorithm (intuitive or initiatives) which have grown substantially in recent years [6-10]. Heuristic algorithms have demonstrated their high ability in many fields of science such as transport [11], bioinformatics [12], data mining [13], physical chemistry [14], electronics [15] and other related fields. The achievement of an appropriate mathematical model to the process of searching for innovative methods, is very hard and even impossible [13]. Therefore, this type of algorithms, can be named as «black boxes» optimization algorithms [16].

According to the gravity law each mass perceived location and status of other masses through the law of gravitational attraction. Therefore, this force can be used as a tool for information exchange. The optimum detector designed to solve the optimization problem can be used, which each answer can be defined as a position in space and its similarity to the other solutions can be expressed as a distance. The rate of masses is determined according to the objective function [17].

However, imagine the system as a set of m object. The position of each object is a point in space which is an answer of the problem. In (4), the position of dimension d of the object i is shown with x_i^d

$$X_i\left(x_i^1, ..., x_i^d, ..., x_i^n\right). \qquad (4)$$

At first, randomly the initial position of the objects, is define in the space of problem definition, these objects due to the forces which exert to each other proceed towards the answer of the problem.

In this system at time t to mass i from mass j in the direction of dimension d force equal to $F_{ij}^d(t)$ is imported. M_{gj} is gravitational mass of mass j, $G(t)$ is the gravitational constant in time t and R_{ij} is the distance between the two objects j and i. Euclidean distance is used to determine the distance between the objects. ε is a very small number

$$F_{ij}^d(t) = \frac{G(t)M_{gj}(t)}{R_{ij}(t) + \varepsilon}\left(x_j^d(t) - x_i^d(t)\right), \qquad (5)$$

$$R_{ij}(t) = \left\| X_i(t) \cdot X_j(t) \right\|_2 . \qquad (6)$$

Force on object j in the direction of dimension d at the time t, $F_i^d(t)$, is calculated according to (7). In this equation, r_1 is a random number with uniform distribution in [0-1]

$$F_i^d(t) = \sum_{j=1, j \ne i}^m r_1 F_{ij}^d(t). \qquad (7)$$

Acceleration of object i in the direction of dimension d at time t is shown with $a_i^d(t)$ and inertial mass of object i is shown with $Mi_1(t)$

$$a_i^d(t) = \frac{F_i^d(t)}{Mi_1(t)}. \qquad (8)$$

In this case we have:

$$V_i^d(t+1) = r_2 V_i^d(t) + a_i^d(t), \qquad (9)$$

$$x_i^d(t+1) = x_i^d(t) + V_i^d(t+1), \qquad (10)$$

where r_1 and r_2 are uniformly-distributed random numbers in [0-1] which have been used to maintain the random search. V_i^d is speed of dimension d from object i.

Relationship (5) to (10), will repeat until the convergence condition is established.

Problem solving of economic distribution using gravitational search algorithm. Distribution of electrical energy, is a non-linear problem and due to high provisions has a very high complexity. For this reason, the usual methods for solving this problem are faced with many problems, and either are not able to solve this problem or solve the problem with many hardships. For these reasons described in this article gravitational search algorithm is used to solve nonlinear problems which is very efficient.

Electric energy demand is equal to E_R. In the period studied, power plants which are available assumed to be constant, so each of these power plants, are at their least production. Different power plants according to the structure have different efficiencies. When the economic distribution of electrical energy is concerned, this fully shows. Thus, only the desired power generation is not considered, but the total final consumption of energy that needed to provide electric energy is optimized. In other words, for effective optimization is done.

We introduce the network efficiency with η and efficiency of different power plants with η_i for $n, i = 1, 2,\ldots$

$$E_{RL} = \eta E_R; \tag{11}$$

$$E_{RL} = \sum_{i=1}^{n} \eta_i E_i, \tag{12}$$

where E_{RL} is the energy demand of the power plant due to final energy consumption and efficiency of the network and E_i is the input energy required to i-th power plant.

The simulation is done in time domain, so, the mean power and electric power, are the same.

Simulations and results. The simulation is performed based on a specific system in accordance with Table 1. Values of a, b and c related to the input data of costs of power plant operation that is used to calculate the relation

$$F_i(P_i) = aP_i^2 + bP_i + c, \tag{13}$$

where F_i is the operating costs, and P_i is the amount of i-th power plant output power.

Table 1

Information about power system plants

unit	P_{min}(MW)	P_{max}(MW)	a	b	c	η
1	150	455	0.00048	19.16	1000	30
2	150	455	0.00031	26.17	970	45
3	20	130	0.002	16.6	700	32
4	20	130	0.00211	16.5	680	35
5	25	162	0.00398	19.7	450	28
6	20	80	0.007	22.26	370	27
7	25	85	0.00079	27.74	480	30
8	10	55	0.004	25.92	660	35
9	10	55	0.00222	27.27	665	33
10	10	55	0.002	27.79	670	33

It assumed that E_R is equal to 1500 kWh, if the efficiency of the network is equal to 75 %, so the demand from the power plant E_{RL} will be 2000 kWh. Performance of the gravity algorithm, was compared with genetic algorithm and particle population algorithm, the results of the implementation of the three algorithms are shown in Table 2.

Table 2

The simulation results of the studied power system

	GA	PSO	GSA
The best answer	70492.205	70526.659	70785.216
Average of answers	70546.156	70574.379	70837.164
The worst answer	70913.142	71052.215	71356.184

To evaluate the proposed method, gravitational algorithm, genetic algorithm and particle swarm algorithm in solving the problem of finding the minimum of economic distribution problem, have been implemented under the same conditions. For $n = 30$, and population size equal to 50, the results for 1500 times iteration is given in Table 2. And for comparison, the fitness average and the best answer which so far has been observed are calculated. These parameters were calculated for 20 times for the implementation of the stand-alone application and middle of the results is obtained. The results of gravitational algorithm show better performance. In the PSO simulation, relation (14) is used for updating the particles velocity in this relation, $c_1 = c_2 = 2$, and w decreases linearly from 0.9 to 0.2. In this relation $V_i^d(t)$, is velocity of particle i in d dimension

in time t, and r_1 and r_2 are random numbers uniformly distributed between zero and one. Also g_{best} is the best position that has been found by the community, $p_{best i}$ is the best position that particle i so far has been accessed

$$V_i^d(t+1) = w(t)V_i^d(t) + c_1 r_{1i}(t)\left[p_{best_i}^d(t) - V_i^d(t)\right] + c_2 r_{2i}(t)\left[g_{best}^d(t) - X_i^d(t)\right]. \tag{14}$$

In order to evaluate the results of the presented objective function optimization, this case is shown in the Table 2. As seen in Table 2, gravitational search algorithm has more acceptable performance and results than GA and PSO algorithms. The results demonstrate the convergence of the GSA algorithm compared to RGA and PSO algorithms.

In order to evaluate the progress of the optimization process, in Fig. 1 to Fig.3 the accomplishing pattern of the optimal solution for gravitational, particle population and genetics algorithms is drawn. Also, in order to have a proper comparison of the performance for these algorithms, the achieving pattern of these algorithms for optimal solution are shown in Fig. 4, simultaneously.
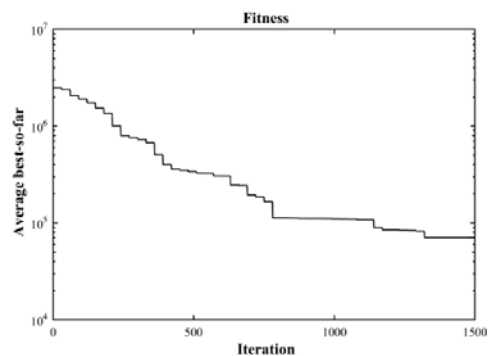

Fig. 1. Accomplishing pattern of the optimal solution by GSA algorithm
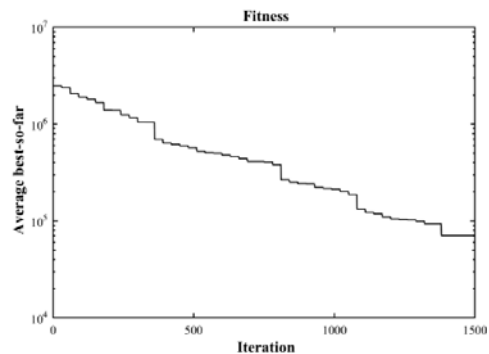

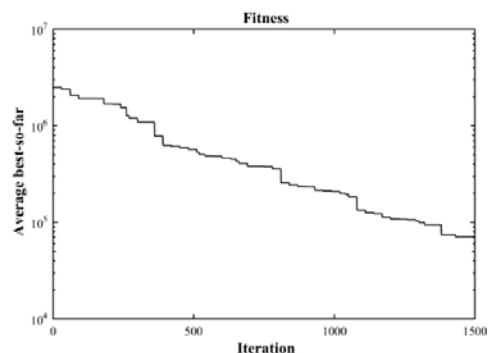Fig. 2. Accomplishing pattern of the optimal solution by PSO algorithm

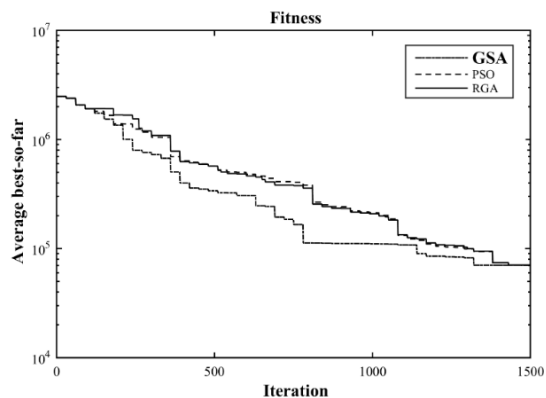Fig. 3. Accomplishing pattern of the optimal solution by GA algorithm

Fig. 4. The comparison of the evolutionary algorithms GSA, PSO and GA to achieve the optimal solution

Conclusion. Electrical energy is very important, and therefore it is important to minimize the energy costs. In a new approach in this paper, according to the final consumption of electric energy and efficiency of power system planets and network, the economic distribution of electrical energy is created. In this regard, according to the non-linear nature of the problem, evolutionary algorithms have been used. The results of the simulation show the well performance of gravity algorithm in compare to other algorithms.

REFERENCES
1. Kuhn H.W., Tucker A.W. Nonlinear Programming. Proceedings of the Second Berkeley Symposium on Mathematical Statistics and Probability, University of California, 1951, pp. 481-492.
2. Yamin H.Y. Review on methods of generation scheduling in electric power systems. *Electric Power Systems Research*, 2004, vol.69, no.2-3, pp. 227-248. **doi: 10.1016/j.epsr.2003.10.002**.
3. Yuan X., Su A., Nie H., Yuan Y., Wang L. Application of enhanced discrete differential evolution approach to unit commitment problem. *Energy Conversion and Management*, 2009, vol.50, no.9, pp. 2449-2456. **doi: 10.1016/j.enconman.2009.05.033**.
4. Zaman M.F., Elsayed S.M., Ray T., Sarker R.A. Evolutionary Algorithms for Dynamic Economic Dispatch Problems. *IEEE Transactions on Power Systems*, 2016, vol.31, no.2, pp. 1486-1495. **doi: 10.1109/TPWRS.2015.2428714**.
5. Surender Reddy S., Bijwe P.R., Abhyankar A.R. Real-Time Economic Dispatch Considering Renewable Power Generation Variability and Uncertainty Over Scheduling Period. *IEEE Systems Journal*, 2015, vol.9, no.4, pp. 1440-1451. **doi: 10.1109/JSYST.2014.2325967**.
6. Tang K.S., Man K.F., Kwong S., He Q. Genetic algorithms and their applications. *IEEE Signal Processing Magazine*, 1996, vol.13, no.6, pp. 22-37. **doi: 10.1109/79.543973**.
7. Kirkpatrick S., Gelatt C.D., Vecchi M.P. Optimization by Simulated Annealing. *Science*, 1983, vol.220, no.4598, pp. 671-680. **doi: 10.1126/science.220.4598.671**.
8. Farmer J.D., Packard N.H., Perelson A.S. The immune system, adaptation, and machine learning. *Physica D: Nonlinear Phenomena*, 1986, vol.22, no. 1-3, pp. 187-204. **doi: 10.1016/0167-2789(86)90240-x.**
9. Dorigo M., Maniezzo V., Colorni A. Ant system: optimization by a colony of cooperating agents. *IEEE Transactions on Systems, Man and Cybernetics, Part B (Cybernetics)*, 1996, vol.26, no.1, pp. 29-41. **doi: 10.1109/3477.484436.**
10. Kennedy J., Eberhart R. Particle swarm optimization. *Proceedings of ICNN'95 – International Conference on Neural Networks*. **doi: 10.1109/icnn.1995.488968**.
11. Zarandi M.H.F., Hemmati A., Davari S. The multi-depot capacitated location-routing problem with fuzzy travel times. *Expert Systems with Applications*, 2011, vol.38, no.8, pp. 10075-10084. **doi: 10.1016/j.eswa.2011.02.006**.
12. Mitra S., Banka H. Multi-objective evolutionary biclustering of gene expression data. *Pattern Recognition*, 2006, vol.39, no.12, pp. 2464-2477. **doi: 10.1016/j.patcog.2006.03.003**.
13. Zahiri S.H. *Swarm Intelligence and Fuzzy Systems*. Nova Science Publ., USA, 2010.
14. Darby S., Mortimer-Jones T.V., Johnston R.L., Roberts C. Theoretical study of Cu–Au nanoalloy clusters using a genetic algorithm. *The Journal of Chemical Physics*, 2002, vol.116, no.4, pp. 1536-1550. **doi: 10.1063/1.1429658**.
15. Coello Coello C.A., Luna E.H., Aguirre A.H. Use of Particle Swarm Optimization to Design Combinational Logic Circuits. *Lecture Notes in Computer Science*, 2003, pp. 398-409. **doi: 10.1007/3-540-36553-2_36**.
16. Wolpert D.H., Macready W.G. No free lunch theorems for optimization. *IEEE Transactions on Evolutionary Computation*, 1997, vol.1, no.1, pp. 67-82. **doi: 10.1109/4235.585893**.
17. Rashedi E., Nezamabadi-pour H., Saryazdi S. GSA: A Gravitational Search Algorithm. *Information Sciences*, 2009, vol.179, no.13, pp. 2232-2248. **doi: 10.1016/j.ins.2009.03.004**.

Zeinab Montazeri[1]*, Candidate of Power Engineering, M.Sc. Student,*
Taher Niknam[1]*, Doctor of Power Engineering, Professor,*
[1] Department of Electrical Engineering,
Islamic Azad University of Marvdasht,
Marvdasht, I.R. Iran.
phones +989171128689, +989171876173
e-mail: Z.montazeri2002@gmail.com, niknam@sutech.ac.ir